Active Flow Control for Aerodynamic Efficiency Enhancement in Transonic Flow

Zur Erlangung des akademischen Grades einer
Doktorin der Ingenieurwissenschaften (Dr.-Ing.)
von der KIT-Fakultät für Maschinenbau des
Karlsruher Instituts für Technologie (KIT)

genehmigte

Dissertation

von

M.Sc. Annika Frede

Tag der mündlichen Prüfung:	23.10.2026
Hauptreferentin:	Prof. Dr.-Ing. Bettina Frohnapfel
Korreferentin:	Prof. Dr.-Ing. Andrea Beck



This document is licensed under a Creative Commons Attribution 4.0 International License (CC BY 4.0): https://creativecommons.org/licenses/by/4.0/deed.en

Abstract

The present work investigates active flow control methods for improving the aerodynamic efficiency in compressible and transonic flows. The two flow control techniques of wall-normal homogeneous blowing and suction and streamwise travelling waves of spanwise velocity are investigated. Both methods show a reduction in drag in canonical flows, but their effectiveness and underlying mechanisms in the transonic regime remain poorly understood.

The first part of the thesis presents a comprehensive numerical investigation of wall-normal blowing and suction applied to an airfoil in the subsonic and transonic flow regime. A parametric study is conducted over a wide range of variables and control parameters, including Mach number, angle of attack, control position, and control magnitude. In the analysis, the energetic costs for the actuation are included. The results show that shock boundary-layer interaction fundamentally alters the flow-control response. In contrast to observations of the control in subsonic flow regimes, the results show that suction applied on the suction side of a transonic airfoil can significantly improve aerodynamic efficiency. The increase in efficiency is achieved by a reduction in total drag through a downstream displacement of the shock.

In the second part of the work, the question of why different active flow control methods can produce similar improvements in aerodynamic efficiency despite inducing opposite effects on local skin friction is addressed. Direct numerical simulations are performed to compare the active control of wall-normal suction with streamwise travelling waves under identical transonic flow conditions. While both methods lead to a gain in aerodynamic efficiency, travelling waves reduce the skin friction drag locally, while suction increases it. A detailed analysis of the flow showed that the dominant mechanism leading to the efficiency increase is not the local modification of the wall shear stress, but a reduction of the momentum thickness upstream of the shock accompanied by a downstream shift of the shock and an increase in lift.

The results of the present work present new insights into the mechanisms responsible for the efficiency increase for active flow control in transonic flows. The results show that local friction drag reduction alone is not a sufficient indicator of an improvement in aerodynamic efficiency, and the shock boundary layer interaction plays a significant role.

Kurzfassung

Die vorliegende Arbeit befasst sich mit der aktiven Strömungskontrolle zur Verbesserung der aerodynamischen Effizienz in kompressiblen und transonischen Strömungen. Untersucht werden die beiden Kontrollmethoden des wand-normalen homogenen Ausblasens und Absaugens sowie die in Strömungsrichtung wandernden Wellen von spannweitiger Geschwindigkeit (streamwise travelling waves of spanwise velocity). Beide Methoden zeigen in kanonischen Strömungen eine Verringerung des Widerstands, wobei die zugrundeliegenden Mechanismen im transonischen Bereich noch nicht vollständig verstanden sind.

Der erste Teil der Arbeit präsentiert eine umfassenden numerische Untersuchung des wand-normalen Ausblasens und Absaugens, die auf einem Tragflügel im subsonischen und transonischen Strömungsbereich angewendet wird. Es wird eine Parameterstudie über einen großen Bereich an Variablen, wie der Machzahl, Anstellwinkel, Kontrollposition und Kontrollgröße durchgeführt. Die Analyse berücksichtigt die energetischen Kosten der Kontrolle. Die Ergebnisse zeigen, dass die Wechselwirkung zwischen Stoß und Grenzschicht das Verhalten der Kontrolle grundlegend ändert. In Gegensatz zu Beobachtungen der Kontrolle im subsonischen Strömungsbereich zeigen die Ergebnisse, dass ein Absaugen auf der Oberseite des Tragflügels die aerodynamische Effizienz deutlich verbessern kann. Die Erhöhung der Effizienz kann durch eine Verringerung des Gesamtwiderstands aufgrund einer stromabwärts Verschiebung des Stoßes erreicht werden.

Im zweiten Teil der Arbeit wird die Frage beantwortet, warum unterschiedliche Methoden der aktiven Strömungskontrolle trotz verschiedener Effekten auf den lokalen Reibungswiderstand zu vergleichbaren Verbesserungen der aerodynamischen Effizienz führen. Es werden direkte numerische Simulationen durchgeführt, um wand-normales Absaugen mit StTW unter identischen transsonischen Strömungsbedingungen zu vergleichen. Während beide Methoden zu einer Verbesserung der Effizienz führen, reduzieren StTW den lokalen Reibungswiderstand, während Absaugen ihn erhöht. Eine detaillierte Analyse der Strömungen zeigt, dass der dominierende Mechanismus, der zur Effizienzsteigerung führt, nicht die lokale Veränderung der Wandschubspannung ist, sondern eine Verringerung der Impulsdicke stromaufwärts des Stoßes zusammen mit einer Verschiebung des Stoßes in Richtung der Hinterkante sowie einer Zunahme des Auftriebs.

Die Ergebnisse der vorliegenden Arbeit liefern neue Erkenntnisse über die Mechanismen, die für die Verbesserung der Effizienz mit aktiver Strömungskontrolle in transonischen Strömungen verantwortlich sind. Die Ergebnisse zeigen, dass eine lokale Verringerung der Wandschubspannung kein ausreichendes Kriterium für eine Verbesserung der Effizienz ist und dass eine Wechselwirkung zwischen Stoß und Grenzschicht eine bedeutende Rolle spielt.

Acknowledgements

First and foremost, I would like to express my sincere gratitude to Bettina Frohnapfel for allowing me to work on this exciting research topic. I am deeply grateful for her continuous support and guidance throughout this project.

I am also very grateful to Davide Gatti for supervising me during my time at ISTM. I greatly appreciated his feedback and the insightful scientific discussions. His support and encouragement have contributed substantially to my scientific development and this thesis.

I would like to thank Andrea Beck for agreeing to evaluate this dissertation and for taking the role of second examiner. I sincerely appreciate the time and effort invested in reviewing my work.

I would also like to gratefully acknowledge the generous financial support provided by the Friedrich and Elisabeth Boysen-Stiftung (Grant No. BOY-164). Without this support, the completion of this research would not have been possible.

My sincere thanks also go to all my colleagues at ISTM for creating such a supportive and inspiring working environment. I am grateful for the scientific discussions and the conversations that made my time at ISTM so memorable.

Finally, I would like to express my deepest gratitude to my family and friends. Above all, I thank my parents, whose unconditional love and unwavering belief in me have supported me throughout every stage of my education and have made this achievement possible. Further, I am deeply grateful to Jonas for his endless patience and constant support throughout this journey.

Contents

Abstract i

Kurzfassung iii

Acknowledgements v

1 Introduction 1
1.1 Motivation 1
1.2 Research Objectives and Outline 2

2 Literature Review 5
2.1 Passive and Active Flow Control 5
2.2 Wall-normal homogeneous Blowing and Suction 5
2.3 Streamwise Travelling Waves 8

3 Governing Equations and Flow Physics 11
3.1 Conservation Equations 11
3.1.1 Reynolds Transport Theorem 11
3.1.2 Conservation of Mass 12
3.1.3 Conservation of Momentum 12
3.1.4 Conservation of Energy 14
3.2 Aerodynamic equations 15
3.2.1 Lift and Drag coefficients 15
3.2.2 Mach and Reynolds number 16
3.3 Turbulent Boundary Layers in Compressible Flows 16
3.3.1 General Introduction to Turbulence 16
3.3.2 Boundary Layer in Compressible Flow 17
3.3.3 Boundary Layer Thickness Definitions 17
3.3.4 Viscous Scaling 19
3.3.5 Laminar-Turbulent Transition 19
3.3.6 Flow Separation 20
3.3.7 Shock-Boundary Layer Interaction 21
3.4 Turbulence Modeling 22
3.4.1 Turbulence Modeling Approaches 22
3.4.2 Direct Numerical Simulations 22
3.4.3 Large Eddy Simulations 23
3.4.4 Reynolds-Averaged Navier-Stokes Simulations 23
3.4.5 Turbulence model 24
3.4.6 Comparison of Turbulence Modeling Approaches 24

4 Numerical methods 27
4.1 Momentum Budget Airfoil 27
4.1.1 Body Drag 28
4.1.2 Wake Drag 28
4.1.3 Momentum balance with micro blowing 29

4.1.4 Consideration of mass source . . . 29
4.2 Implementation of General Boundary Layer Conditions . . . 30
4.2.1 No-Slip adiabatic wall . . . 30
4.2.2 Far Field Boundary Condition . . . 30

5 Parametric study of blowing and suction for turbulent flow control on a transonic airfoil . . . 33
5.1 Methodology . . . 33
5.1.1 Numerical methods . . . 33
5.1.2 Boundary Conditions . . . 34
5.1.3 Net drag . . . 35
5.1.4 Power Budget . . . 36
5.1.5 Parametric Study . . . 38
5.2 Validation of RANS code . . . 39
5.3 Effects of Parameter Variations . . . 41
5.3.1 Effect of Control Configuration . . . 41
5.3.2 Effect of Control Magnitude . . . 43
5.3.3 Effect of Mach number . . . 47
5.3.4 Effect of Control Position . . . 49
5.3.5 Effect of Reynolds number . . . 49
5.4 Efficiency Increasing Configurations . . . 51
5.5 Discussions of the Parametric Study . . . 54
5.6 Bayesian Optimization . . . 55
5.7 Methodology . . . 55
5.8 Results . . . 57

6 Comparison of Streamwise Travelling Waves and Uniform Suction on a Supercritical Airfoil . . . 61
6.1 Methodology . . . 61
6.1.1 Numerical methods . . . 61
6.1.2 Computational Setup . . . 62
6.1.3 RANS Analysis of the V2C airfoil . . . 64
6.1.4 Numerical Database . . . 65
6.2 Results . . . 66
6.2.1 Aerodynamic coefficients . . . 66
6.2.2 Pressure and friction coefficient distribution . . . 68
6.2.3 Pressure and friction drag . . . 71
6.2.4 Instantaneous Velocity Field . . . 72
6.2.5 Boundary Layer Properties . . . 74
6.2.6 Reynolds stresses . . . 79
6.3 Power Consumption . . . 79
6.3.1 Power estimation for StTW . . . 80
6.3.2 Power estimation for US . . . 80
6.3.3 Net Power Consumption . . . 81
6.4 Concluding Discussions . . . 82

7 Final Concluding Discussion . . . 85

8 References . . . 91
Bibliography . . . 91
List of Conference Contributions . . . 97
List of Journal Publications . . . 97

Acronyms and symbols . . . 99

List of Figures **107**

List of Tables **109**

1 Introduction

The reduction of greenhouse gas emissions represents one of the main technological challenges of the present century. The use of fossil energy sources has intensified environmental impacts, leading to growing international efforts to limit carbon dioxide emissions across all sectors. In this context, the European Union has set the goal of reaching a reduction of greenhouse gas emissions of at least 50% by 2030 [2], and net-zero greenhouse gas emissions by 2050 [1], highlighting the importance of ongoing technological development and strategic planning.

The transportation sector plays a central role in this transition. One part is global air traffic, which is expected to grow over the next few years, thus, sustained research efforts aimed at improving the efficiency of aircraft and reducing fuel consumption are essential.

Before the COVID-19 pandemic, aviation was responsible for approximately 2.4% of the global annual carbon dioxide emissions and contributed about 4% to the human-induced global warming [28, 37]. Predictions indicate that the share of aviation-related emissions could increase significantly in the coming decades [28]. Consequently, reducing fuel consumption and associated emissions in aviation remains a critical research priority.

For transport aircraft operating at cruise conditions, fuel consumption is closely linked to aerodynamic drag. Even modest improvements in aerodynamic efficiency can translate into considerable reductions in fuel burn and emissions when accumulated over the operational lifetime of an aircraft [63]. This sensitivity motivates continued research into drag reduction strategies.

1.1 Motivation

At typical cruise conditions, viscous drag contributes a significant portion of approximately 50% to the total aerodynamic drag of transport aircraft. This drag component is governed by the turbulent boundary layer developing over the aircraft's surface [3]. Thus, boundary layer manipulation techniques aimed at reducing viscous drag have long been recognized as a promising pathway for improving aerodynamic efficiency [63].

A broad range of flow control strategies has been proposed and investigated to modify boundary layer dynamics. These approaches are commonly classified into passive and active techniques. Passive flow control methods, such as surface shaping or the application of riblets, do not require an external energy input and are therefore attractive because of their simplicity and robustness [78]. However, the achievable performance improvements are generally modest and are often limited to a narrow range of operating conditions.

Active flow control, by contrast, relies on external actuation to directly influence the flow. Although they introduce additional energetic costs, they offer greater flexibility to cover a broad range of flight conditions and the potential for larger gains in efficiency. In particular, active techniques that target the near-wall region of turbulent boundary layers are of interest, as this region dominates viscous drag production.

Among the various active flow control techniques, wall normal blowing and suction [5, 18, 35, 73] and spanwise travelling waves [10, 22, 59] have received particular attention in recent years, as both target the reduction of the local wall shear stress in the turbulent boundary layer, but achieve this through fundamentally different physical mechanisms.

Among the earliest active approaches is wall-normal blowing and suction, where a small amount of mass is injected into or removed from the boundary layer through a porous surface. Early experimental and numerical studies established the fundamental effects of this method on the boundary layer development, skin-friction drag, and transition behavior over flat plates and in channel flows [13, 29, 45, 55]. Subsequent investigations demonstrated that, under certain conditions, wall-normal blowing can locally reduce skin friction and that these effects may persist downstream of the control region [5, 32, 35, 73].

In contrast to wall-normal blowing and suction, which modify the boundary layer through mass transfer across the wall, another class of active flow control techniques directly targets the near-wall turbulence dynamics to reduce drag.

Comparing these approaches is particularly interesting because both methods target a reduction in total drag, while the fundamental mechanisms are different. Their effects on turbulent boundary layers may therefore help to identify the flow phenomena most relevant to aerodynamic drag reduction.

A second class of active flow control strategies aiming for a reduction of skin friction introduces a spanwise velocity component at the wall. This method aims to modify near-wall turbulence by altering the transport of streamwise momentum and suppressing turbulent structures responsible for high shear stresses [34]. Techniques such as oscillating walls and, more recently, streamwise travelling waves of spanwise velocity have demonstrated substantial friction drag reduction potential in canonical turbulent flows [57, 58]. Their effectiveness has been confirmed across a range of configurations, in experiments and flow regimes, including compressible conditions [6, 22].

1.2 Research Objectives and Outline

Despite the encouraging results reported in the literature, several limitations remain. The majority of the investigations on wall-normal blowing and suction have been conducted on simplified configurations, such as flat plates or channel flows, and have focused primarily on incompressible or low-speed conditions [32, 35, 36, 45, 74]. The application of these methods to airfoil flows introduces additional complexities associated with surface curvature, pressure gradients, and pressure drag, thereby complicating the evaluation of their overall effectiveness.

Recent numerical studies have highlighted that local reductions in skin friction do not necessarily translate into reductions in total drag [5, 18]. In some configurations that investigate the flow around an airfoil, improvements in friction drag are offset by unfavorable changes in pressure drag, leading to a net increase in total drag, especially when taking into account the energetic costs for the actuation control [5, 17, 18]. These findings emphasize the importance of considering the complete aerodynamic force balance and energetic efficiency, rather than focusing exclusively on local friction effects.

The challenge becomes even more pronounced in the transonic regime, which is of primary relevance for modern transport aircraft. Under these conditions, compressibility effects lead to the formation of shock waves that interact with turbulent boundary layers, resulting in complex flow phenomena.

Despite their practical importance, transonic flows remain comparatively underexplored in the context of active flow control, particularly for wall-normal blowing and suction.

The overall objective of this thesis is to investigate and clarify the physical mechanism through which active flow control can improve aerodynamic efficiency in compressible and transonic flows relevant for transport aircraft. Special emphasis is placed on understanding the interplay between boundary layer manipulation, shock behavior, and the resulting balance of friction and pressure drag.

The first objective is to assess the performance of wall-normal homogeneous blowing and suction under compressible and transonic conditions. Previous studies by Fahland et al. [18] and Atzori et al. [5] have already investigated the application of the control technique to airfoil geometries in the subsonic regime, providing valuable insights into its aerodynamic effects, leading to the first research question:

How does the active flow control method of wall-normal blowing and suction perform under compressible and transonic flow conditions, and how do shock boundary layer interactions influence its effectiveness in improving aerodynamic efficiency?

Building on the foundation of previous studies, the present work extends the analysis to the compressible and transonic regime, examining how wall-normal blowing and suction influence the boundary-layer development, shock position and strength, and overall aerodynamic efficiency, while accounting for the energetic costs associated with actuation. Therefore, a detailed numerical parametric study is conducted focusing on the effects of Mach and Reynolds number as well as control-specific parameters, such as configuration, magnitude, and position. The results of this investigation are presented in Chapter 5.

A second active flow control aiming for a reduction in friction drag is travelling waves. The application of streamwise travelling waves of spanwise velocities has been extended in recent numerical studies from canonical configurations to airfoil flows [10, 59]. These studies reported a downstream displacement of the shock wave on the upper side of the airfoil, accompanied by an increase in lift and an overall improvement in aerodynamic efficiency under transonic conditions. Similar effects can be seen in the results of the first study conducted in this thesis (see Chapter 5): suction on the upper side leads to a shift of the shock position toward the trailing edge, accompanied by an intensification. Overall, an increase in the aerodynamic efficiency is present, even when taking into account the energetic costs. The effect of the control methods on the local friction drag is fundamentally different, while a reduction of skin friction is reached for the control via travelling waves, an increase is observed for suction.

Although the active control methods of wall-normal homogeneous suction and streamwise travelling waves of spanwise velocity operate through fundamentally different mechanisms and exhibit distinct local effects, both have been shown to produce similar global aerodynamic benefits, raising the fundamental question about the dominant physical mechanisms. In particular, it suggests that factors beyond local skin friction reduction, such as shock displacement and changes in boundary layer thickness, may govern aerodynamic efficiency in compressible and transonic flows. The goal of this thesis is to identify the dominant physical processes responsible for these improvements and evaluate how different control strategies can lead to comparable outcomes in transonic flows.

Ultimately, answering this question will improve the understanding of the physical mechanisms governing drag reduction and aerodynamic efficiency, thereby providing a basis for the systematic development of future flow control strategies.

This leads to the second research question of the thesis:

What are the dominant physical mechanisms responsible for the increase in aerodynamic efficiency in compressible and transonic flows when applying wall-normal suction and streamwise travelling waves, and to what extent do these mechanisms differ between the two approaches?

The second research question is addressed through a detailed comparative analysis of wall-normal suction and streamwise travelling waves of spanwise velocity. Both control methods are investigated under identical flow conditions to ensure a consistent basis for comparison. The two control techniques are performed at the same lift coefficient to directly see the effect of the applied control on the global aerodynamic quantities, such as drag and efficiency, as well as local flow characteristics, including boundary layer properties and shock wave behavior. By examining similarities and differences in the flow response induced by the two control strategies, the study aims to identify the underlying physical mechanism responsible for the observed improvements in aerodynamic efficiency. The results of the comparison are shown in Chapter 6.

A detailed review of the literature on drag reduction with a focus on the active control methods of wall-normal homogeneous blowing and suction and travelling waves is presented in Chapter 2. The fundamental equations and flow physics are described in Chapter 3 and 4. Chapters 4, 5 and 6 contain direct quotations from journal articles by Fahland et al. [FAF$^+$23], Frede and Gatti [FG25] and Frede et al. [FSP$^+$26]. These articles are published by the author of this thesis. While the quotations are highlighted and major changes to the original draft are marked, the nomenclature is adjusted without further comment to be consistent within the present dissertation.

2 Literature Review

2.1 Passive and Active Flow Control

Numerous drag reduction techniques have been proposed and systematically investigated in recent decades [21, 71], with many of them specifically aimed at reducing turbulent skin-friction drag. Since viscous drag represents one of the major contributors to the total drag of transport aircraft [3], significant research has focused on strategies to manipulate the turbulent boundary layer for drag reduction.

The investigated methods can be classified into two categories, passive and active flow control. Passive flow control techniques aim to modify the near-wall flow without requiring external energy input. Typical approaches include modifications of the geometry, such as riblets or tailored surface shaping. These modifications can delay the transition toward the trailing edge and/or reduce the risk of flow separation, which both lead to a reduction in skin friction drag. Riblets are among the most successful passive approaches and have demonstrated skin friction drag reductions of about 10% in laboratory experiments [8]. The technique was also evaluated in flight tests on transport aircraft, confirming friction drag reductions of 2-6% [76, 79]. Their primary advantages lie in their simplicity, robustness, and practical implementation. Further, they do not require an additional power supply.

Despite these promising results, passive drag-reduction strategies generally provide moderate performance gains and are typically effective only within a narrow operating range. While passive techniques remain attractive due to their energetic neutrality, their overall drag-reduction potential is inherently limited.

Active flow control techniques, in contrast, require an external energy input but offer greater flexibility and the potential for significantly larger performance improvements. Because the actuation can be tuned to a broader range of flow conditions, active methods can be adapted to varying operating points, flow conditions, and geometries. However, their overall benefit must be evaluated by considering both the aerodynamic gains and the energetic cost of actuation. This thesis focuses on two techniques of active flow control, which have been intensively studied during the last few years. Both target the near-wall region of turbulent boundary layers, which dominates viscous drag production, but they rely on fundamentally different mechanisms. The two techniques are uniform wall-normal blowing and suction, and streamwise travelling waves of spanwise velocity (StTW), and will be discussed in more detail in the following subsections.

2.2 Wall-normal homogeneous Blowing and Suction

Among the earliest active flow control methods is wall-normal blowing and suction, in which mass is injected into (blowing) or removed (suction) from the boundary layer through a porous surface. A sketch of this technique is shown in Figure 2.1, where blowing and suction can be observed on a portion of the upper side of an airfoil.

The foundational idea dates back to the work of Prandtl and Betz [55], who proposed suction to stabilize the boundary layer and to prevent flow separation in regions of adverse pressure gradients. They identified suction as an effective method to suppress separation and delay transition. Since skin friction is significantly lower in laminar boundary layers than in turbulent ones, delaying transition directly reduces overall viscous drag.

Early experimental investigations on porous flat plates under zero-pressure-gradient conditions demonstrated that suction reduces the boundary layer thickness while increasing local skin friction, whereas blowing leads to boundary layer thickening and a reduction in skin friction [13, 45]. Black et al. [13] observed that suction pulls the velocity profile toward the wall and thus increases the friction drag, while blowing shifts the profile away from the wall, reducing the velocity gradient at the wall. Furthermore, the results of Prandtl and Betz [55] were confirmed, showing that suction delays laminar-turbulent transition, whereas blowing promotes it [29].

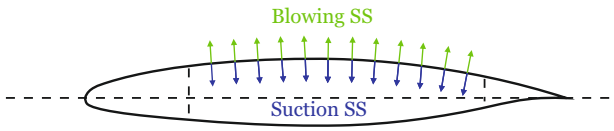


Figure 2.1: Sketch of the blowing and suction control mechanism on the upper side of an airfoil.

As computational resources increased, more detailed numerical investigations became possible. Large-eddy simulations of turbulent channel flows with wall-normal blowing and suction were among the first high-fidelity numerical studies of this control technique [50]. Subsequent direct numerical simulations confirmed the reduction of wall shear stress under blowing in good agreement with experimental data [74]. These findings were later confirmed by numerical simulations by Park et al. [48]. A comparison of uniform blowing to the control technique of body forces damping conducted by Stroh et al. [73] showed that uniform blowing leads to a thickening of the turbulent boundary layer, resulting in a persistent drag reduction that was still observed in the region downstream of where the control was applied. Consequently, uniform blowing demonstrated superior global efficiency.

An important development was the introduction of micro-blowing techniques [33]. Earlier experiments used relatively rough porous materials, which introduced additional surface effects. Micro-blowing was introduced to provide smoother injection surfaces and more controlled mass fluxes. The conducted experiments demonstrated that significant drag reduction could be achieved even at relatively low blowing rates.

Kornilov [40] reported a large skin-friction reduction potential for a turbulent boundary layer over permeable surfaces. A subsequent review confirmed the general trend of local friction drag reduction under blowing and friction increase under suction [39]. Experimental and numerical studies largely agreed on the evolution of local wall friction, even though the implementation differs fundamentally. Experiments use discrete injection holes, whereas simulations typically impose idealized boundary conditions, where the mass is injected or removed uniformly distributed over the surface. However, these studies did not fully address the question of how the injected mass affects the global momentum balance and, consequently, the definition of total drag.

Despite these encouraging results, the majority of investigations on blowing and suction have been limited to simplified geometries such as flat plates or channel flows and have predominantly focused on incompressible or low-speed conditions [32, 35, 45, 73, 74]. In these configurations, friction drag

is the only drag source. Therefore, a reduction in friction drag directly translates to a reduction in overall drag.

When extending such methods to more realistic aerodynamic configurations, such as, for example, airfoils, additional complexity arises. In airfoil flows, surface curvature, pressure gradients, and an additional drag component, the pressure drag, arise and complicate the assessment of control effectiveness. Consequently, a reduction in local skin-friction drag does not necessarily imply a reduction in total aerodynamic drag.

Encouraged by the favorable outcomes observed in simple flow cases and by the simple implementation of the actuation, homogeneous blowing and suction have also been explored in more complex aerodynamic settings. One of the earliest theoretical attempts to extend blowing and suction to more complex geometries was performed by Gertsen and Wiedemann [25], who investigated the theoretical optimization of blowing and suction on a Joukowsky airfoil. Their work represents an early step toward applying active flow control to realistic airfoil configurations. They identified the displacement effect of blowing already known from simpler flow configurations, resulting in a friction drag reduction persisting even downstream of the control region. At the same time, the displacement effect was shown to increase pressure drag, thereby compensating for the favorable reduction in friction drag [71].

Contrary to Spalart et al. [71], numerical investigations via large-eddy simulations (LES) of incompressible flow around a NACA4412 airfoil indicated that uniform blowing applied to the lower surface led to an increase in efficiency [5, 47]. Furthermore, these results were supported by a comprehensive RANS-based parametric analysis, which confirmed the influence of uniform blowing and suction on the individual drag components [18]. The total drag in these numerical studies was obtained by integrating the shear stresses and the pressure along the surface.

Eto et al. [17] observed a reduction in total drag in numerical simulations, but reported difficulties in reproducing these in experiments. A direct measurement of the drag in experiments led to large uncertainties. For the determination of the drag in experiments, a wake-based measurement was used. Discrepancies in the drag measurements were already observed in the review of Hwang [33], who saw good agreement between numerical simulations and experiments when the drag in the experiments was measured by a scale. The corresponding wake measurements showed a drop in pressure, which translated to an increase in drag.

The difference in the drag measurements between numerical simulations and experiments, or in other words, by measuring the drag directly on the body via integrating the stresses, or indirectly from the wake, can only partially be described by uncertainties in the measurements.

The major reason lies in the contribution of blowing to the global momentum balance. If the injected mass originates from an internal source within the airfoil, the wake momentum balance must include the additional mass flux. In such a case, the drag calculated from wake measurements becomes larger than the body drag obtained from surface integration. The difference between drag determined directly at the body and drag inferred from the wake is therefore not only a measurement artifact but a consequence of the modified control-volume balance.

This issue, as well as a corresponding correction of the drag coefficient, has been addressed in detail by Fahland et al. [FAF+23], while the detailed explanation for compressible flows is discussed in Section 4.1.

Modern transport aircraft operate primarily in the transonic regime, where compressibility effects become significant and weak shock waves form on the suction side of the airfoil. These shock waves interact with the turbulent boundary layer and can lead to increased drag and complex flow

phenomena. Despite their practical relevance, such conditions remain comparatively unexplored in the context of wall-normal blowing and suction. However, they form an important basis for making statements about the effectiveness of control in the areas where the applications actually take place.

In this work, the feasibility of wall-normal homogeneous blowing and suction for improving the aerodynamic efficiency of the transonic airfoil RAE2822 is investigated, explicitly accounting for compressibility effects and shock boundary layer interactions. Therefore, a detailed numerical study is conducted where the active flow control method of wall-normal uniform blowing and suction is investigated. The variation of many parameters, such as Mach number, angle of attack, and the control parameters, including the control configurations, magnitude, and position, are investigated. The results of the parametric study are presented in Chapter 5.

2.3 Streamwise Travelling Waves

A large number of friction drag-reducing control methods have been investigated over the last century. One approach, which gained a lot of interest in recent decades, is spanwise forcing. Spanwise forcing and suction have similar effects on the efficiency when applied to an airfoil in transonic flow conditions, but the underlying mechanism is fundamentally different. This raises the question of which mechanisms are essential to achieve an overall increase in efficiency. To address this question, a comparative investigation of the two active control mechanisms is conducted.

Spanwise forcing is based on imposing a space and/or time-dependent spanwise velocity at the wall. The simplest realization is the spanwise oscillating wall, where the wall undergoes spatially uniform but time-varying motion. This configuration was first investigated by Jung et al. [34] and later systematically analyzed by Quadrio and Ricco [57], demonstrating substantial reductions in turbulent skin-friction drag.

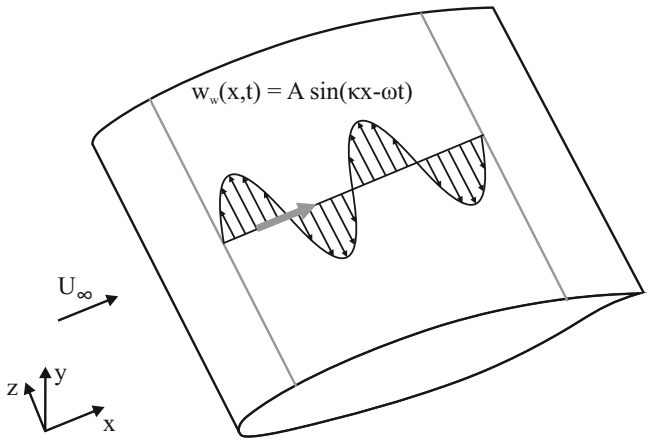


Figure 2.2: Sketch of streamwise travelling waves of spanwise velocity on the upper side of an airfoil.

A more effective extension of this concept is streamwise travelling waves of spanwise velocity, introduced by Quadrio et al. [58]. In this technique, the wall velocity varies in both space and time according to

$$u_{StTW}(x,t) = A_{StTW} \sin(\kappa_x x - \omega t), \tag{2.1}$$

where A_{StTW} is the forcing amplitude, κ_x and ω the spatial and temporal frequencies, respectively, and x and t represent the spanwise coordinate and time. A sketch of the application of StTW on the suction side of an airfoil is shown in Figure 2.2.

The physical mechanism underlying the drag reduction by StTW was qualitatively explained by Quadrio and Ricco [58]. The imposed spanwise motion generates a transversal Stokes layer whose thickness depends on the forcing parameters. The oscillatory shear layer interacts with near-wall turbulence structures, weakening the self-sustaining cycle responsible for turbulence production and thereby reducing wall shear stress.

Extensive numerical and experimental investigations confirmed the effectiveness of spanwise forcing. Experimental validation was first achieved in pipe flow by Auteri et al. [6], who reported a drag reduction of up to 33% using discretized travelling waves generated by independently rotating pipe segments. Subsequent developments included planar actuators based on deformable membranes [12] and spatially discrete implementations suitable for practical applications [38, 42]. These studies contributed to a deeper understanding of actuator realizations and discretization effects.

Most early investigations focused on incompressible turbulent channel or pipe flows at moderate Reynolds numbers [6, 34, 57, 58]. The Reynolds number dependence of the control performance was investigated by Gatti and Quadrio [23], who showed that the drag reduction decreases only moderately with increasing Reynolds number, while the optimal forcing parameters remain nearly Reynolds-number independent when expressed in wall units. Studies of compressible channel flows indicated that spanwise forcing remains effective even in supersonic regimes [82], and recent analysis demonstrated that, when the comparison is performed consistently, the energetic performance of StTW is largely unaffected by compressibility effects [22].

While spanwise forcing was originally conceived as a friction drag reduction technique, more recent research has shown that its impact extends beyond viscous effects. In realistic aerodynamic configurations, total drag includes contributions also from the pressure drag, thus, improving aerodynamic efficiency requires understanding how the control modifies the global pressure field. Banchetti et al. [7] demonstrated by using DNS that friction reduction induced by travelling waves can alter the pressure distribution over non-planar surfaces, as in a channel flow with a bump at the wall, leading to additional energetic benefits beyond local skin-friction reduction.

The interaction between drag reduction techniques and pressure-driven flow phenomena becomes particularly relevant in transonic flows, where shock waves contribute significantly to total drag. Earlier studies suggested that friction drag reduction techniques may affect pressure drag in transonic configurations. A modification of the pressure distribution was reported in an experiment where riblets were applied to a transonic airfoil [43]. RANS investigations further indicated that similar interactions between spanwise forcing and pressure-driven flow features may occur in aircraft configurations. This hypothesis was confirmed by Quadrio et al. [59], who performed DNS of turbulent flow over a modern transonic airfoil with localized StTW. Their results revealed a downstream displacement and intensification of the shock wave, accompanied by changes in both friction and pressure distributions along the surface. A comparison at the same lift coefficient, by adjusting the angle of attack, showed a net drag reduction of approximately 9%.

Extending earlier studies, a detailed DNS study of a transonic airfoil with StTW applied on the suction side confirmed that the control shifts the shock wave on the suction side toward the trailing edge, thereby enhancing aerodynamic efficiency [10].

The coexistence of similar aerodynamic improvements produced by wall-normal suction and streamwise travelling waves raises fundamental questions regarding the dominant physical mechanisms

responsible for efficiency gains. In transonic flows, local friction drag reductions alone do not appear to be the primary driver of performance enhancement. Instead, modifications of boundary layer thickness, pressure distribution, and shock wave interactions seem to play a decisive role.

These observations motivate a comparative analysis of wall-normal suction and streamwise travelling waves under compressible and transonic conditions, to identify the mechanisms governing improved aerodynamic efficiency. The results of the DNS study of the turbulent flow around the supercritical airfoil V2C are presented in Chapter 6.

3 Governing Equations and Flow Physics

3.1 Conservation Equations

The fundamental equations of fluid mechanics are based on general conservation laws. These laws can be formulated for a control mass, a fixed system with a constant mass. The shape and the position of the control mass can change with time, but its identity remains constant.

For an extensive property Φ, such as e.g. mass, momentum, or energy, the conservation principle states that the rate of change of this property equals the external effects acting on the control mass.

The mass m of a control mass remains constant, so it is neither created nor destroyed in the observed control mass, which means that mass is conserved [72]

$$\frac{\mathrm{d}m}{\mathrm{d}t} = 0. \tag{3.1}$$

The momentum conservation follows from Newton's second law

$$\frac{\mathrm{d}}{\mathrm{d}t}(m\vec{u}) = \sum \vec{F}, \tag{3.2}$$

with the velocity $\vec{u}$ of the control mass and the external forces $\vec{F}$. So the momentum can be changed by forces acting on the control mass.

The use of a control mass is difficult in fluid mechanics, since the fluid particles move and deform all the time. Therefore, the conservation laws are reformulated using a control volume. A control volume covers a fixed region in space where fluid can flow through. The relation between the control mass and control volume description is established by the Reynolds Transport Theorem. In a control volume, the considered properties are intensive, meaning they are independent of the amount of mass that is considered.

3.1.1 Reynolds Transport Theorem

The intensive property ϕ is considered. The corresponding extensive property Φ per unit mass can be calculated by [19]

$$\Phi = \iiint_{V(t)} \rho\phi \, \mathrm{d}V, \tag{3.3}$$

where $V(t)$ is the volume occupied by the control mass. The Reynolds Transport Theorem relates the rate of change of the property of the system to quantities defined over a control volume [20]

$$\frac{\mathrm{d}\Phi}{\mathrm{d}t} = \frac{\mathrm{d}}{\mathrm{d}t} \iiint_{V(t)} \rho\phi \, \mathrm{d}V = \frac{\partial}{\partial t} \iiint_{V} \rho\phi \, \mathrm{d}V + \iint_{A} \rho\phi(\vec{u} \cdot \hat{n}) \, \mathrm{d}A, \tag{3.4}$$

where V is the fixed volume and A is the surface of the control volume. $\hat{n}$ is the unit vector normal to the surface directed outward, and $\vec{v}$ is the velocity of the fluid. The first term represents the rate of change of the property inside the control volume, and the second term represents the net flux through the control surface. This theorem is the basis for deriving the conservation equations in the control volume form.

3.1.2 Conservation of Mass

For the conservation of mass, the intensive property is $\phi = 1$. Using the Reynolds Transport Theorem 3.4 leads to the integral form of the mass conservation equation [19]

$$\frac{\partial}{\partial t} \iiint_V \rho \, \mathrm{d}V + \iint_A \rho(\vec{u} \cdot \hat{n}) \, \mathrm{d}A = 0. \tag{3.5}$$

This equation means that the sum of the rate of change of mass inside the control volume and the net mass flux through the control surface is zero, meaning no mass is created or removed inside the control volume. By using Gauss' divergence theorem for the convection term, the surface integral can be transformed into a volume integral, thus, the equation can be converted into its differential form. Assuming an infinitesimally small control volume, the differential form can be derived to [72]

$$\frac{\partial \rho}{\partial t} + \nabla \cdot (\rho \vec{u}) = 0. \tag{3.6}$$

Using the material derivative $\frac{\mathrm{D}}{\mathrm{D}t} = \frac{\partial}{\partial t} + \vec{u} \cdot \nabla$ leads to a different form of the continuity equation

$$\frac{\mathrm{D}\rho}{Dt} + \rho(\nabla \cdot \vec{u}) = 0 \tag{3.7}$$

If $\frac{\mathrm{D}\rho}{Dt} = 0$ holds, the density of a fluid parcel remains constant along its trajectory. Under this assumption, the continuity equation simplifies to $\nabla \cdot \vec{u} = 0$, which represents the incompressibility condition for volume-preserving flows.

3.1.3 Conservation of Momentum

For momentum conservation, the extensive property is the momentum $\vec{I}$ of the fluid system. The corresponding intensive property per unit mass is the velocity vector $\phi = \vec{u}$. Thus the total momentum $\vec{I}$ of the material mass can be calculated by

$$\vec{I} = \iiint_{V(t)} \rho \vec{u} \, \mathrm{d}V. \tag{3.8}$$

According to Newton's second law, the rate of change of the momentum of the system equals the sum of all external forces

$$\frac{\mathrm{d}\vec{I}}{\mathrm{d}t} = \sum \vec{F}. \tag{3.9}$$

The external forces consist of two classes: the body forces and the surface forces. The body forces act on every fluid particle in the volume and are proportional to the mass of the fluid. They

originate from external forces, such as gravitational, electric, or magnetic fields. The body force per unit mass is denoted by $\vec{k}$. The total body force $\vec{F}_{body}$ can be calculated as follows [72]

$$\vec{F}_{body} = \iiint_V \rho\vec{k} \, \mathrm{d}V. \tag{3.10}$$

Within fluid mechanics, gravity is the dominant body force in most cases, leading to $\vec{k} = \vec{g}$.

Surface forces act on the boundary of the control volume and represent the interaction between the fluid and the surroundings. These forces arise from stresses within the fluid and are described by $\vec{t}$, representing the force per unit area acting on a surface element [72]

$$\vec{F}_{surf} = \iint_A \vec{t} \, \mathrm{d}A. \tag{3.11}$$

Surface forces include both pressure forces in the normal direction and viscous forces in the tangential direction.

Applying the Reynolds Transport Theorem 3.4 and Newton's second law to the integral form of the momentum equation leads to [19]

$$\frac{\partial}{\partial t} \iiint_V \rho\vec{u} \, \mathrm{d}V + \iint_A \rho\vec{u}(\vec{u} \cdot \hat{n}) \, \mathrm{d}A = \iiint_V \rho\vec{k} \, \mathrm{d}V + \iint_A \vec{t} \, \mathrm{d}A. \tag{3.12}$$

The first term on the left-hand side of the equation describes the rate of change of momentum inside the control volume, while the second term represents the net momentum flux through the control surface due to fluid motion. The right-hand side terms correspond to the external forces acting on the fluid.

The surface forces arising from the stresses and pressure are described by $\vec{t}$. These fluxes must be written in terms of conserved properties to get a closed system of equations. Therefore, the assumption of a Newtonian fluid, which is valid for many fluids, is made. The stress tensor $\mathbf{T}$ can be written as follows [72]

$$\mathbf{T} = -p\mathbf{1} + \tau, \tag{3.13}$$

with the identity matrix $\mathbf{1}$, the pressure p and the wall shear stress τ_w. For a Newtonian fluid, the viscous stresses are linearly related to the rate of deformation [19]

$$\tau = \mu(\nabla\vec{u} + (\nabla\vec{u})^T) - \frac{2}{3}\mu(\nabla \cdot \vec{u})\mathbf{1}, \tag{3.14}$$

with the dynamic viscosity μ.

Substituting this relation into the momentum equation and using Gauss' divergence theorem leads to the differential form of the momentum equation [19]

$$\frac{\partial(\rho\vec{u})}{\partial t} + \nabla \cdot (\rho\vec{u}\vec{u}) = \nabla \cdot \mathbf{T} + \rho\vec{k} = -\nabla p + \nabla\tau + \rho\vec{k}. \tag{3.15}$$

This equation is called the compressible Navier-Stokes equation. For an incompressible flow, where $\nabla \cdot \vec{v} = 0$ is valid, the Navier-Stokes equation simplifies to

$$\rho\left(\frac{\partial\vec{u}}{\partial t} + (\vec{u} \cdot \nabla)\vec{u}\right) = -\nabla p + \mu\nabla^2\vec{u} + \rho\vec{k}. \tag{3.16}$$

3.1.4 Conservation of Energy

The conservation of energy is based on the first law of thermodynamics, which states that energy cannot be created or destroyed, it can only be converted from one form into another. The total energy of a fluid particle consists of two main components, the internal energy e and the kinetic energy $\frac{u^2}{2}$, so the total energy per unit mass is the intensive property

$$\phi = e + \frac{|\vec{u}|^2}{2}. \tag{3.17}$$

The total energy of a control mass with a volume $V(t)$ is (here $\Phi = E_{tot}$) [19]

$$E_{tot} = \iiint_{V(t)} \rho \left(e + \frac{|\vec{u}|^2}{2} \right) \, \mathrm{d}V. \tag{3.18}$$

The rate of change of the energy is determined by two mechanisms, the mechanical work done by forces and heat transfer.

The forces acting on the control volume are the same as for momentum conservation: the body forces and the surface forces. The rate of work done is [72]

$$W = \iiint_V \rho \vec{u} \cdot \vec{k} \, \mathrm{d}V + \iint_A \vec{u} \cdot \vec{t} \, \mathrm{d}A. \tag{3.19}$$

Energy can also enter or leave the control volume in the form of heat. Heat transfer is described by the heat flux vector $\vec{q}$, which describes the heat flow per unit area. The net heat flux into the control volume is

$$\dot{Q} = - \iint_A \vec{q} \cdot \hat{n} \, \mathrm{d}A. \tag{3.20}$$

The negative sign ensures that heat entering the control volume is counted as positive.

Applying the Reynolds Transport Theorem and the first law of thermodynamics, the energy conservation equation is derived to [72]

$$\frac{\mathrm{D}}{\mathrm{D}t} \iiint_{V(t)} \rho \left(e + \frac{|\vec{u}|^2}{2} \right) \, \mathrm{d}V = W + \dot{Q} = \iiint_V \rho \vec{u} \cdot \vec{k} \, \mathrm{d}V + \iint_A \vec{u} \cdot \vec{t} \mathrm{d}A - \iint_A \vec{q} \cdot \hat{n} \, \mathrm{d}A. \tag{3.21}$$

The left-hand side of the equation describes the rate of change of energy in the control volume and the energy transport by fluid motion, while the right-hand side describes the energy that is added through mechanical work or heat transfer. Applying Gauss' divergence theorem and using the definition of the stress tensor 3.13 to the integral form of the energy equation, the differential equation is derived to

$$\frac{\mathrm{D}}{\mathrm{D}t} \left[\rho \left(e + \frac{\vec{u}^2}{2} \right) \right] = \rho \vec{k} \cdot \vec{u} + \nabla \cdot (\mathbf{T} \cdot \vec{u}) - \nabla \cdot \vec{q}. \tag{3.22}$$

3.2 Aerodynamic equations

3.2.1 Lift and Drag coefficients

The total aerodynamic force $\vec{F}_{tot}$ is determined by integrating the pressure p and wall shear stress τ_w over the entire surface A of the body

$$\vec{F}_{tot} = \iint_A (-p\hat{n} + \tau_w \hat{t}) \, \mathrm{d}A, \tag{3.23}$$

with $\hat{n}$ as the unit normal vector pointing outward and $\hat{t}$ as the unit tangential vector along the surface. The wall shear stress is defined as [31]

$$\tau_w = \mu \frac{\partial \vec{u}}{\partial n}. \tag{3.24}$$

The total force can be decomposed into three components. The lift component F_L, which is perpendicular to the freestream, the drag component F_D, which is parallel to the freestream, and the side force F_S, which is perpendicular to the other two force components. For a two-dimensional airfoil in symmetric flow, the side force is zero and therefore neglected here.

The lift c_L and drag c_D coefficients are defined using the freestream dynamic pressure $q_\infty = \frac{1}{2}\rho_\infty U_\infty^2$ [65]

$$c_L = \frac{F_L}{\frac{1}{2}\rho_\infty U_\infty^2}, \tag{3.25}$$

$$c_D = \frac{F_D}{\frac{1}{2}\rho_\infty U_\infty^2}, \tag{3.26}$$

with the freestream density ρ_∞ and the freestream velocity U_∞.

The drag coefficient consists of two components, the pressure and skin-friction drag. Pressure drag originates from the pressure distribution over the airfoil surface, whereas skin-friction drag results from viscous shear stress. Both components are obtained by integrating the corresponding surface forces and projecting them onto the streamwise direction

$$c_{D,p} = -\frac{\iint_A p(\hat{n} \cdot \hat{e}_x) \, \mathrm{d}A}{\frac{1}{2}\rho_\infty U_\infty^2}, \tag{3.27}$$

$$c_{D,f} = \frac{\iint_A \tau_w(\hat{n} \cdot \hat{e}_x) \, \mathrm{d}A}{\frac{1}{2}\rho_\infty U_\infty^2}, \tag{3.28}$$

with $\hat{e}_x$ the unity vector in streamwise direction.

The aerodynamic efficiency E is described by the lift-to-drag ratio

$$E = \frac{F_L}{F_D} = \frac{c_L}{c_D}, \tag{3.29}$$

which represents the amount of lift generated per unit drag.

3.2.2 Mach and Reynolds number

In addition to the aerodynamic force coefficients, two important dimensionless parameters are used to characterize the flow conditions.

The Mach number Ma is a dimensionless velocity parameter that indicates the relevance of compressibility effects. It is defined as the ratio of the local flow velocity magnitude to the speed of sound a in the medium

$$Ma = \frac{|\vec{u}|}{a}. \tag{3.30}$$

For an ideal gas, the speed of sound is given by

$$a = \sqrt{\gamma \frac{p}{\rho}}, \tag{3.31}$$

where γ is the ratio of specific heats. The Mach number can also be interpreted as the square root of the ratio between the inertial and elastic forces

$$Ma = \sqrt{\frac{\text{inertial forces}}{\text{elastic forces}}}. \tag{3.32}$$

The Reynolds number Re characterizes viscous flow behavior and represents the ratio of inertial to viscous forces

$$Re = \frac{\rho |\vec{u}| l}{\mu}, \tag{3.33}$$

where l is the characteristic length scale. It can also be interpreted as the ratio of the convective momentum transport to the diffusive momentum transport in the flow. Consequently, it governs the relative importance of viscous effects compared to inertial effects.

3.3 Turbulent Boundary Layers in Compressible Flows

3.3.1 General Introduction to Turbulence

Turbulent flows are characterized by enhanced diffusion, strong three-dimensionality, unsteadiness, and a vortex-dominated flow structure. In a laminar flow, small disturbances decay, and the motion of fluid particles remains ordered. In the region of transition, disturbances can be amplified once a critical Reynolds number is exceeded, leading to transition and the development of turbulent flow.

A fundamental feature of turbulence is the stochastic behavior of flow quantities such as velocity, pressure, and temperature. Although the instantaneous flow field is irregular and time-dependent, it can be decomposed into a mean component and a fluctuating component using Reynolds decomposition, which was first introduced by Reynolds [61]

$$u_i = \overline{u_i} + u_i', \tag{3.34}$$

where $\overline{u_i}$ denotes the mean velocity and u_i' represents the fluctuating component.

For statistically stationary flows, the mean velocity is obtained by temporal averaging at a fixed spatial location x_j

$$\overline{u}_i = \frac{1}{t} \int u_i(t) \, \mathrm{d}t, \tag{3.35}$$

where the averaging interval T must be large compared to the characteristic turbulent time scales.

The fluctuating velocity components generate additional momentum transport through Reynolds stresses, which act analogously to turbulent stress and significantly modify the mean flow behavior in wall-bounded flows compared to laminar ones.

In compressible flows, turbulence is additionally influenced by variations in density and temperature. At higher Mach numbers, compressibility effects become relevant and modify the structure and dynamics of turbulence, for example, through density fluctuations and additional coupling between momentum and thermodynamic variables.

Thus, both Reynolds number and Mach number influence the development of turbulent boundary layers in compressible flows, with the Reynolds number primarily governing the transition to turbulence and the Mach number determining the importance of compressibility effects.

3.3.2 Boundary Layer in Compressible Flow

A boundary layer forms when a viscous fluid flows over a solid surface. Due to the no-slip condition, the velocity at the wall is zero and increases toward the external flow velocity within a thin region close to the surface. For a flat plate aligned with the flow, the boundary layer thickness grows with increasing downstream coordinate x.

In compressible flows, the boundary layer is characterized not only by strong velocity gradients but also by significant temperature and density gradients. These arise from viscous dissipation and wall heat transfer. Consequently, thermodynamic properties vary across the boundary layer and influence its development.

The wall boundary condition plays a crucial role. For an isothermal wall, the wall temperature is prescribed, resulting in heat exchange between the wall and fluid. An adiabatic wall is characterized by the absence of heat flux across the wall, the wall temperature adjusts to the temperature of the flow.

Since viscosity μ depends on temperature, it varies within the boundary layer. This dependence is commonly described by Sutherland's law, which relates dynamic viscosity to temperature [75]

$$\mu = \mu_0 \frac{T_0 + C}{T + C} \left(\frac{T}{T_0} \right)^{\frac{3}{2}}, \tag{3.36}$$

where μ_0 is the dynamic viscosity at a reference temperature T_0. The actual temperature is T, and C is the Sutherland constant. At a reference temperature of $T_0 = 291.15K$, the Sutherland constant is $C = 120$.

3.3.3 Boundary Layer Thickness Definitions

The boundary layer describes the thin region close to the surface in which viscous effects are significant, and velocity gradients are large. Since the boundary layer does not have a sharply defined

outer edge, its thickness cannot be uniquely specified. Instead, several characteristic measures have been introduced, each emphasizing different physical aspects of the flow, such as velocity deficit, mass flux, or momentum loss. These integral thickness measures provide a quantitative framework for analyzing boundary layer development. In the following, the most commonly used definitions are introduced.

3.3.3.1 Geometric Boundary Layer Thickness

The geometric boundary layer thickness δ_{99} is defined as the distance from the wall to the location where the velocity of the flow reaches 99% of the external velocity U_e

$$u_{y=\delta_{99}} = 0.99U_e. \tag{3.37}$$

Although this 99% criterion is arbitrary, it is widely adopted in engineering applications. The term geometric boundary layer thickness refers to the fact that this definition is based purely on a spatial location within the velocity field, rather than on an integral or analytic property of the boundary layer.

3.3.3.2 Displacement Thickness

The displacement thickness δ^* accounts for the reduction in mass flow caused by the boundary layer. For compressible flow, it is defined as [69]

$$\delta^* = \int_0^\infty \left(1 - \frac{\bar{\rho}\tilde{u}}{\rho_e U_e}\right) \mathrm{d}n, \tag{3.38}$$

where $(\bar{})$ and $(\tilde{})$ denote the Reynolds-averaged and Favre-averaged quantities, respectively, and ρ_e and U_e denote density and velocity at the boundary layer edge. n defines the normal direction of the surface, where the boundary layer forms. Physically, δ^* represents the outward displacement of the external inviscid streamlines due to the presence of the boundary layer and is therefore a measure of blockage.

3.3.3.3 Momentum Thickness

The momentum thickness θ describes the reduction in momentum flux within the boundary layer compared to an inviscid flow [69]

$$\theta = \int_0^\infty \left(1 - \frac{\tilde{u}}{U_e}\right) \frac{\bar{\rho}\tilde{u}}{\rho_e U_e} \mathrm{d}n. \tag{3.39}$$

The momentum thickness is directly related to skin friction drag and appears as a central quantity in the integral boundary layer equations, where it characterizes the momentum deficit of the boundary layer.

3.3.3.4 Shape Factor

The shape factor H is defined as

$$H = \frac{\delta^*}{\theta}. \tag{3.40}$$

It provides information about the state of the boundary layer. A high shape factor indicates a boundary layer approaching separation, particularly under adverse pressure gradients.

3.3.4 Viscous Scaling

Near the wall, the turbulent boundary layer exhibits similarity when expressed in viscous units. The wall shear stress τ_w defines the friction velocity

$$u_\tau = \sqrt{\frac{\tau_w}{\rho_w}}, \tag{3.41}$$

where ρ_w is the density at the wall.

Dimensionless wall coordinates are marked with a + superscript and are defined as

$$u^+ = \frac{\overline{u}}{u_\tau}, \tag{3.42}$$

$$y^+ = \frac{y u_\tau}{\nu_w}, \tag{3.43}$$

with ν_w being the kinematic viscosity evaluated at the wall.

Using this scaling, the velocity profile of the boundary layer can be divided into three sections. The viscous sublayer ($y^+ < 5$) is very close to the wall, and the viscous stresses dominate momentum transport. In the logarithmic layer ($y^+ > 70$), the Reynolds stresses dominate momentum transport. The buffer layer ($5 < y^+ < 70$) forms the transition region where viscous and turbulent stresses are of comparable magnitude. The outer region is mainly influenced by external flow conditions and pressure gradients. A normalized mean velocity profile of a turbulent boundary layer is shown in Figure 3.1.

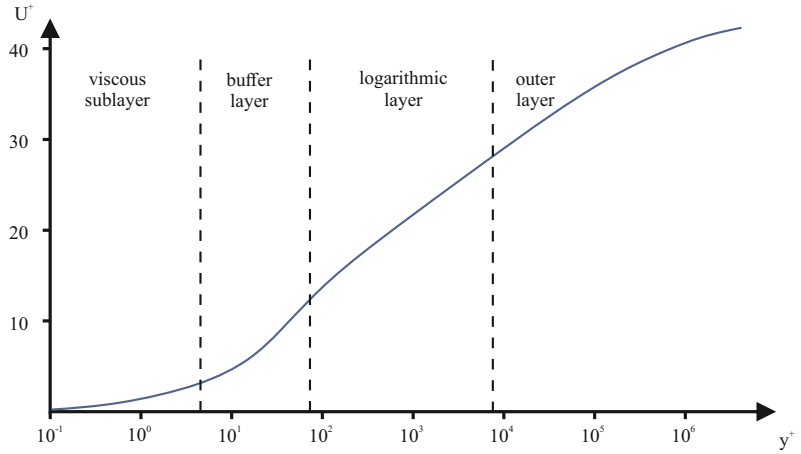


Figure 3.1: Sketch of a normalized mean velocity profile of a turbulent boundary layer.

3.3.5 Laminar-Turbulent Transition

Transition describes the process by which a laminar boundary layer becomes turbulent. For a flat plate under low-disturbance conditions, transition typically occurs at a critical Reynolds number of approximately $Re_x \approx 5 \times 10^5$, although the exact value depends on environmental conditions.

Natural transition proceeds through instability mechanisms such as Tollmien-Schlichting waves, which evolve into three-dimensional vortical structures and turbulent spots before forming a fully turbulent boundary layer [69].

The place where transition takes place is influenced by many parameters, such as Reynolds number, pressure distribution, surface roughness, turbulence level in the freestream, and Mach number.

In addition to natural transition mechanisms, transition can be enforced to ensure a prescribed laminar-turbulent change within the boundary layer. In experimental investigations, this is achieved by introducing disturbances, for example, by placing a thin roughness element as a thread on the surface to trip the boundary layer at a prescribed location. A comparable strategy can be adopted in numerical simulations to ensure a controlled laminar-turbulent transition.

To enforce transition, a localized turbulent kinetic energy (TKE) source term is introduced. Upstream of the transition location, laminar flow is maintained by prescribing a negligibly small turbulence level. At the tripping location, transition is triggered through the introduction of an additional source term $S_{k,a}$ in the TKE transport equation [49].

The source term $S_{k,a}$ is implemented as a semi-explicit scalar source, where only the explicit contribution is considered [49]. It is spatially restricted to a finite region around the prescribed transition location in the streamwise direction. In the normal direction, it extends from the local momentum thickness θ to twice its value. Within this region, a constant source magnitude is prescribed, while it is set to zero elsewhere.

The introduction of this localized TKE source enforces an immediate transition to turbulence at the specified location.

3.3.6 Flow Separation

Flow separation occurs when a boundary layer is subjected to a sufficiently strong adverse pressure gradient, such that the fluid particles in the near-wall region are no longer able to overcome the increasing pressure in the streamwise direction. As a result, the flow decelerates and eventually reverses direction.

From a physical perspective, separation is governed by the balance between inertial forces and viscous effects within the boundary layer. Fluid elements near the wall possess less momentum compared to those in the outer region due to viscous dissipation. When an adverse pressure gradient is imposed, the outer flow is decelerated, and the reduced momentum transport toward the wall is no longer sufficient to sustain forward motion in the near- wall region. Consequently, the velocity gradient at the wall decreases.

The evolution of the velocity profile provides further insights into the separation process. In an attached boundary layer, the velocity increases monotonically from zero at the wall to the external value. As the adverse pressure gradient strengthens, the velocity profile becomes progressively less steep near the wall and develops an inflection point. At the point of separation, the wall shear stress vanishes

$$\tau_w = \mu \left. \frac{\partial u}{\partial n} \right|_{n=0} = 0, \tag{3.44}$$

which implies that the velocity gradient at the wall is zero. Downstream of this point, the velocity gradient becomes negative, indicating flow reversal in a finite region adjacent to the wall.

In practical applications, separation is often identified using the skin friction coefficient

$$c_f = \frac{\tau_w}{\frac{1}{2}\rho U^2}. \tag{3.45}$$

At the point of separation, c_f approaches zero, while negative values indicate reversed flow. In addition, integral boundary layer parameters exhibit characteristic behavior. The displacement thickness increases significantly while the momentum thickness increases moderately, leading to a rise in the shape factor H when separation is approached.

Downstream of the separation point, a recirculation zone is typically formed, leading to the development of a separation bubble. Within this region, the flow is characterized by a closed streamline pattern and low momentum. At the reattachment point, the reversed flow region ends, and the wall shear stress becomes positive again.

A fundamental distinction exists between laminar and turbulent boundary layers with respect to separation behavior. Laminar boundary layers are more susceptible to separation, as they lack the strong mixing mechanisms that transport high-momentum fluid from the outer region toward the wall. In contrast, turbulent boundary layers exhibit enhanced momentum transport due to Reynolds stresses, which increases their resistance to adverse pressure gradients and delays separation.

The accurate identification of separation and reattachment locations, as well as the characterization of the associated flow structures, is of central importance for the analysis of wall-bounded flows.

3.3.7 Shock-Boundary Layer Interaction

In compressible flows, shock waves can interact with the boundary layer, giving rise to complex flow phenomena collectively referred to as shock-boundary layer interaction. These interactions are of fundamental importance in fluid dynamics and occur in many practical applications such as transonic airfoils, supersonic intakes, and hypersonic vehicles.

When a supersonic flow encounters a shock, the static pressure increases abruptly across the shock, while the flow velocity decreases. Although the outer inviscid flow adjusts nearly instantaneously to this pressure rise, the boundary layer responds more gradually due to viscous effects and its limited momentum near the wall. This mismatch leads to a thickening of the boundary layer and may induce flow separation if the imposed pressure gradient is sufficiently strong.

Depending on the strength of the interaction and the properties of the incoming boundary layer, different regimes can be distinguished. In weak shock-boundary layer interactions, the boundary layer remains attached, and the primary effect is a moderate increase in boundary layer thickness. In contrast, strong interactions result in flow separation upstream of the shock impingement location, leading to the formation of a recirculation region.

In separated interactions, the shock structure becomes more complex and typically assumes a characteristic λ-shape. This configuration consists of a leading separation shock and a downstream reattachment shock, enclosing a recirculation region. The interaction between shock waves and separated flow is a canonical example of a strong viscous-inviscid interaction and has been extensively studied in both experiments and numerical simulations.

The separated flow region is associated with a plateau in the wall pressure distribution, which is commonly used as a diagnostic feature in experimental and numerical studies. Within this region, the flow is highly non-equilibrium and exhibits strong gradients in velocity, pressure, and

turbulence quantities. Downstream of the reattachment point, the boundary layer redevelops and gradually returns to an equilibrium turbulent state.

An important characteristic of shock-boundary layer interactions is their inherently unsteady behavior. Even under nominally steady free-stream conditions, the interaction region may exhibit low-frequency oscillations of the shock system and the separation bubble. These oscillations are associated with significant wall pressure fluctuations and can affect aerodynamic performance and structural loading.

The behavior of shock-boundary layer interactions is governed by several parameters, including Mach number, Reynolds number, and shock strength. Higher Mach numbers generally increase compressibility effects and amplify the interaction, while higher Reynolds numbers tend to stabilize the boundary layer and delay separation. Additionally, the incoming boundary layer thickness and turbulence level strongly influence the interaction characteristics.

Due to their strong impact on boundary layer development, separation, and wall pressure distribution, shock-boundary layer interactions represent a key phenomenon in high-speed aerodynamics. A detailed understanding of these interactions is therefore essential for the analysis and interpretation of the flow configurations considered in the present work.

3.4 Turbulence Modeling

3.4.1 Turbulence Modeling Approaches

Turbulent flow contains structures over a wide range of spatial and temporal scales. Large turbulent eddies contain most of the kinetic energy and are responsible for the transport of momentum and energy within the flow. Through nonlinear interactions, energy is transferred from these large eddies to smaller structures until the smallest scales of turbulence are reached, which are known as the Kolmogorov scales, where energy is dissipated into heat.

Accurately resolving all turbulent scales in numerical simulations requires extremely fine spatial and temporal resolution. For most engineering applications, particularly at high Reynolds numbers, resolving the entire range of scales is computationally infeasible. Therefore, different numerical approaches have been developed to approximate the influence of unresolved turbulent structures on the mean flow.

These approaches differ primarily in the range of turbulence scales that are resolved and those that are modeled. The most commonly used approaches are Direct Numerical Simulations (DNS), Large Eddy Simulations (LES), and Reynolds-Averaged Navier-Stokes (RANS) simulations. The choice of the turbulence modeling approach represents a trade-off between computational cost and physical accuracy.

3.4.2 Direct Numerical Simulations

Direct Numerical Simulations represent the most fundamental approach for simulating turbulent flows. In DNS, the Navier-Stokes equations are solved directly without any turbulence modeling or averaging, meaning that all spatial and temporal scales of turbulence are fully resolved.

To capture the entire turbulent kinetic energy spectrum, the computational mesh and time step must be sufficiently small to resolve even the smallest turbulent structures, the Kolmogorov scales.

As a result, DNS requires extremely fine spatial discretizations and very small time steps, and thus is computationally expensive.

Since the smallest turbulent scales become progressively smaller as the Reynolds number increases, the computational cost of DNS grows rapidly with Reynolds number. Consequently, DNS is generally limited to flows with relatively low Reynolds numbers and simple geometries.

Despite these limitations, DNS provide the most accurate numerical representation of turbulent flows and is often used as a reference for validating turbulence models and numerical methods.

3.4.3 Large Eddy Simulations

Large Eddy Simulations represent an intermediate approach between DNS and RANS. In LES, the large energy-containing turbulence structures are resolved directly, while the smaller scales are modeled.

The underlying idea of LES is that the largest turbulent eddies depend strongly on the geometry and boundary conditions of the flow and therefore must be resolved accurately. In contrast, the smaller scales of turbulence are more universal and can be modeled using subgrid-scale models.

LES is typically implemented by applying a spatial filtering operation to the Navier-Stokes equations, separating the flow field into resolved large-scale structures and unresolved subgrid-scale motions. The unresolved effects are then represented using turbulence models such as the Smagorinsky model.

Compared to DNS, LES significantly reduces computational cost because the smallest turbulent scales do not need to be resolved.

3.4.4 Reynolds-Averaged Navier-Stokes Simulations

In Reynolds-Averaged Navier-Stokes simulations, the instantaneous flow variables are decomposed into a mean part and a fluctuating part using Reynolds decomposition 3.35. For compressible flows, density-weighted (Favre) averaging is employed, in which the flow variables are decomposed into a density-weighted mean component and a corresponding fluctuating component. Applying the Favre averaging to the compressible Navier-Stokes equations yields transport equations for the mean flow.

In conservative form, the Favre-averaged RANS equations read [80]

$$\frac{\partial \bar{\rho}}{\partial t} + \frac{\partial}{\partial x_j}\bar{\rho}\tilde{u}_j = 0, \tag{3.46}$$

$$\frac{\partial}{\partial t}(\bar{\rho}\tilde{u}_i) + \frac{\partial}{\partial x_j}(\bar{\rho}\tilde{u}_i\tilde{u}_j + \bar{p}\delta_{ij} - \tilde{\tau}_{ij}) = -\frac{\partial}{\partial x_j}(\widetilde{\bar{\rho}u_i''u_j''}), \tag{3.47}$$

$$\frac{\partial}{\partial t}(\bar{\rho}\tilde{E}) + \frac{\partial}{\partial x_j}\left[(\bar{\rho}\tilde{E} + \bar{p})\tilde{u}_j - \tilde{u}_i\tilde{\tau}_{ij} + \tilde{q}_j\right] = -\frac{\partial}{\partial x_j}\left(\widetilde{\bar{\rho}u_j''h''}\right), \tag{3.48}$$

where $\bar{\rho}$ and $\bar{p}$ denote the Reynolds-averaged density and pressure, $\tilde{u}_i$ the Favre-averaged velocity components, and $\tilde{E}$ the Favre-averaged total energy per unit mass. Here, $\delta_{i,j}$ is the Kronecker delta and h'' denotes the Favre fluctuations of the specific enthalpy. Repeated indices imply summation according to the Einstein summation convention.

Compared to the laminar Navier-Stokes equations, the averaging procedure introduces additional unknown correlations arising from turbulent fluctuations. These include the Reynolds stress tensor, $\bar{\rho}\widetilde{u_i'' u_j''}$, in the momentum equations and the turbulent heat flux, $\bar{\rho}\widetilde{u_j'' h''}$, in the energy equation. These terms cannot be obtained directly from the mean flow variables and therefore require turbulence models to close the system of equations.

RANS simulations model the effects of the entire turbulence spectrum on the mean flow rather than resolving individual turbulent structures. Consequently, they are computationally efficient and remain the most widely used approach in engineering applications.

3.4.5 Turbulence model

In the present work, turbulence is modeled using the $k-\omega$ Shear Stress Transport (SST) model proposed by Menter [44]. This model combines the advantages of the $k-\omega$ formulation near solid walls with the more robust behavior of the $k-\epsilon$ model in the outer flow region. Consequently, it provides accurate predictions of attached boundary layers while maintaining good performance in the presence of adverse pressure gradients and flow separation.

The model is based on two transport equations. The first equation governs the turbulent kinetic energy k, which represents the kinetic energy contained in the turbulent velocity fluctuations. The second equation describes the specific dissipation rate ω, defined as the rate of turbulent kinetic energy dissipation per unit turbulent kinetic energy. The transport equations are given by [44]

$$\frac{\partial(\rho k)}{\partial t} + \frac{\partial(\rho k u_j)}{\partial x_j} = P_k - \beta^* \rho k \omega + \frac{\partial}{\partial x_j}\left[(\mu + \sigma_k \mu_t)\frac{\partial k}{\partial x_j}\right], \tag{3.49}$$

$$\frac{\partial(\rho \omega)}{\partial t} + \frac{\partial(\rho \omega u_j)}{\partial x_j} = \alpha \frac{\omega}{k} P_k - \beta \rho \omega^2 + \frac{\partial}{\partial x_j}\left[(\mu + \sigma_\omega \mu_t)\frac{\partial \omega}{\partial x_j}\right] + D_\omega, \tag{3.50}$$

where μ_t is the Eddy viscosity. The model constants α, β, β^*, σ_k, and σ_ω determine the relative contributions of production, dissipation, and diffusion. The term P_k denotes the production of turbulent kinetic energy, and D_ω is the cross-diffusion term.

The turbulent eddy viscosity is computed as

$$\mu_t = \frac{\rho k}{\max(\omega, F_2 S)} \tag{3.51}$$

where S is the invariant measure of the strain stress and F_2 is a blending function that limits the Eddy viscosity in regions with strong adverse pressure gradients, thereby improving the predictions of separated flows.

The $k-\omega$-SST model is widely used in aerodynamic applications because it combines robustness with good predictive accuracy for wall-bounded flows. In particular, it has been shown to provide reliable results for boundary layers subjected to adverse pressure gradients and moderate flow separation.

3.4.6 Comparison of Turbulence Modeling Approaches

The three approaches differ primarily in the range of turbulent scales that are resolved and the associated computational cost.

DNS provides the highest level of physical accuracy but is limited to fundamental studies due to its high computational cost. LES offers a balance between accuracy and cost by resolving the dominant turbulent structures. RANS simulations, while less detailed, remain the most practical approach for many engineering applications due to their computational efficiency.

4 Numerical methods

4.1 Momentum Budget Airfoil

The momentum budget analysis for an airfoil presented in this section is based on work that has been previously published in a journal article, to which the author of this thesis contributed as a co-author. References to the original publication Fahland et al. [FAF+23] are provided, and the reader is encouraged to consult the paper for further details and more context.

The integral momentum balance for the flow around a two-dimensional airfoil using the control volume ABCD, see Figure 4.1, is analyzed. The freestream direction coincides with the $\overline{x}$ axis and therefore defines the direction of the drag force F_D. The perpendicular direction, denoted by $\overline{y}$, corresponds to the lift force F_L.

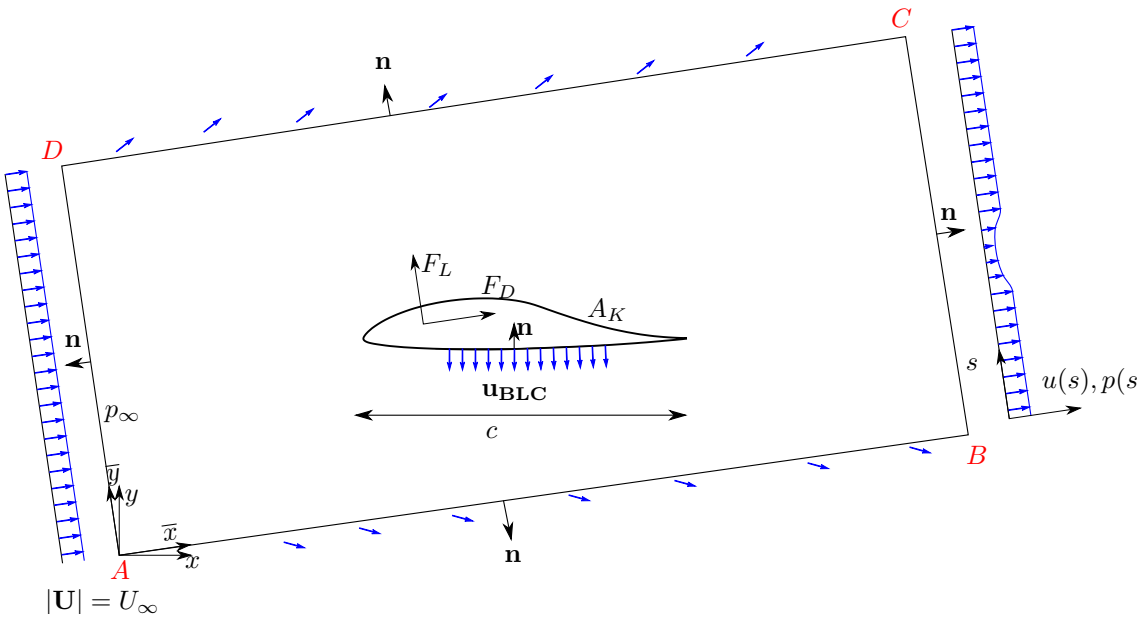


Figure 4.1: Control Volume (CV) for the airfoil momentum budget in which **n** is the normal vector pointing out of the CV ([FAF+23]).

A rotated coordinate system (x, y) is used to describe the airfoil orientation at varying angles of attack. Active flow control is introduced in the form of wall-normal micro blowing on the pressure side of the airfoil. The blowing velocity is denoted by u_{BLC}, with the index BLC meaning boundary layer control, and, for small angles of attack, is assumed to act in the $\overline{y}$-direction. In the uncontrolled case, no blowing is applied and thus $u_{BLC} = 0$.

The control volume is bounded by the outer surfaces $\overline{AB}$ and $\overline{CD}$, aligned with the $\overline{x}$-direction, and by $\overline{BC}$ and $\overline{DA}$, which are parallel to $\overline{y}$. Along the wake survey plane $\overline{BC}$, a sampling coordinate s is introduced to evaluate the velocity distribution $u(s)$ and the pressure distribution $p(s)$.

All other control surfaces are located sufficiently far away from the airfoil such that the streamwise velocity component $u_{\overline{x}}$ and the static pressure p can be assumed equal to their inflow values. The wetted surface of the airfoil is denoted by A_K, and the outward-pointing normal vectors are represented by $\vec{n}$.

4.1.1 Body Drag

For the uncontrolled configuration ($u_{BLC} = 0$), the integral momentum equation indicates that the force exerted by the fluid on the airfoil in the $\overline{x}$-direction can be evaluated from the momentum deficit in the far wake. This approach relies on the assumption that the static pressure has recovered to its upstream value, thereby eliminating any net pressure contribution to the momentum balance. Consequently, the streamwise force is directly related to the momentum loss in the wake.

The drag coefficient obtained from integrating the stresses acting directly on the airfoil surface (referred to as body drag) is defined as [FAF+23]

$$c_{D,body} = \frac{F_D}{\frac{1}{2}\rho_\infty U_\infty^2 A_K}, \tag{4.1}$$

where the reference area is $A_K = c \cdot l_s$, with l_s the span of the airfoil and c the chord length of the airfoil.

4.1.2 Wake Drag

Alternatively, the drag coefficient can be determined from measurements in the wake. The corresponding wake-based drag coefficient (referred to as wake survey drag) is [FAF+23]

$$c_{d,wake} = \frac{2}{\rho_\infty c} \int_B^C \rho(s) \frac{u(s)}{U_\infty} \left(1 - \frac{u(s)}{U_\infty}\right) \, \mathrm{d}s. \tag{4.2}$$

For an airfoil without blowing, both definitions coincide within experimental uncertainty

$$c_{d,body} = c_{d,wake} \text{ if } u_{BLC} = 0. \tag{4.3}$$

If the static pressure along the wake plane $\overline{BC}$ has not yet returned to its inflow value, the wake-based expression must be extended to include the pressure contribution [FAF+23]

$$c_{d,wake} = \frac{2}{\rho_\infty c} \int_B^C \left[\rho(s) \frac{u(s)}{U_\infty} \left(1 - \frac{u(s)}{U_\infty}\right) + \frac{1}{U_\infty^2} \left(p_\infty - p(s)\right)\right] \, \mathrm{d}s. \tag{4.4}$$

Although measuring $u(s)$ and $p(s)$ experimentally can be challenging, this formulation can be applied directly to numerical data.

If a drag-reducing control strategy is implemented without adding or removing mass within the control volume (for example, passive surface modifications), a reduction in $c_{d,body}$ is expected. Under the same assumptions as in the uncontrolled case, this reduction can be captured through the wake survey using the equations above.

4.1.3 Momentum balance with micro blowing

The situation changes when active micro-blowing is applied. In this case, additional mass is injected through the airfoil surface with velocity u_{BLC}, oriented normal to the mean flow direction. In the airfoil-fixed frame of reference, the injected fluid initially carries no streamwise momentum.

This type of blowing on the pressure side has been shown to reduce both skin-friction drag and pressure drag [18]. Consequently, the drag force F_D exerted by the fluid on the airfoil decreases, and therefore the body drag coefficient $c_{d,body}$ is reduced.

However, because mass is added inside the control volume, the wake momentum balance needs to be modified. The injected fluid must be accelerated to the freestream velocity U_∞ in the streamwise direction. This acceleration generates an additional momentum deficit in the wake equal to the product of the injected mass flow rate and freestream velocity.

By normalizing this contribution analogously to the drag coefficient definition, a dimensionless boundary layer control penalty term c_{BLC} is obtained [FAF+23]

$$c_{BLC} = 2\frac{u_{BLC}}{U_\infty}\frac{l_{BLC}}{c}\frac{\rho_{BLC}}{\rho_\infty}, \tag{4.5}$$

where l_{BLC} denotes the streamwise extent of the blowing region and ρ_{BLC} the density of the control fluid.

This resulting dimensionless momentum balance for the blowing-controlled configuration reads

$$c_{d,body} + c_{BLC} = c_{d,wake}. \tag{4.6}$$

The boundary layer control penalty therefore presents the difference between body drag and wake survey drag when blowing is applied. For sufficiently high blowing rates, this term can become significant. In fact, the equation shows that the body drag could even become negative if $c_{BLC} > c_{d,wake}$. Representative flow cases and a more detailed discussion of the modified momentum balance are provided in the original publication of Fahland et al. [FAF+23], to which the reader is referred for further details.

4.1.4 Consideration of mass source

In deriving the previous relation, the origin of the injected mass is not specified, it is simply assumed to be available at the airfoil surface. In numerical simulations, this is implemented via appropriate boundary conditions. In experiments, the fluid is typically supplied by an external pressurized reservoir.

A more realistic configuration would include an air intake that extracts the fluid required for the boundary layer control directly from the freestream. The intake redirects the captured air such that its streamwise momentum is transferred to the body. Even if viscous losses are neglected, the removal of streamwise momentum at the intake produces an additional drag contribution equal in magnitude, but opposite in sign, to c_{BLC}.

If the airfoil and intake are considered together as a closed system, mass conservation is satisfied internally, and the equality between body drag and wake survey drag is restored. However, if the airfoil with blowing is analyzed without accounting for an intake, the boundary layer control penalty term c_{BLC} must explicitly be included in the momentum balance.

4.2 Implementation of General Boundary Layer Conditions

4.2.1 No-Slip adiabatic wall

The surface of a simulated airfoil is modeled as a stationary, impermeable, and adiabatic wall. This boundary condition represents a solid surface that neither moves relative to the computational reference frame nor allows any mass transfer across the boundary. Accordingly, the velocity at the wall is prescribed as

$$\vec{u} = \vec{0}, \tag{4.7}$$

which enforces both the no-slip and no-penetration conditions. The no-slip condition requires the fluid velocity to match the velocity of the wall, whereas the no-penetration condition ensures that no fluid can pass through the solid boundary. The latter can also be expressed as

$$\vec{u} \cdot \hat{n} = 0, \tag{4.8}$$

where $\hat{n}$ denotes the outward unit normal vector at the surface.

Thermally, the wall is assumed to be adiabatic, implying that no heat is exchanged between the airfoil and the surrounding fluid. Consequently, the conductive heat flux normal to the wall vanishes. This condition is expressed by imposing a zero normal temperature gradient

$$\frac{\partial T}{\partial n} = 0. \tag{4.9}$$

In the finite-volume formulation, this is typically implemented by setting the temperature at the wall equal to the adjacent cell value, resulting in zero diffusive heat flux.

4.2.2 Far Field Boundary Condition

At the outer boundary, non-reflective boundary conditions are imposed to minimize artificial reflections. These boundary conditions are formulated based on the characteristic structure of the compressible Navier-Stokes equations.

In a compressible flow, information propagates along characteristic directions associated with wave speeds

$$u_n - a,\ u_n,\ u_n + a, \tag{4.10}$$

where u_n is the velocity component normal to the boundary and a is the local speed of sound.

Depending on the local Mach number and flow direction, some characteristics are oriented inward into the computational domain, and some point outward. For outgoing characteristics, the corresponding flow quantities are extrapolated from the interior solution. For incoming characteristics, freestream conditions are prescribed.

This procedure ensures that only physically consistent information enters the domain, while disturbances generated inside the domain can leave the computational domain without reflection. Consequently, the far-field boundary behaves transparently to outgoing acoustic and convective waves.

In practice, the freestream state is imposed along incoming characteristics, while the remaining variables are obtained from the interior solution via characteristic relations. This approach provides a stable and physically consistent representation of boundary conditions in compressible flow simulations.

5 Parametric study of blowing and suction for turbulent flow control on a transonic airfoil

This chapter is based on the publication *Investigation of blowing and suction for turbulent flow control on a transonic airfoil* by Frede and Gatti [FG25] and presents the methodology and the resulting analysis of the investigated flow control techniques. The study focuses on the application of RANS simulations to assess the aerodynamic impact of wall-normal blowing and suction on the transonic airfoil RAE2822. A comprehensive parametric study is conducted, systematically varying flow conditions and control parameters, including Mach number, angle of attack, control magnitude, and control location. The results presented in this chapter provide a detailed evaluation of the aerodynamic behavior of different control configurations. The analysis focuses on the effects on lift and drag as well as shock behavior in the subsonic and transonic regimes. Particular attention is given to the question of how wall-normal blowing and suction perform under compressible and transonic flow conditions and how shock-boundary-layer interactions influence the effectiveness of the control strategy in improving aerodynamic efficiency. The overall efficiency serves as an indicator of whether the applied control strategy has a beneficial or negative effect on the flow behavior.

5.1 Methodology

5.1.1 Numerical methods

"The compressible flow around the transonic airfoil RAE2822 is simulated via Reynolds-Averaged Navier-Stokes equations (RANS) with the open-source solver SU2 [16]. For the simulations, the density-based steady-state solver is used. The Menter k-ω-SST model is employed as the turbulence model. A fixed transition at $x/c = 0.1$, with c being the chord length and x the coordinate in the streamwise direction, is implemented via a semi-implicit scalar source. The tripping location spans 1%c in the streamwise direction, and the size of the local boundary layer thickness in the wall-normal direction. The fluid is modeled as standard air and treated as an ideal gas with the viscosity calculated by the Sutherland model.

The numerical grid consists of hexahedral cells and has a 2D block-shaped pattern. It has a C-radius of $r_c = 50c$ and an outlet distance of $d_o = 75c$, where c is the chord length of the airfoil. A sketch of the mesh is shown in Figure 5.1. The total cell count of the meshes is $n_{cell} \approx 150000$. A y^+ value of 1 or less is assured in the first cell of the boundary layer. The boundary layer consists of at least 40 points. The growth factor near the wall is 1.1, so a detailed resolution of the flow near the wall is provided. The meshes are generated with a custom script using *blockMesh* from OpenFoam and are then converted into a readable format for SU2. For a detailed description of the mesh generation, see Fahland et al. [18].

The convective fluxes are discretized with the second-order *Roe* method [64] and the viscous fluxes with the *Green-Gauss* method [19]. For the gradients of turbulent variables, the second-order upwind scheme is applied." [FG25]

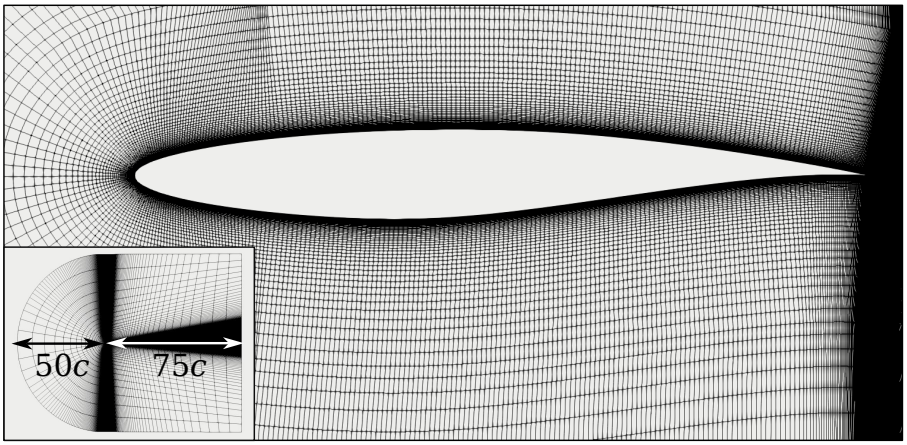


Figure 5.1: Sketch of the computational C-mesh.

5.1.2 Boundary Conditions

"The airfoil's surface is simulated as an adiabatic wall. In the non-control regions, the velocity in the normal direction on the airfoil surface is set to zero, so a no-slip boundary condition is present. " [FG25]

Within the control region, boundary layer control via blowing and suction is applied through a prescribed wall-normal mass flux. Instead of enforcing a no-slip condition, a wall-normal velocity u_{BLC} is imposed. The corresponding mass flux is given by

$$\dot{m}_{BLC} = \rho_{BLC} u_{BLC} l_{BLC}. \tag{5.1}$$

The thermodynamic state of the boundary is not fully prescribed but reconstructed using a characteristic-based approach. For subsonic inflow, one characteristic propagates from the domain interior toward the boundary. Therefore, one piece of information must be obtained from the interior solution. This is achieved by extrapolating the outgoing Riemann invariant [4]

$$\mathcal{R} = \frac{2}{\gamma - 1} a + \vec{u} \cdot \hat{n}. \tag{5.2}$$

Riemann invariants represent quantities that remain constant along characteristics and enable a physically consistent coupling between prescribed boundary data and interior flow information in compressible flow.

Using the prescribed wall-normal velocity and the extrapolated Riemann invariant, the boundary speed of sound is calculated as

$$a_{BLC} = \sqrt{\frac{\gamma - 1}{2} (\mathcal{R} - \vec{u}_{BLC} \cdot \hat{n})}. \tag{5.3}$$

The density at the boundary is approximated by the density of the nearest interior cell

$$\rho_{BLC} = \rho_{int}, \tag{5.4}$$

which corresponds to a first-order extrapolation from the flow field.

The static pressure at the boundary is then obtained from the equation of state

$$p_{BLC} = \frac{\rho_{BLC}\, a_{BLC}^2}{\gamma}. \tag{5.5}$$

Finally, the total energy is reconstructed as

$$E_{BLC} = \frac{p_{BLC}}{\rho_{BLC}(\gamma - 1)} + \frac{1}{2}\vec{u}_{BLC}^2, \tag{5.6}$$

with an additional turbulent kinetic energy contribution if a turbulence model is employed.

This formulation ensures that the boundary condition is consistent with the hyperbolic nature of the compressible Navier-Stokes equations, allowing only physically consistent information to enter the domain.

"The outer boundaries of the computational domain use a non-reflective far-field boundary condition aligned with the local directions of the characteristics.

In most of the simulations performed in the present study, the region in which blowing and suction are applied spans from $x/c = 0.25$ to 0.85. The late start of the control region allows the flow to become fully turbulent before the control region starts. The endpoint of $x/c = 0.85$ was chosen so that trailing edge components can still be implemented without overlapping with the control region. In Section 5.3.4, the influence of the position of the control area was also analyzed. Unless otherwise stated, the following results always refer to the control area described above.

In the parametric study, three different control configurations were investigated: blowing on the pressure side, suction on the suction side, and blowing on the suction side. All three configurations are investigated individually, and no combinations of two configurations are considered." [FG25]

5.1.3 Net drag

"The drag coefficient for an airfoil can be calculated by integrating the pressure and friction stresses along the surface, which results in the body drag $c_{D,body}$, or it can be determined from the momentum loss in the wake, which results in the wake drag $c_{D,wake}$. For an uncontrolled case or a controlled case with zero total mass flow, which means that the mass flow of the fluid sucked in is the same as the mass flow of the blowing fluid, the two drag components are equal. The active flow control of blowing and suction, where fluid is either removed or expelled, changes this relationship. In the case of blowing, a mass source is present on the airfoil surface, since the air intake is not explicitly defined in the current investigated system. The fluid that is expelled in the wall-normal direction lacks momentum in the main wind direction, so it needs to be accelerated towards the wake of the airfoil. The reaction force is carried by the body, which results in a reduced body drag compared to the wake drag.

For suction, the opposite occurs, and thus the wake drag is reduced compared to the body drag, as shown by Beck et al. [9]. For both suction and blowing, the largest among $c_{D,body}$ and $c_{D,wake}$ is the drag component, which includes the costs of providing or expelling the flow control fluid. This is the so-called inclusive drag $c_{D,inc}$, which is used in the analysis of the results for a comparison of the different investigated cases.

$$c_{D,inc} = \begin{cases} c_{D,body} = c_{D,wake} + c_{BLC} & \text{for suction} \\ c_{D,wake} = c_{D,body} + c_{BLC} & \text{for blowing} \end{cases} \tag{5.7}$$

Here, the boundary layer control penalty c_{BLC} is proportional to the mass flow rate [FAF+23]

$$c_{BLC} = \left| 2 \frac{u_{BLC}}{U_\infty} \frac{l_{BLC}}{c} \frac{\varrho_{BLC}}{\varrho_\infty} \right|, \tag{5.8}$$

with the velocity of the control fluid u_{BLC} and the freestream velocity U_∞. The length of the control system is described by l_{BLC}, while the control fluid has a density of ϱ_{BLC} and the free stream of ϱ_∞." [FG25]

The derivation of the boundary layer control was shown in Section 4.1.

5.1.4 Power Budget

"Additionally to the control penalty drag c_{BLC} due to the non-zero mass flow rate, the power required to operate the active control must be taken into account to assess the net efficiency increase. The focus of the current study is the investigation of the influence of different control configurations. Therefore, no combinations of blowing and suction are studied, and the net control mass flow rate is always non-zero. The details of the air supply (for blowing) or dumping (for suction) strongly influence the required control power but are not explicitly defined here, since they greatly depend on the particular physical implementation of the active control, which is not addressed in the present study. Therefore, an accurate calculation of the additional power is not possible, and many simplifying assumptions have to be made here. In this respect, we follow the approach of Fahland et al. [18] for the estimation of the additional power. Although this estimate reflects a worst-case scenario, it can be calculated and understood with just a few assumptions and limited complexity.

The additional control power is defined as the power needed to overcome the pressure difference between the fluid supply and the controlled surface for blowing, or from the controlled surface to the position of discharge for suction.

The power consumption is converted to dimensionless drag components so that the efficiency can be calculated with the extra cost [9]. It is assumed that the fluid from suction is expelled at a pressure coefficient of $c_p = 1$ and the fluid for the blowing control is collected at stagnation, where also $c_p = 1$ is valid. So the total drag coefficient results in

$$c_{D,total} = \begin{cases} c_{D,body} - c_{BLC} + c_{pump} & \text{for suction} \\ c_{D,body} + c_{BLC} + c_{turbine} & \text{for blowing} \end{cases} \tag{5.9}$$

where c_{pump} accounts for the energy that is needed to drive the pump for suction and $c_{turbine}$ reflects the energy that can be regained by a turbine during the blowing process.

For the suction control, extra energy is needed for the actual suction process, which is expressed by c_{pump}. The sucked fluid can now be expelled somewhere on the airfoil surface to generate some thrust. We assume to expel the fluid at $c_p = 1$, since at this specific pressure coefficient the thrust equals the boundary layer penalty c_{BLC}. For the blowing process, the costs for the fluid supply can be calculated by the boundary layer control penalty, while some energy can be regained from the turbine.

To calculate the pump drag for suction or the turbine drag for blowing, the pressure differences between the supply chamber and the sink or source, respectively, need to be determined. The sink and the source are at the freestream total pressure level.

The pressure of the supply chambers is at a constant pressure level, which is calculated by the following equation

$$c_{p,chamber} = \begin{cases} min\{c_{p,control}\} - 0.1 & \text{for suction} \\ max\{c_{p,control}\} + 0.1 & \text{for blowing} \end{cases} \tag{5.10}$$

where $c_{p,control}$ is the pressure coefficient in the control area, and the maximum or minimal value is used for blowing or suction, respectively. For suction, the pressure level in the supply chamber needs to be lower compared to the pressure level on the control surface, therefore, $\Delta c_p = 0.1$ was subtracted from the minimal pressure value [9]. The opposite holds for blowing, the pressure level in the supply chamber needs to be higher than on the control surface, so $\Delta c_p = 0.1$ was added to the maximum pressure value. The different pressure levels are also shown in Figure 5.2.

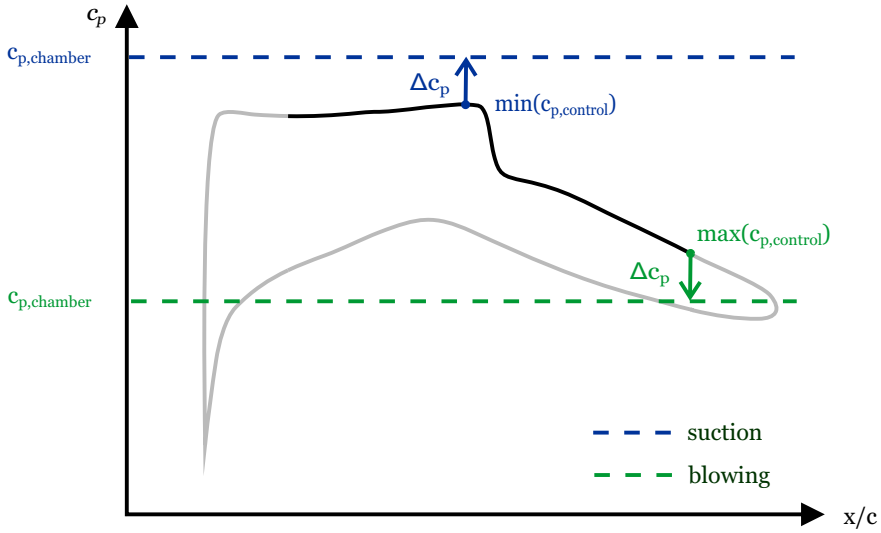


Figure 5.2: Sketch of a pressure distribution to determine the different pressure levels for the supply chambers for the pump or turbine.

This choice does not reflect the best option but gives an estimation of the costs for the control. Especially for configurations with large pressure differences in the control area, as they are present in the cases where a shock wave appears on the suction side, this estimation is a very conservative approximation. For a more detailed discussion of the applied power calculation, see Section 5.4.

The pump and turbine drag are calculated as follows

$$c_{pump} = \frac{1}{\eta_p} \frac{u_{BLC}}{U_\infty} \frac{l_{BLC}}{c} \frac{\varrho_{BLC}}{\varrho_\infty} (1 - c_{p,chamber}), \tag{5.11}$$

$$c_{turbine} = -\eta_t \frac{u_{BLC}}{U_\infty} \frac{l_{BLC}}{c} \frac{\varrho_{BLC}}{\varrho_\infty} (1 - c_{p,chamber}), \tag{5.12}$$

with a pump efficiency of $\eta_p = 0.7$ and a turbine efficiency of $\eta_t = 0.7$ [9]." [FG25]

5.1.5 Parametric Study

"A parametric study was conducted to investigate the effect of wall-normal blowing and suction on the transonic airfoil RAE2822 in a compressible and subsonic or transonic flow. All simulations were conducted at a chord-based Reynolds number of about $Re = 5 \times 10^6$. The Mach number was varied between $Ma = 0.6$, which corresponds to the subsonic flow case, up to $Ma = 0.729$, the design Mach number for the present airfoil, representing the fully transonic case. The control magnitude is expressed in terms of mass flow rate and ranges between $\dot{m}_{BLC} = 0.1\%\dot{m}_\infty$ up to $3\%\dot{m}_\infty$ with the freestream mass flow per unit area of $\dot{m}_\infty = U_\infty c\varrho_\infty$. The angle of attack varies between $\alpha = -1°$ and $\alpha = 3°$.

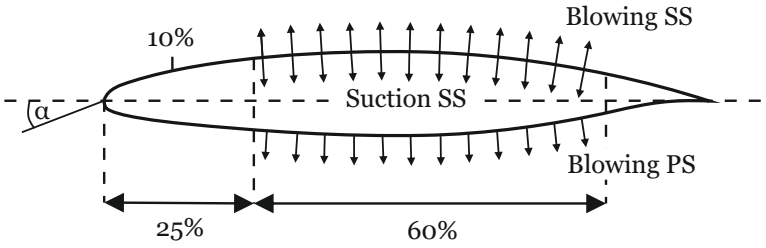


Figure 5.3: Sketch of the control areas and different control configurations.

Three different control configurations are investigated: blowing on the suction side, suction on the suction side, and blowing on the pressure side. In Figure 5.3, a sketch of the airfoil and the different control configurations is shown. In the results, the influence of varying the position at which blowing or suction is applied is analyzed. To this aim, three additional control positions are introduced, named before shock, across shock, and behind shock. These control areas have a size of $10\%c$ and their positions are defined with respect to the shock position in the uncontrolled cases. A graphical sketch of the positions is shown in Figure 5.4. For all other configurations, the default control area of $x/c = 0.25 - 0.85$ is used.

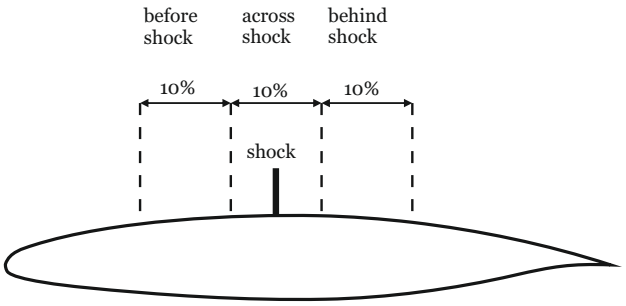


Figure 5.4: Sketch of the different control positions with respect to the shock position.

For all combinations of Ma and α, the uncontrolled reference cases are calculated. These results were used as restart files for the controlled cases to save computational time.

The freestream parameters are based on a flight altitude of 11km at standard atmosphere. For the simulations, a Reynolds number of $Re = 5 \times 10^6$, a free stream temperature of $T_\infty = -53.5°\mathrm{C}$, a viscosity of $\mu_\infty = 1.449 \times 10^{-5} \frac{\mathrm{kg}}{\mathrm{ms}}$ and the corresponding Mach number are prescribed. The density and the pressure are calculated from the given parameters and the ideal gas law.

The Mach number varies between $Ma = 0.6 - 0.729$, so the range of subsonic up to transonic flow regimes is covered. The Reynolds number of the simulation is smaller compared to a real

airplane with a Reynolds number of about $Re = 20 \times 10^6 - 30 \times 10^6$, depending on the size of the airplane. This regime cannot be covered in this study, because the computational costs for such high Reynolds numbers are too high. So all calculations have been conducted at lower Reynolds numbers of $Re = 5 \times 10^6$." [FG25]

5.2 Validation of RANS code

"For the validation of the present RANS results, a direct numerical simulation is performed with the code FLEW, developed by Soldati et al. [70]. FLEW is designed for performing DNS on structured grids defined on generalized curvilinear coordinates and is an extension of the Cartesian code STREAmS [51]. The numerical framework uses a hybrid discretization of the compressible Navier-Stokes equations, which combines the nearly-zero numerical dissipation of 8^{th}-order central schemes, best suited to accurately describe turbulence structures, with the robustness of 7^{th}-order Weighted Essentially Non-Oscillatory (WENO) schemes, required to capture shock waves.

The grid was generated with a modified version of the open-source software Construct2D [56], where a hyperbolic algorithm generates high-quality, smooth C-type meshes. The grid generated with the code for a Reynolds number of $Re = 3 \times 10^5$ consists of 4096x512x256 nodes in streamwise (x), wall-normal (y), and spanwise (z) directions, respectively.

The C-mesh has a radius of $25c$, and the outflow of the domain is placed at $25c$ from the trailing edge of the airfoil with the chord length c. The flow is assumed to be periodic in the spanwise direction with an extension of $0.1c$. Additionally to the freestream condition prescribed, non-reflective boundary conditions are imposed to prevent the shock wave from being reflected in the far field. On the airfoil, a no-slip adiabatic boundary condition is prescribed.

The validation of the RANS simulation is performed at a Reynolds number of $Re = 3 \times 10^5$, a Mach number of $Ma = 0.725$, and an angle of attack of $\alpha = 4°$. The distribution of the pressure and friction coefficient is shown in Figure 5.5. The forced transition of the flow at $x/c = 0.1$ was prescribed for the DNS simulation with a numerical tripping defined according to Schlatter and Örlü [68], consisting of a weak random volume force acting in the wall-normal direction. Owing to the small value of the Reynolds number and the effect of the favorable pressure gradient present up to $x/c \approx 0.4$, it was observed that the boundary layer on the pressure side of the airfoil remains laminar despite the numerical tripping. At $x/c \approx 0.4$ the pressure gradient changes and is now positive, which leads to a separation of the flow on the lower surface with a consequent separation-induced transition and reattachment.

The semi-implicit scalar source employed to initiate the turbulent flow in the RANS simulations at large values of Re is not adequate to reproduce the complex scenario occurring at the low value of Re necessarily employed in the DNS. To capture the transition and separation correctly, also in the RANS simulations, the Langtry-Menter transition model has been utilized. The model predicts the transition and flow separation at the lower surface as expected and thus agrees with the DNS simulations. The LM transitional model was modified for the upper surface to trigger the transition at $x/c = 0.1$ on the upper surface.

The pressure distribution shows good agreement between the DNS and the RANS simulations, see Figure 5.5. Both simulations capture the shock at the same position. Only the flow separation takes place slightly later on the airfoil's lower surface for the RANS simulation. This can also be

observed in the distribution of the friction coefficient. Additionally, it can be seen that turbulence in the DNS simulation is triggered at $x/c = 0.1$.

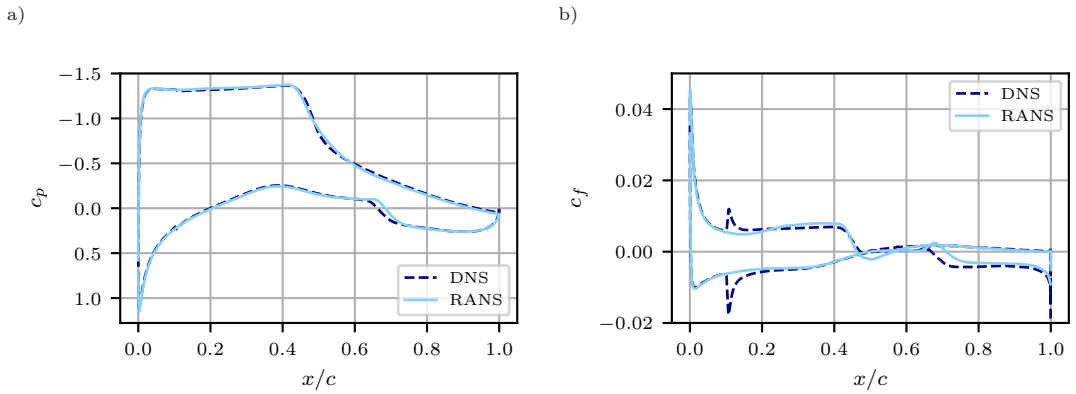


Figure 5.5: Distribution of the pressure and friction coefficient for a RANS and a DNS simulation at a Reynolds number of $Re = 3 \times 10^5$.

In Table 5.1, the aerodynamic coefficients for the validation simulations are shown. The lift coefficient agrees perfectly, while a small difference can be observed for the drag coefficient, which mainly comes from a difference in the friction drag. A small underestimation of the drag coefficient was also observed in the comparison of RANS and DNS by Fahland et al. [18] for an incompressible flow. Despite the small deviation in the absolute value of the drag, the relative changes induced by the control were correctly reproduced in the RANS simulations.

Table 5.1: Aerodynamic coefficients for the conducted validation simulation for the RANS and DNS results for a Reynolds number of $Re = 3 \times 10^5$.

	$\mathbf{c_l}$	$\mathbf{c_{d,body} \cdot 10^2}$	$\mathbf{c_{d,p} \cdot 10^2}$	$\mathbf{c_{d,f} \cdot 10^2}$
DNS	0.840	3.261	2.461	0.800
SU2	0.839	3.165	2.472	0.694

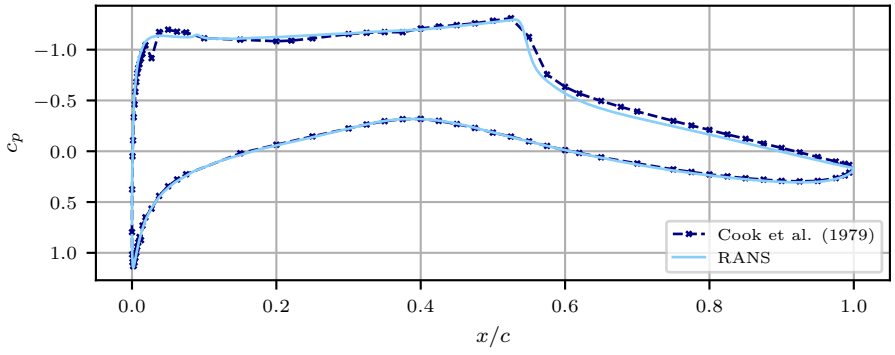


Figure 5.6: Pressure distribution of the RANS simulation and the experimental data of Cook et al. [14] at a Reynolds number of $Re = 6.5 \times 10^6$.

While it is not possible to exploit DNS for validating the RANS simulations at the larger value of the Reynolds number of $Re = 5 \times 10^6$ employed in the present study, we can resort to laboratory experiments. So the pressure distribution of the RANS simulation at a Reynolds number of $Re = 6.2 \times 10^6$, a Mach number of $Ma = 0.734$, and an angle of attack of $\alpha = 2.79°$ (corrected for

experimental wind tunnel blockage) is compared to the experimental data of Cook et al. [14] (test case 9).

Figure 5.6 shows the pressure distribution of the RANS simulation and the experimental data of Cook et al. [14]. The data show great agreement, where only the shock position is slightly shifted toward the trailing edge for the experimental data.

Finally, the validation of the RANS simulation with the DNS simulation at a Reynolds number of $Re = 3{\times}10^5$ and the comparison with the experimental data at a Reynolds number of $Re = 6.5{\times}10^6$ showed that the RANS simulations can resolve the flow and the most relevant flow physics." [FG25]

5.3 Effects of Parameter Variations

5.3.1 Effect of Control Configuration

"In the parametric study, three different control configurations were investigated: blowing on the pressure side, blowing on the suction side, and suction on the suction side. The effect of the different control configurations should be discussed in this Section. In Figure 5.7, the polar plots and the pressure and friction coefficient distributions are plotted for a Mach number of $Ma = 0.6$ in the left column (subsonic uncontrolled case) and $Ma = 0.725$ in the right column (transonic uncontrolled case). The control magnitude is $\dot{m}_{BLC} = 0.1\%\dot{m}_\infty$ and the angle of attack is $\alpha = 2.31°$ for the c_p and c_f plots. The angle of attack of $\alpha = 2.31°$ is marked by the circled symbols in the polar plot. To increase the readability of the data and prevent them from overlapping, the c_f values from the lower surface of the airfoil are plotted as negative values.

First, the subsonic cases at a Mach number of 0.6, which are shown in the left column of Figure 5.7, are analyzed. All polars show a similar trend in which the lift and drag coefficients increase with increasing angle of attack. Since no complete flow separation is observed, no sudden changes in the slope are expected. The slope of the polars for suction on the suction side and blowing on the pressure side increased compared to the uncontrolled case, while the slope for blowing on the suction side decreased. All controlled polars are shifted to higher drag values compared to the uncontrolled case, except for the high-lift configurations of suction on the suction side. Especially for the two blowing configurations, the inclusive drag coefficient increased by around 20%. For suction on the suction side, the drag difference at the lower lift configuration is significant but decreases with increasing angle of attack and lift. At $\alpha = 2.31°$, the two polars intersect, and the drag coefficient of the case with suction on the suction side has a lower drag coefficient than the uncontrolled case. For these high-lift configurations, an increase in efficiency is reached. The distribution of the pressure coefficient changes slightly depending on the control configuration, see Figure 5.7 c). Blowing on the suction side leads to a slightly increased pressure coefficient on the whole upper side. Opposite effects can be observed for suction on the suction side with a slightly decreased pressure coefficient. The slightly decreased pressure coefficient results in a small increase in lift coefficient compared to the uncontrolled case for a constant angle of attack. Blowing on the pressure side leads to a decrease in the pressure coefficient on the lower side. A clear effect of the control can be observed for the friction coefficient (see Figure 5.7 e)). In the control region, a clear increase can be seen for suction, whereas a decrease can be observed for blowing. Suction removes fluid from the boundary layer, and thus the boundary layer thickness is thinner. The velocity gradient in the boundary layer increases, which then results in an increase in the wall-shear stress and thus an increased friction coefficient. For blowing, the opposite effects can be observed.

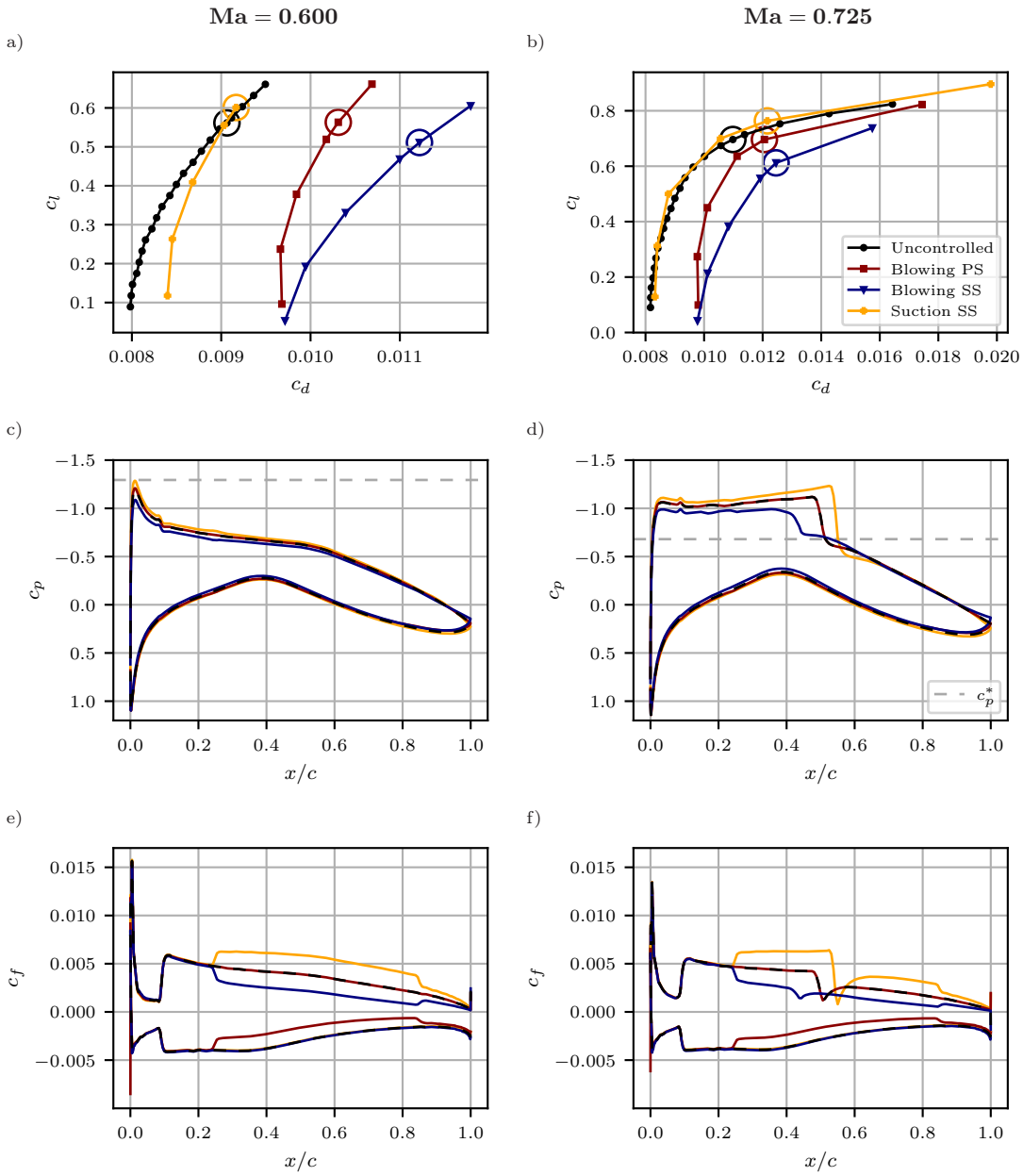


Figure 5.7: Polar plot and pressure and friction coefficient distribution for the three control configurations and the uncontrolled reference case for $\dot{m}_{BLC} = 0.1\%\dot{m}_\infty$ and $\alpha = 2.31°$ for the surface distribution plots, and $Ma = 0.6$ and 0.725 for the left and right columns, respectively.

Secondly, the transonic case at a Mach number of $Ma = 0.725$, which is shown in Figure 5.7 in the right column, is studied. The trend of the polars is similar to the subsonic cases, an increase in the angle of attack leads to an increased drag and lift coefficient. For suction on the suction side, most configurations show a decreased drag coefficient compared to the uncontrolled case, which results in an increased efficiency. The other two configurations, blowing on the pressure and suction side, lead to an increased drag. The pressure distributions show a clear dependency on the different control configurations. For blowing on the pressure side, the pressure distribution on the upper side matches the one of the uncontrolled case, whereas a small decrease of c_p on the lower side can be observed. Both control configurations on the upper side have a significant influence on the shock position and magnitude. For the uncontrolled case, covered by the red curve, the shock position is at $x/c = 0.51$. Blowing on the suction side leads to a shift of the shock towards the leading edge

to $x/c = 0.44$ and a decrease in the shock magnitude, whereas opposite effects can be observed for suction on the suction side: the shock is shifted towards the trailing edge to $x/c = 0.55$, and the shock magnitude increases significantly. Before the shock, a near-constant pressure coefficient can be observed, followed by a significant increase in c_p at the shock position and a steady increase towards the trailing edge. The sonic c_p^* value is also indicated in the pressure distribution for the corresponding Mach number.

Similar to the subsonic case, an increase (or decrease) of the friction coefficient in the control region can be observed for suction (or blowing). The shock is indicated by a sharp drop of c_f followed by a slight recovery.

In agreement with previous literature [13, 33, 45, 48, 74], blowing leads to a reduction of the friction drag of up to 40% for the transonic cases with a medium mass flow rate. However, when the inclusive drag is calculated, which also includes the pressure drag component and the boundary layer control penalty, an increase in the inclusive drag is observed compared to the uncontrolled cases.

Overall, it can be concluded that the only control configuration that can lead to an increase in efficiency is suction on the suction side for rather high lift configurations, if taking into account the inclusive drag." [FG25]

5.3.2 Effect of Control Magnitude

"The effect of the control magnitude is discussed in this Section. The left column of Figure 5.8 shows the subsonic uncontrolled case at $Ma = 0.65$ and the corresponding controlled cases with suction on the suction side at an angle of attack of 2.31°, marked by circled symbols in the polar plot. The polar plot clearly shows a shift of the c_l-c_d curves to higher drag values with increasing control magnitude. The lift coefficient at the same angle of attack also increases with increasing control magnitude. Nevertheless, the aerodynamic efficiency is smaller than that for the uncontrolled cases. For high lift configurations and a rather small control magnitude of $\dot{m}_{BLC} < 0.2\%\dot{m}_\infty$, slightly lower drag values compared to the uncontrolled polar (black) can be observed. From the polar plot, it can be summarized that, especially, the cases with a small control magnitude are promising for an efficiency increase.

In the pressure distribution, it can be observed that the uncontrolled case, indicated in black, is subsonic and no shock is present on the upper side of the airfoil. With increasing magnitude of the suction on the upper side, a pressure decrease followed by a sudden pressure increase around $x/c = 0.22 - 0.28$, dependent on the control magnitude, can be observed, which leads to the appearance of a shock for high control magnitude configurations ($\dot{m}_{BLC} \geq 1\%\dot{m}_\infty$). Suction on the upper side also influences the flow on the lower side, which can be observed by a slightly increased pressure coefficient. This effect increases with increasing control magnitude. The increase in the pressure coefficient on the lower side and the presence of the shock for higher control magnitudes explain the lift increase observed in the polar plot for higher control magnitudes.

Suction on the suction side leads to an increase in the friction coefficient on the upper surface, as expected. The increase in the friction coefficient grows with increasing control magnitude. The presence of the shock can also be observed in the friction coefficient and is indicated by a strong decrease in c_f.

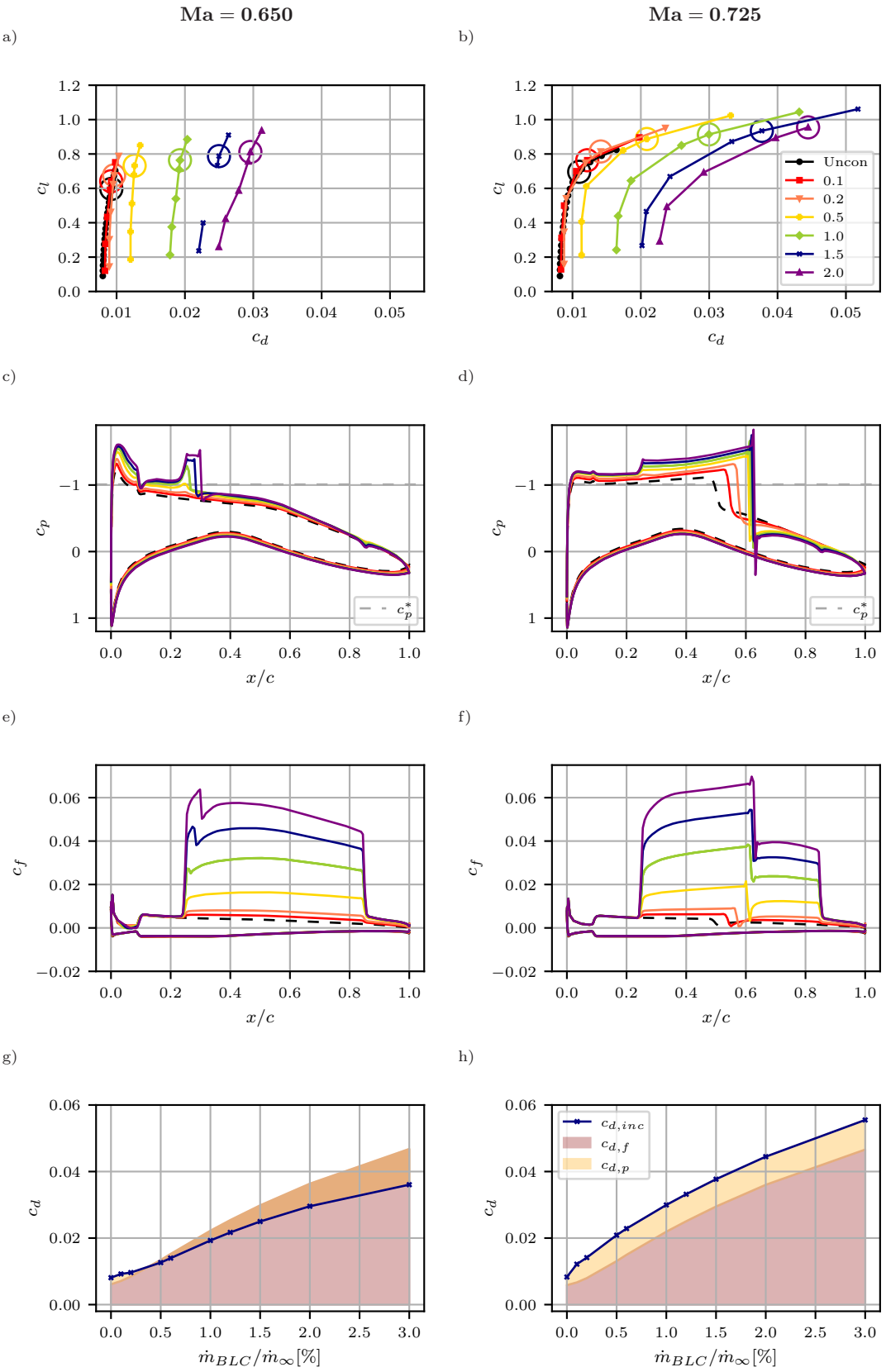


Figure 5.8: Polar plot and pressure and friction coefficient distribution for different control magnitudes and the uncontrolled reference case. The applied control is suction on the suction side at Mach numbers of $Ma = 0.65$ and 0.725 for the left and right columns, respectively. The surface plots are shown for an angle of attack of $\alpha = 2.31°$.

The inclusive drag is the sum of the pressure and friction drag, as well as the boundary layer control penalty. The last plot in the left column shows the pressure and friction drag ratios compared to the total drag. Since the body drag for the control of suction already includes the boundary layer penalty, it is not plotted in Figure 5.8 g). The blue curve indicates the inclusive drag, which consists of a friction part, shown in red, and a pressure part, shown in yellow. For a control magnitude of $\dot{m}_{BLC} \geq 0.5\%\dot{m}_{\infty}$, the blue curve cuts the ratio of the friction component. This indicates that a negative pressure drag is present, and thus the inclusive drag is lower than the friction component. This is shown by the orange color, which is an overlap of the red and the yellow area.

In the transonic case for a Mach number of $Ma = 0.725$, right column of Figure 5.8, it can be seen that the low magnitude control configurations ($\dot{m}_{BLC} \leq 0.2\%\dot{m}_{\infty}$) at high lift coefficients lead to slightly lower drag values compared to the uncontrolled case. The overall trend of the polars is similar to the one of the subsonic case, with increasing mass flow rate of the control fluid, the polars are shifted to higher drag values and also to higher lift values.

The increase in the lift coefficient can be explained by the shift of the shock position towards the trailing edge for increasing control magnitude, see Figure 5.8 d), and the increase in the shock magnitude. In the friction coefficient distribution in Figure 5.8 f), an increase in the friction coefficient with increasing control magnitude can be observed. The increase in the friction coefficient can also be seen in Figure 5.8 h), where the friction ratio is marked by the red area, which increases with increasing control magnitude. The ratio of the pressure component is almost constant, marked by the yellow area, and is now positive, compared to the subsonic case, which leads to higher inclusive drag values.

The effect of the control magnitude for blowing on the pressure side is shown in Figure 5.9. In the uncontrolled subsonic case (black) with a Mach number of 0.65, left column, an increase in the drag coefficient with increasing angle of attack can be observed, while a significant increase in the lift coefficient can be observed. For the low magnitude controlled cases, the trend is the same, but the polar is shifted to slightly higher drag values. For higher control magnitudes, $\dot{m}_{BLC} \geq 0.5\%\dot{m}_{\infty}$, the trend changes and the drag coefficient decreases with increasing angle of attack, accompanied by an increase in the lift coefficient. For control magnitudes $\dot{m}_{BLC} \geq 0.5\%\dot{m}_{\infty}$, massive separation occurs on the lower side due to the injected fluid. Flow snapshots with local streamlines are shown in Figure 5.10, where the flow separation in the back part of the airfoil can be seen.

The pressure coefficient for $\alpha = 2.31°$ for the uncontrolled case, compare Figure 5.9 c) (dashed black curve), increases over the whole upper side. On the pressure side, the pressure coefficient decreases up to $x/c = 0.4$ and then changes its slope and increases continuously towards the trailing edge. For low control magnitudes, the trend of the pressure distribution only changes slightly, with a small decrease in the pressure coefficient on the upper side. On the lower side, the pressure coefficient increases in the region up to $x/c \leq 0.58$ and decreases in the back part of the airfoil compared to the uncontrolled case. At higher control magnitudes $\dot{m}_{BLC} \geq 1\%\dot{m}_{\infty}$, blowing on the pressure side leads to a shock on the suction side close to the leading edge, which is associated with a strong increase in the pressure coefficient. On the pressure side, it can be observed that the pressure coefficient is almost constant and close to zero in the region of $x/c \approx 0.4$ towards the trailing edge, which indicates separation. As already seen in Figure 5.10, the flow detaches when the control magnitude is larger than $0.5\%\dot{m}_{\infty}$, which can be seen by the smaller pressure gradient and the zero friction coefficient. In the area where the flow is detached, the injected fluid is still present and gets deflected towards the outer flow. The friction coefficient behaves as expected: it decreases more and more in the region of blowing with increasing control magnitude up to a control magnitude of $\dot{m}_{BLC} \leq 0.5\%\dot{m}_{\infty}$.

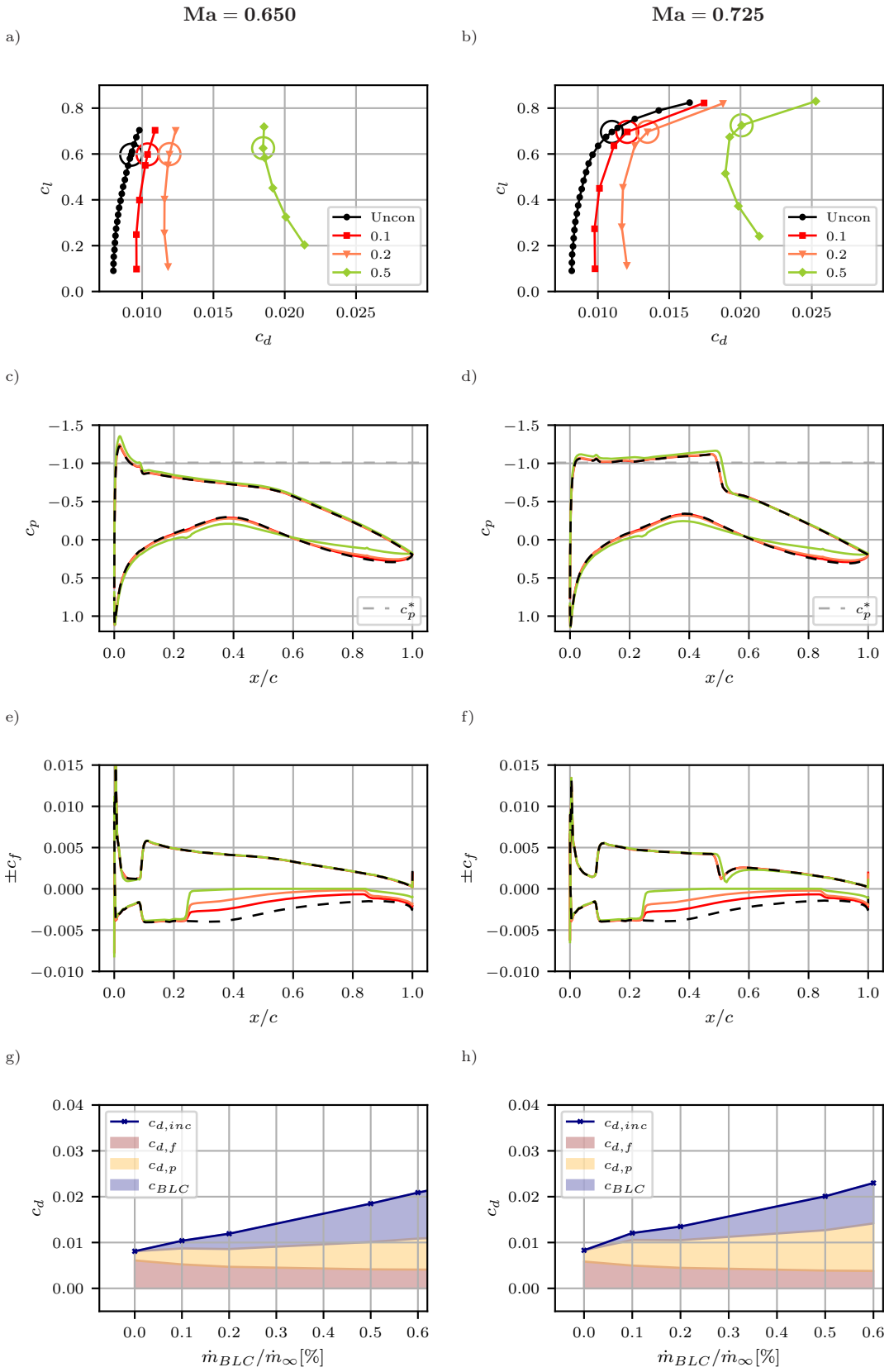


Figure 5.9: Polar plot and pressure and friction coefficient distribution for different control magnitudes and the uncontrolled reference case. The applied control is blowing on the pressure side at Mach numbers of $Ma = 0.65$ and 0.725 for the left and right columns, respectively. The surface plots are shown for an angle of attack of $\alpha = 2.31°$.

For higher control magnitudes, the friction coefficient in the control region is zero, and the flow is detached. Due to the flow of the control fluid in the wall-normal direction, no friction is present in this area, as well as no backflow. When the blowing region ends at $x/c = 0.85$, a full separation with backflow, which can be denoted by a negative friction coefficient, can be observed for high control magnitudes of $\dot{m}_{BLC} \geq 1\%\dot{m}_{\infty}$.

With increasing control magnitude, the friction drag is slightly decreasing, while the pressure drag increases, see Figure 5.9 g). The main contribution to the drag is the boundary layer penalty drag, which increases significantly with increasing control magnitude and is responsible for about 57% of the total drag for a control magnitude of $\dot{m}_{BLC} = 1\%\dot{m}_{\infty}$.

The Figures for the transonic case are shown in the right column of Figure 5.9. In the polar plot, only the data up to a control magnitude of $\dot{m}_{BLC} \leq 0.6\%\dot{m}_{\infty}$ are presented since no steady solution can be obtained for higher control magnitudes. The polars are shifted to higher drag values but also higher lift coefficients with increasing control magnitude. In the pressure distribution (see Figure 5.9 d)) a slight decrease of the pressure coefficient before the shock position for small control magnitudes can be observed, while the shock position is shifted towards the trailing edge. On the pressure side, the same effect as in the subsonic case can be seen, the pressure coefficient in the control area is almost constant. The shift in the shock position and magnitude increases with increasing control magnitude, even though the control takes place at the opposite side of the airfoil.

On the pressure side, the friction coefficient in the control area is again zero, as also seen in the subsonic case." [FG25]

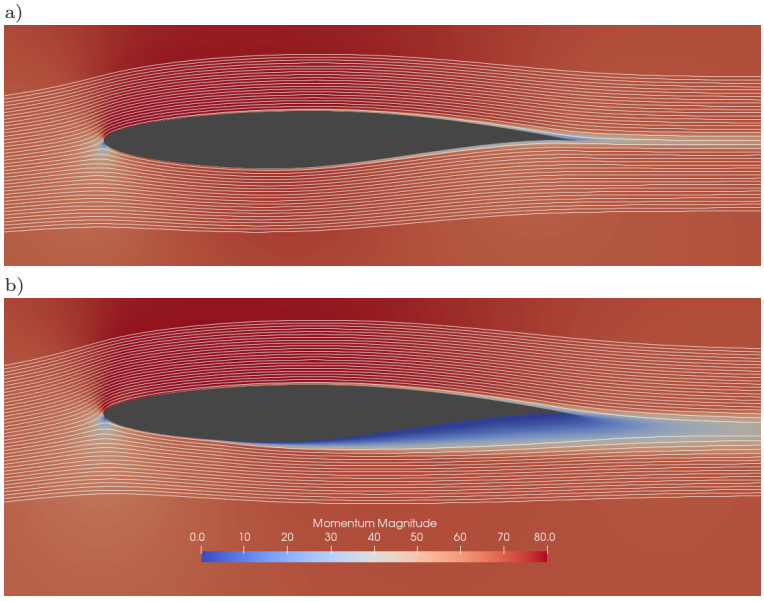


Figure 5.10: Snapshot of the streamlines for (a) the uncontrolled case and (b) the controlled case with blowing on the pressure side for $Ma = 0.65$, $\alpha = 2.31°$ and $\dot{m}_{BLC} = 1.2\%\dot{m}_{\infty}$.

5.3.3 Effect of Mach number

"In Figure 5.11, the results for a variation of the Mach number are shown for the control of suction on the suction side with a control magnitude of $\dot{m}_{BLC} = 0.2\%\dot{m}_{\infty}$. In this Section, the polar and surface plots have been omitted for reasons of clarity. The trends of the corresponding curves

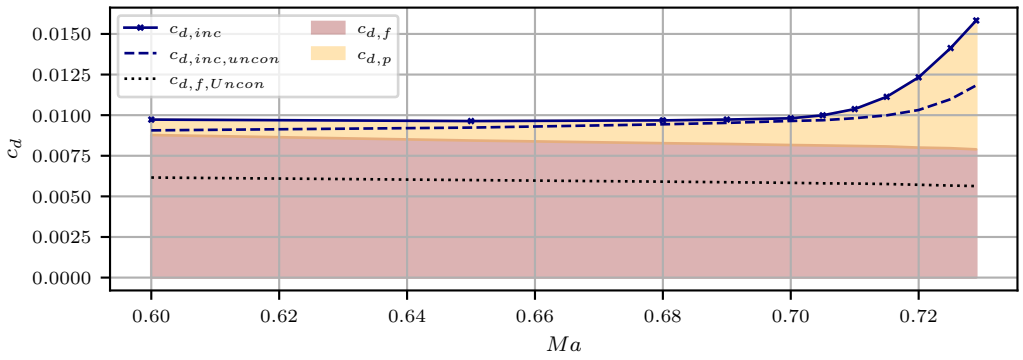


Figure 5.11: Drag distribution for different Mach numbers for suction on the suction side with a control magnitude of $m_{BLC} = 0.2\%\dot{m}_\infty$ and an angle of attack of $\alpha = 2.31°$.

have already been described in detail in the previous sections. The Mach number regime covers the range from subsonic $Ma < 0.7$ up to the transonic regime $Ma \geq 0.7$, where a clear shock is observed at the upper side of the airfoil. An increase in the Mach number leads to, first, the appearance of the shock and, later, to a shift of the shock towards the trailing edge and an increase in magnitude.

In Figure 5.11, the drag distribution is shown. The components for the controlled cases are shown by the colored areas and the blue line, while the uncontrolled components are marked by the dashed and dotted lines. For the uncontrolled and the controlled cases, a slight decrease in the friction drag is observed with an increase in the Mach number. The friction drag of the uncontrolled case is lower compared to the controlled one, which can be explained by the applied control of suction on the suction side, which leads to an increase in the friction drag, as already seen in Section 5.3.1. The inclusive drag, so the sum of the pressure and body drag, which already includes the boundary layer control penalty, is almost constant for both the controlled and the uncontrolled case up to a Mach number of $Ma = 0.7$. At this Mach number, the shock appears, which leads to a significant increase in the pressure drag. With a further increase in the Mach number, also the pressure drag increases, which is due to the increase in the shock's magnitude. At $Ma = 0.725$, the pressure drag is responsible for about 46% of the total drag.

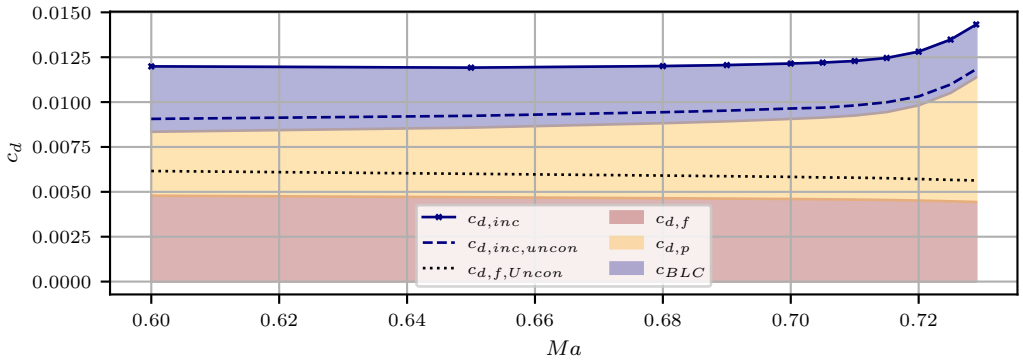


Figure 5.12: Drag distribution for different Mach numbers for blowing on the pressure side with a control magnitude of $m_{BLC} = 0.2\%\dot{m}_\infty$ and an angle of attack of $\alpha = 2.31°$.

The effect of the variation of the Mach number for blowing on the pressure side is shown in Figure 5.12. Since the control is applied to the lower side of the airfoil, the influence on the flow and thus

the shock's characteristics on the upper side is rather low. However, due to the variation of the Mach number, a shift of the shock position as well as an increase in magnitude is still observed. But no significant variation between the controlled and uncontrolled cases can be seen on the upper side. In the drag distribution in Figure 5.12, it can be observed that the trend is similar to the cases with suction on the suction side because the main reason for the increase of the pressure drag component can be explained by the shift of the shock, which is mainly driven by the variation of the Mach number. This effect can be increased by the control of suction on the suction side. The comparison of the uncontrolled and controlled configurations for blowing on the pressure side shows an increased friction drag compared to the uncontrolled case, contrary to the suction case. Blowing increases the boundary layer thickness and thus leads to a reduction of the friction drag. As already observed in the previous case, the appearance of the shock at $Ma \approx 0.7$ leads to a significant increase of the pressure component." [FG25]

5.3.4 Effect of Control Position

"The influence of the control position is shown in Figure 5.13 for the transonic Mach number of $Ma = 0.725$ and the control configurations of blowing on the suction side and suction on the suction side in the left and right columns, respectively. The default control area spans 60% of the chord length, while the smaller areas of before, across, and behind the shock span 10% of the chord length. The positions are defined concerning the shock position in the uncontrolled case, see Figure 5.4. The effect of the control, so a shift of the shock position and change in magnitude, can also be observed for the smaller control areas for both investigated control configurations, but with a much smaller effect, see Figure 5.4 a) and b). The control intensity depends on the freestream flow, and therefore, the total mass flow is smaller due to the smaller area through which the flow passes. The trend of the friction coefficient shows that only the areas in which the control is applied show a large difference from the uncontrolled case. It can also be seen that the shift of the shock is the same for the positions before and behind the shock, while the shift of the shock for the control at the shock position is minimally larger but still significantly smaller than in the default case." [FG25]

5.3.5 Effect of Reynolds number

"The parametric study was performed at a constant Reynolds number of $Re = 5 \times 10^6$ since the computational costs for a variation of the Reynolds number for the whole parametric study would have been too high. To see the effect of this variation, Reynolds numbers between $Re = 2 \times 10^6 - 12 \times 10^6$ are tested for the case of a Mach number of $Ma = 0.725$ and at a constant lift coefficient of $c_l = 0.695$ (which corresponds to the uncontrolled case at a Reynolds number of $Re = 5 \times 10^6$ and an angle of attack of $\alpha = 2.31°$). Figure 5.14 shows the body drag as a function of the Reynolds number for the uncontrolled case as well as for the controlled cases of suction on the suction side and blowing on the pressure side. Overall, the body drag is decreasing for all investigated configurations, but the rate of the decrease decreases with increasing Reynolds number. Also, the difference between the uncontrolled body drag and the controlled body drag decreases. Thus, the effects on the efficiencies are also decreasing. While at a Reynolds number of $Re = 5 \times 10^6$ for the investigated case, an efficiency increase of 2.7% is observed, at a Reynolds number of $Re = 10 \times 10^6$, the efficiency increase is 1.9%. The efficiency is calculated with the body drag, thus, the costs for the control are not taken into account for this discussion.

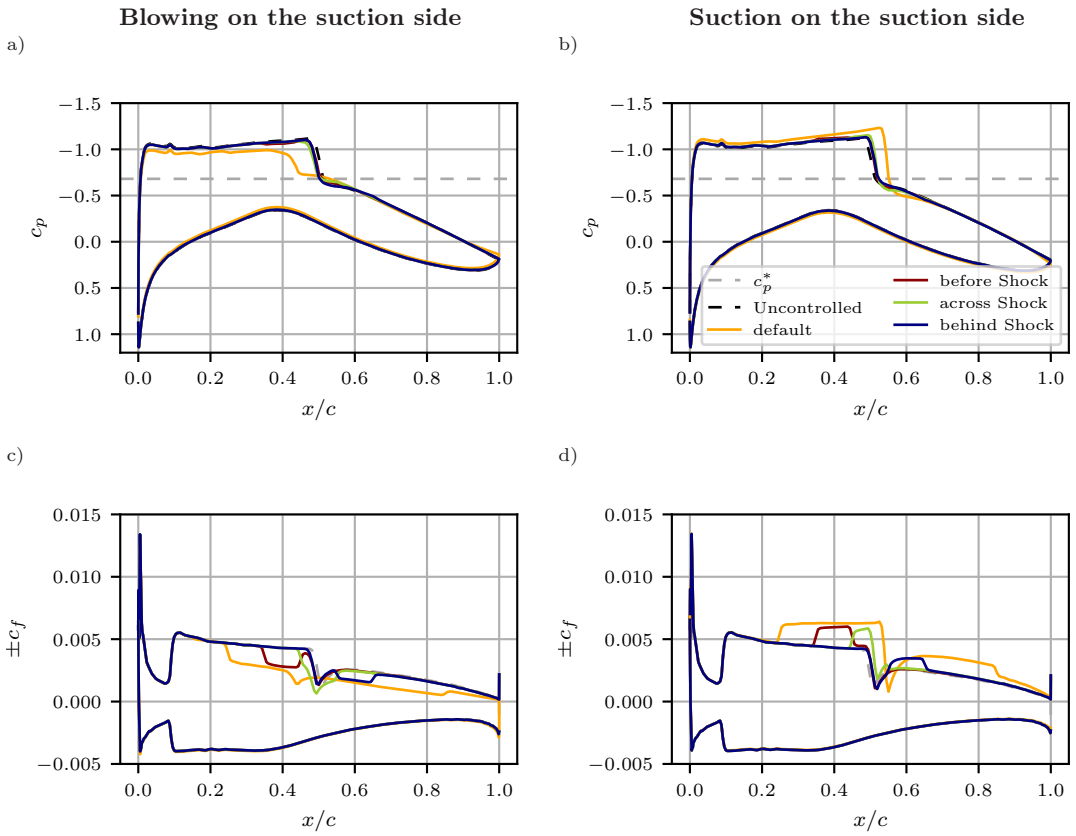


Figure 5.13: Polar plot and pressure and friction coefficient distribution for different control positions and the uncontrolled reference case. The applied control is blowing on the suction side and suction on the suction side for the left and right columns, respectively, with a control magnitude of $m_{BLC} = 0.1\%\dot{m}_\infty$. The surface plots are shown for an angle of attack of $\alpha = 2.31°$.

In order to make a precise and detailed prediction about the influence of the Reynolds number, a more broadly diversified parametric study would have to be carried out. In the investigated set of mesh generation, code, and parameters used here, a wider range of Reynolds numbers cannot be covered. A more detailed discussion of the realization of the presented flow control method can be found in the Concluding discussions." [FG25]

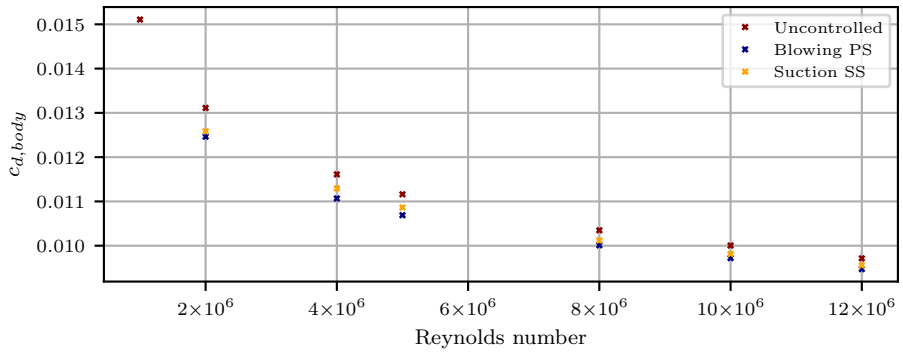


Figure 5.14: Variation of the Reynolds number for one single configuration at a Mach number of $Ma = 0.725$ and a constant lift coefficient of $c_l = 0.695$.

5.4 Efficiency Increasing Configurations

"The previously discussed results show that there are a few configurations where an increase in efficiency was observed. In this subsection, these cases should be analyzed in more detail.

The only control configuration that showed an increase in efficiency is suction on the suction side at low control magnitudes of $\dot{m}_{BLC} = 0.1\%\dot{m}_{\infty}$ in the default control area. Promising cases have been observed throughout the whole investigated range of Ma numbers. For the following comparison, three example Mach numbers were chosen: 0.65 to represent a subsonic case and 0.71 and 0.725 in the transonic regime. All the cases are listed in Table 5.2.

Table 5.2: Example cases of suction on the suction side, which promise an increase in efficiency. The uncontrolled cases are rerun at the same lift coefficient as the controlled cases for a better comparison.

Ma	$\dot{\mathbf{m}}_{\mathbf{BLC}}$	**AoA**	$\mathbf{c_l}$	$\mathbf{c_{d,body}} \cdot 10^2$	**E**	
0.65	0.1	$-1°$	0.121	0.83	15.57	-3.78%
0.65	-	$-0.797°$	0.121	0.80	15.15	
0.65	0.1	$0°$	0.277	0.84	33.11	-2.27%
0.65	-	$0.224°$	0.277	0.82	33.87	
0.65	0.1	$1°$	0.434	0.86	50.21	-0.46%
0.65	-	$1.250°$	0.434	0.86	50.44	
0.65	0.1	2○	0.592	0.91	65.35	**1.54%**
0.65	-	$2.279°$	0.592	0.92	64.37	
0.65	0.1	$3°$	0.752	0.98	76.59	**5.75%**
0.65	-	$3.324°$	0.752	1.04	72.42	
0.71	0.1	$-1°$	0.127	0.83	15.30	-2.22%
0.71	-	$-0.785°$	0.127	0.81	15.65	
0.71	0.1	$0°$	0.303	0.84	36.16	-0.25%
0.71	-	$0.241°$	0.303	0.84	36.25	
0.71	0.1	$1°$	0.481	0.87	55.15	**2.17%**
0.71	-	$1.276°$	0.481	0.89	53.98	
0.71	0.1	$2°$	0.667	0.94	71.16	**4.56%**
0.71	-	$2.318°$	0.667	0.98	68.06	
0.71	0.1	$3°$	0.870	1.35	64.60	**14.96%**
0.71	-	$3.374°$	0.870	1.55	56.19	
0.725	0.1	$-1°$	0.129	0.83	15.49	-1.73%
0.725	-	$-0.780°$	0.129	0.82	15.76	
0.725	0.1	$0°$	0.312	0.82	37.17	**0.45%**
0.725	-	$0.252°$	0.312	0.84	37.00	
0.725	0.1	$1°$	0.500	0.88	56.92	**3.28%**
0.725	-	$1.290°$	0.500	0.91	55.11	
0.725	0.1	$2°$	0.700	1.06	66.26	**4.76%**
0.725	-	$2.332°$	0.700	1.11	63.25	
0.725	0.1	$3°$	0.896	1.98	45.29	**22.59%**
0.725	-	$3.574°$	0.896	2.43	36.94	

The controlled cases are now compared to uncontrolled cases at the same lift coefficient instead of the same angle of attack. The uncontrolled simulations were rerun at the same c_l from the corresponding controlled cases. This change in comparison is especially important for those cases that are far from the design angle of attack. In fact, in this case, the control at low AoA configurations

showed a high efficiency increase compared to the uncontrolled cases at the same AoA. However, a comparison at the same lift coefficient has shown that these configurations are far from increasing the efficiency.

For all configurations, the angle of attack for the uncontrolled cases is slightly higher, $\Delta\alpha = 0.2° - 0.6°$, compared to the uncontrolled cases. A comparison of the controlled cases with the corresponding uncontrolled cases at the same lift coefficient showed that with increasing AoA, the effectiveness of suction improves so that for large AoA the control does induce an overall net efficiency increase. For lower Mach numbers, the efficiency increase is smaller than for the higher transonic cases. In the subsonic regime, a maximum efficiency increase of about 5.75% is reached for a lift coefficient of $c_l = 0.752$. For the controlled case, this corresponds to an angle of attack of $\alpha = 3°$, and for the uncontrolled case of $\alpha = 3.32°$. In the fully transonic regime, the efficiency increase is 22.59% for $c_l = 0.897$ for a controlled angle of $\alpha = 3°$ and for the uncontrolled case $\alpha = 3.574°$. The maximum absolute value of the efficiency of $E = 62.25$ is reached for a lift coefficient of $c_l = 0.700$. An application of the active control in this case led to an increase in the efficiency of 4.76%.

A visualization of the efficiency increase for the different Mach numbers and angles of attack for the controlled cases is shown in Figure 5.15. It can be seen that an increase in Mach number as well as an increase in the angle of attack (of the controlled case) leads to an increase in the efficiency.

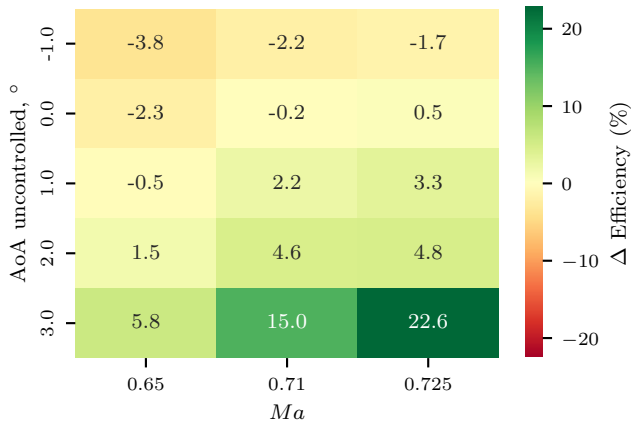


Figure 5.15: Efficiency increase for suction on the suction side at three different Mach numbers of $Ma = 0.65$ as a representation of the subsonic case and $Ma = 0.71$ and 0.725 as representations for the transonic cases without the power consumption.

As already discussed in Section 5.1.4, the active control method needs extra energy, which was not taken into account so far. To get an estimation of whether the control works and increases the efficiency, this extra power needs to be calculated. For all controlled cases, the minimal c_p value in the control area on the suction side was determined. Since all configurations in this chapter are of the control type suction, only the minimal c_p value needs to be taken into account. With the calculated pressure difference, the pump drag was determined by Equation 5.11. The calculated values are shown in Table 5.3. The thrust that can be generated by dumping the fluid is calculated with the boundary layer penalty of Eq. 5.8. With the body drag, the generated thrust, and the pump drag, the total drag of the controlled cases was calculated. The newly calculated efficiency was then compared to the uncontrolled cases at the same c_l. Since the new total drag increased compared to the total drag without the energy consumption, the efficiency decreased. Now, most

of the configurations show a decrease in efficiency. Also, the case with the largest efficiency at $Ma = 0.725$ and $\alpha = 2°$ is now decreased by about -3.56%. An increase in efficiency can still be observed for configurations at high angles of attack. With a net efficiency of $E = 42.75$ in the 3° controlled case, an increase of 15.72% compared to the uncontrolled case was reached. This most promising configuration, achieved at a Mach number of 0.725, a control magnitude of $\dot{m}_{BLC} = 0.1\%\dot{m}_\infty$ and the control of suction on the suction side at $\alpha = 3°$, is shown in Figure 5.17 and compared to the uncontrolled case at $\alpha = 3.574°$.

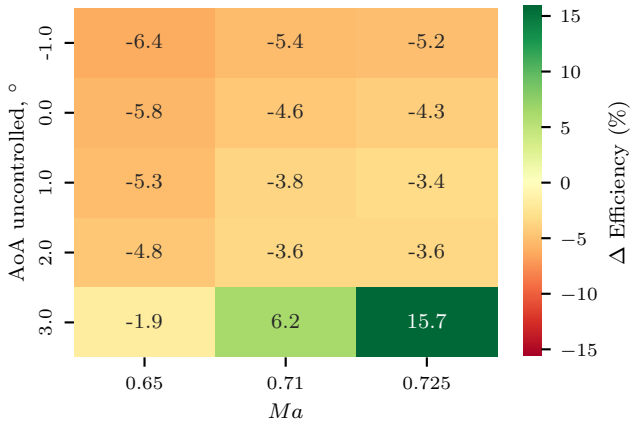


Figure 5.16: Efficiency increase for suction on the suction side at three different Mach numbers of $Ma = 0.65$ as a representation of the subsonic case and $Ma = 0.71$ and 0.725 as representations for the transonic cases with the power consumption.

In Figure 5.16, the change in efficiency of the controlled compared to the uncontrolled cases with low magnitude suction on the suction side is shown. As already observed before, an increase in Mach number and angle of attack (of the controlled cases) leads to higher values in ΔE, but by taking into account the calculation of the power consumption, most of the cases now show an efficiency decrease. Only the high lift configurations in the transonic regime show an efficiency increase.

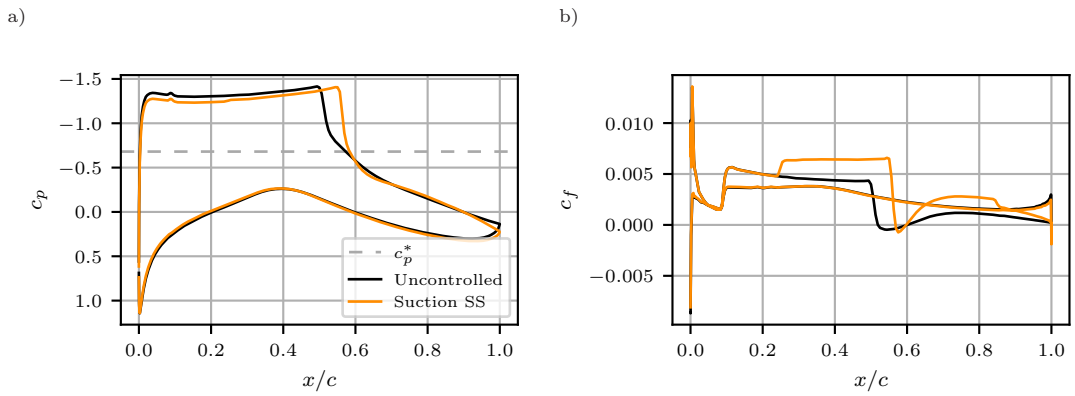


Figure 5.17: Pressure and friction coefficient of the most promising configuration for $Ma = 0.725$, $m_{BLC} = 0.1\%\dot{m}_\infty$ and $\alpha = 3°$ or 3.567° for the controlled (suction on the suction side) and uncontrolled case, respectively.

In the uncontrolled case, the pressure coefficient on the upper side before the shock is lower compared to the controlled case. As already seen in the previous results, suction on the suction side shifts the shock towards the trailing edge, even though now two configurations with the same c_l are compared instead of the same AoA. In the plot of the friction coefficient, a flow separation on the suction side in the uncontrolled case can be observed right after the shock took place. The flow reattaches, and the friction coefficient recovers at about $x/c = 0.6$. In the controlled suction case, an increased friction coefficient in the controlled area can be observed. Although the friction coefficient is significantly higher than in the uncontrolled case, the shift of the shock position towards the trailing edge and the increase in magnitude still lead to a flow separation right after the shock takes place. The recovery of the friction coefficient is much faster than in the uncontrolled case, and only a very small separation bubble can be observed, but a flow separation cannot be prevented by the active flow control.

As already mentioned in Section 5.1.4, the estimation of the power consumption is very conservative and probably lower in a real-life scenario, as the pressure difference between the supply chamber and the airfoil's surface is very large in the region after the shock. Nevertheless, there are a few configurations where, even with the conservative power calculation, a net drag saving could be achieved. Additionally, no optimization of different configurations was conducted so far, and some non-optimal cases were investigated as well to get an idea of the potential of the investigated control method." [FG25]

Table 5.3: Calculation of the power consumption and thrust generation to get a better estimation of the real drag savings for three example Mach numbers. The uncontrolled cases are shown in Table 5.2.

Ma	AoA	$c_{d,body} \cdot 10^2$	$c_{p,min}$	$c_{BLC} \cdot 10^2$	$c_{pump} \cdot 10^2$	$c_{D,total} \cdot 10^2$	E_{total}	
0.65	$-1°$	0.83	-0.49	-0.17	0.19	0.85	15.08	-6.35%
0.65	$0°$	0.84	-0.56	-0.17	0.20	0.87	35.85	-5.76%
0.65	$1°$	0.88	-0.67	-0.17	0.21	0.92	54.21	-5.28%
0.65	$2°$	0.91	-0.80	-0.17	0.23	0.97	61.29	-4.78%
0.65	$3°$	0.98	-0.94	-0.17	0.24	1.06	71.08	-1.86%
0.71	$-1°$	0.83	-0.56	-0.15	0.18	0.86	14.80	-5.42%
0.71	$0°$	0.84	-0.65	-0.15	0.19	0.88	34.60	-4.56%
0.71	$1°$	0.87	-0.80	-0.15	0.21	0.93	51.93	-3.80%
0.71	$2°$	0.94	-1.03	-0.15	0.23	1.02	65.64	-3.57%
0.71	$3°$	1.35	-1.32	-0.15	0.26	1.46	59.70	**6.24%**
0.725	$-1°$	0.83	-0.59	-0.15	0.18	0.86	14.94	-5.19%
0.725	$0°$	0.84	-0.69	-0.15	0.19	0.88	35.43	-4.25%
0.725	$1°$	0.88	-0.87	-0.15	0.21	0.94	53.26	-3.36%
0.725	$2°$	1.06	-1.16	-0.15	0.24	1.15	60.99	-3.56%
0.725	$3°$	1.98	-1.41	-0.15	0.27	2.10	42.75	**15.72%**

5.5 Discussions of the Parametric Study

This study investigated wall-normal blowing and suction as an active flow control method for improving the aerodynamic efficiency of a transonic airfoil under fully turbulent boundary layer conditions. The results of the investigated parameter range showed that suction on the suction side emerged as the only configuration capable of providing a net aerodynamic benefit when the inclusive drag and the required control power were taken into account.

The results demonstrated that the effectiveness of the control strongly depends on the flow regime, control magnitude, and operating conditions. In the subsonic regime, no improvements were observed in the efficiency. In contrast, the transonic regime showed a stronger sensitivity to the control due to the interaction with the shock. Suction shifted the shock position downstream and increased its magnitude, which resulted in a favorable lift-to-drag ratio for low control magnitudes. While suction reduces pressure drag, it simultaneously increases skin-friction drag because of the thinner boundary layer. For low suction intensities, however, the aerodynamic benefit outweighed these penalties, leading to efficiency gains.

Blowing configurations consistently failed to improve the aerodynamic efficiency despite reducing friction drag, as the associated increase in pressure drag dominated the overall behavior. The study therefore indicates that friction alone is not sufficient to achieve a net performance improvement in transonic conditions when the total drag balance is considered.

The study showed that efficiency improvements were limited to configurations with low suction magnitudes. Increasing the control magnitude amplified both the beneficial and adverse effects, eventually leading to higher overall drag levels and a reduction in efficiency. In addition, the exact streamwise position of the control region appeared to be of secondary importance compared to the selected control type and control intensity.

When accounting for the estimated power consumption of the active system, several low-intensity suction cases achieved measurable efficiency improvements. Nevertheless, the most favorable configurations did not coincide with typical cruise operating conditions for the investigated airfoil. Consequently, the present results suggest that homogeneous wall-normal suction has potential as an active flow control method in transonic flow, but further optimization and integration with additional concepts are required before practical aerodynamic benefits at realistic operating conditions can be fully assessed.

5.6 Bayesian Optimization

The conducted parametric study demonstrated that wall-normal suction can positively influence the aerodynamic performance of the transonic airfoil. However, due to the large number of possible actuation configurations and the strong nonlinear interaction between the shock position, boundary layer behavior, and control intensity, a systematic exploration of the design space is required in order to assess the full potential of the active flow control strategy. For this reason, a small Bayesian Optimization framework was employed in the present work to efficiently identify optimal blowing and suction distributions while minimizing the number of computationally expensive CFD evaluations. The following investigation was carried out in collaboration with researchers from KTH Royal Institute of Technology in Sweden and forms part of a conference proceeding, Mallor et al. [MFR+23].

5.7 Methodology

The numerical setup and the implementation of the boundary conditions are based on the methodology presented in Section 5.1, where further details regarding the numerical discretizations, turbulence modeling, mesh generation, and boundary treatment are provided.

"The allowed intensity of the wall-normal mass flow (positive for blowing and negative for suction) is limited to 0.25% of the freestream mass flow. Two additional constraints are imposed on the

optimization: the total length of the blowing region must be at least 10% of the chord, and the sum of the total suction and blowing massflows must be the same so that the overall active control results in zero net mass flux. The former is used to avoid major discontinuities in the solution, which could undermine stability, and whose effect can hardly be captured by RANS simulations. The latter constraint was imposed in order to study a self-contained flow control system, in which no additional air must be supplied or exhausted from the free-stream. In order to estimate the power of the actuation, we consider a simplified system in which a single compressor (or turbine) connects the suction and blowing regions. The power required to operate the control system can be computed as the mass flowing across the compressor times the change in total enthalpy (Δh_t). Using the isentropic relations, the expression can be rearranged to depend on the total pressure ratio across the compressor and the inflow temperature:

$$P = \dot{m} c_{sh} T_s \left(\left(\frac{p_b}{p_s} \right)^{\frac{\gamma-1}{\gamma}} - 1 \right) \tag{5.13}$$

where c_{sh} is the specific heat constant, γ the specific heat ratio, $\dot{m}$ the massflow, T_s the suction air temperature and p_b and p_s the blowing and suction pressures, respectively. The pressure ratio is given by the regions in which the flow control is applied: p_b is taken as the maximum pressure of the blowing region, whereas p_s is fixed from the point of minimum pressure of the suction region. Moreover, the efficiency (η) of the compressor can be taken into account easily: $P_\eta = P/\eta$. In the present work, three different cases are considered:

- $\mathbf{min}(\mathbf{c_D})$: Only the drag is accounted for in the maximization of the efficiency;
- $\mathbf{min}(\mathbf{c_D} + \mathbf{c_P})$: Both drag and the power needed to drive the control actuation are used in the denominator of the efficiency ($E_{power} = c_L/(c_D + c_P)$);
- $\mathbf{min}(\mathbf{c_D} + \mathbf{c_{P_\eta}})$: The actuation power is computed assuming a compressor efficiency (η) equal to 0.8.

Lastly, the temperature at the outlet of the compressor is prescribed as a fixed value boundary condition for the region in which blowing is applied. The temperature is computed using the isentropic relations and the pressure ratio across the compressor as follows:

$$T_b = T_s \left(\frac{p_b}{p_s} \right)^{\frac{\gamma-1}{\gamma}} \tag{5.14}$$

A surrogate model of the aerodynamic response as a function of the prescribed control actuation parameters is built using a Gaussian Process Regression (GPR [60]) with the open-source library GPy (see reference [26]). The parameters of the GPR (with a Matern52 kernel for the covariance function) are fitted using the available observations obtained by simulating the flow with some prescribed control boundary conditions (BC) in SU2. Moreover, in order to accelerate convergence, we impose the symmetry inherent in the problem by interchanging the beginning and end points (*i.e.* at each iteration, two values are stored: the original one, and one in which the start and end point values are swapped).

In order to draw the sequence of training samples (i.e. the parameter of the control schemes to be simulated next), the expected improvement (EI) acquisition function is maximized (for a detailed description of the EI function and its application to GPR, we refer the reader to the second section in the work by [46]). Using a hyperparameter ξ, a balance between exploration (minimizing parts of the parameter space with high variance) and exploitation (maximizing the use of the best objective)

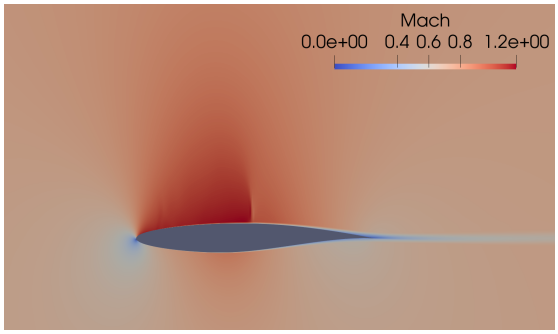


Figure 5.18: Distribution of the local Mach number around the airfoil for the reference simulation without active control.

is established. In the present case, we set $\xi = 1 \cdot 10^{-3}$. For the GPR-BO, the library GPyOpt [see reference 27] is used.

In the present work, the aerodynamic characteristics of the uncontrolled airfoil at an angle of attack (α) of 2° are used as a baseline in order to compare the effectiveness of the control actuation. In this baseline case (see Figure 5.18), the lift (c_L) and drag (c_D) coefficients are equal to $6.38 \cdot 10^{-1}$ and $9.89 \cdot 10^{-3}$, respectively, giving an aerodynamic performance ($E = c_L/c_D$) of 64.5. The objective is to increase the aerodynamic performance while maintaining the same lift force (i.e. reducing c_D). This is achieved by correcting the angle of attack using a Newton method implemented in SU2 until the c_L matches the baseline in each of the studied control cases." [MFR+23]

Table 5.4: Aerodynamic properties and power consumption of the optimal control strategies.

Case	AoA	c_D	c_P	$\dot{m}$	E	E_{power}
Baseline	2.0	$9.89 \cdot 10^{-3}$	0.0	0.0	**64.50**	-
$\min(c_D)$	1.41	$9.31 \cdot 10^{-3}$	$2.90 \cdot 10^{-3}$	11.89	**68.48**	52.22
$\min(c_D + c_P)$	1.92	$9.65 \cdot 10^{-3}$	$1.12 \cdot 10^{-4}$	1.37	66.11	**65.35**
$\min(c_D + c_{P_\eta})$	1.88	$9.60 \cdot 10^{-3}$	$1.74 \cdot 10^{-4}$	2.21	66.43	**65.24**

5.8 Results

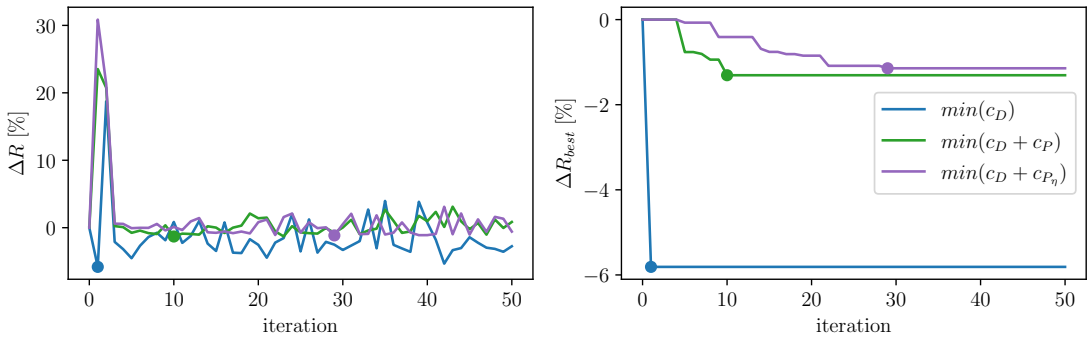


Figure 5.19: Evolution of the response (as a relative percentage change versus the baseline case) with the number of iterations (left) and cumulative best response found (right).

"For each of the three optimization scenarios, 50 simulations were carried out, and the aerodynamic performances obtained for the best cases found in each of them are reported in Table 5.4. The evolution of the response (objective of the minimization) is shown in Figure 5.19. As seen in

the right panel, the optimal response was found earlier than the 50^{th} iteration in all cases. From that point on, the optimization process explored the parameter space and reduced the uncertainty around the point of maximum power efficiency gain. As the complexity of the objective function increases (by taking into account the control actuation power and efficiency), the number of iterations needed to reach the optima increases. Given the complexity of the cases (the presence of a shock, the requirement to maintain a constant c_L), and the number of optimization parameters, the fact that convergence to an optimal strategy was achieved in such few flow realizations supports the effectiveness and robustness of BO-GPR as a flow optimization tool. Moreover, the method works as a black box and is non-intrusive, i.e. it does not require to perform any sort of adjoint or gradient computations within the numerical simulation.

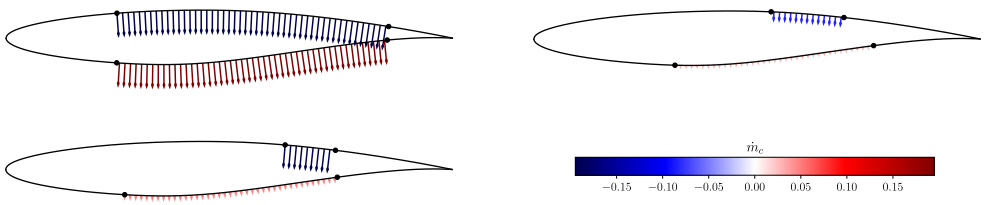


Figure 5.20: Best control strategy found after the optimization process for the case in which the drag is minimized (top left), and for the cases in which the cost of the control actuation is taken into account in the objective function (top right and bottom left represent the cases with η equal to 1 and 0.8, respectively).

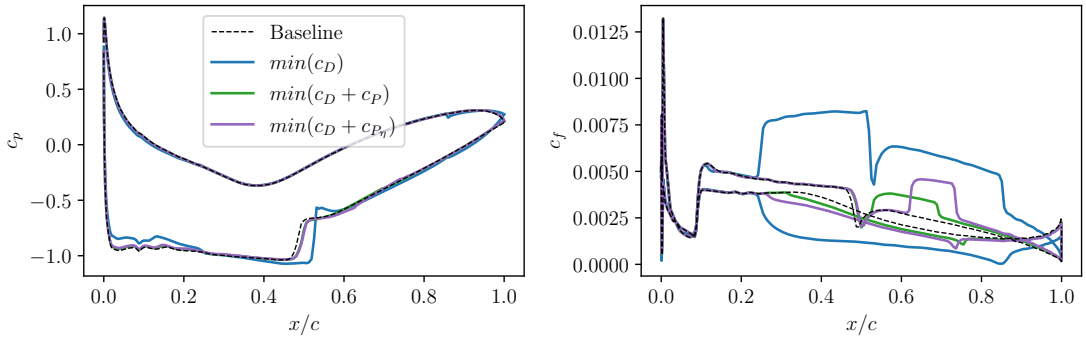


Figure 5.21: Pressure c_p (left) and skin-friction c_f coefficient (right) obtained after the optimization process. The baseline case is represented with a black, dashed line, and the best control strategy with a solid line. The color coding refers to the three considered optimization cases as reported in the legend.

As shown in Figure 5.20, all control configurations which lead to an increase in the aerodynamic efficiency share a common feature across the different optimizations: mass-flow ingestion (suction) takes place on the suction side, while mass-flow (blowing) is injected into the pressure side. Clear differences in the optimal control actuations appear once the power, and not just the drag, is taken into account in the efficiency calculation: For the min(c_D) case, the control is applied at its maximum allowed strength over the whole admissible control region. The strong suction over the span of the suction side leads to a more attached flow, causing the circulation around the airfoil to increase, and hence increasing its lift coefficient. As the lift coefficient is fixed, this in turn leads to a decrease in the angle of attack required to obtain the required lift. The reduction in angle of attack (1.4° versus the baseline 2°) results in a downstream shift of the position of the shockwave which (clearly seen both in the pressure and friction coefficient distributions shown in Figure 5.21), together with the reduction in friction drag over the pressure side due to blowing (see the right plot of Figure 5.21), leads to a substantial reduction in the drag coefficient: The aerodynamic

efficiency improves by 6.2%. However, as the power depends directly on the maximum pressure ratio across the two control regions, sucking air from the position upstream of the shockwave (where the pressure ratio is high) is not power-efficient, which translates into a decrease of E_{power} compared to the baseline case (see Table 5.4), i.e. no net power saving can be achieved. This feature is clearly reflected in the optimal control actuations found for the cases in which the power actuation was part of the optimization objective: as seen in Figure 5.20, no suction is performed before the position of the shock. This leads to a smaller downstream shift of the shockwave (around 1.5 versus 4% of the chord for the previous case), resulting in more moderate gains in terms of the aerodynamic efficiency. On the other hand, the actuation over the pressure side remains virtually unchanged, as the air ingested on the suction side is exhausted uniformly over the control region on the pressure side. Even though the gains in power efficiency are moderate (1.32 and 1.15% for the case with η equal to 1 and 0.8, respectively), the optimal actuation strategies still yield an increased aerodynamic performance when compared to the baseline case, which has not been observed in previous studies.

While RANS convergence for the aerodynamic coefficients after 30000 iterations is well below the significant digits reported here, the modeling error due to RANS may be larger than the small performance improvement margin measured in the present study for such a complex flow scenario. A more robust verification of the present results through well-resolved LES is planned. If included into the multifidelity framework developed by [62], the results of more accurate LES simulations will not only serve as validation but can be utilized to improve the whole surrogate model of the aerodynamic response.

Besides the current uncertainty related to the RANS simulations, the present results show that improving the aerodynamic efficiency via wall-normal blowing and suction is theoretically possible, also when the ideal cost of the active control strategy is taken into account. We were able to achieve these results thanks to a Bayesian optimization framework, which could find the optimal blowing and suction configurations within the very large parameter space. The small improvement in net aerodynamic efficiency should not be a surprise. On the one hand, the airfoil shape is already optimized for cruise flight at the reference conditions. A holistic approach, in which both the airfoil shape and active control are designed and optimized together, could yield better results. On the other hand, we limited ourselves to considering active control in the turbulent region of the airfoil." [MFR+23]

6 Comparison of Streamwise Travelling Waves and Uniform Suction on a Supercritical Airfoil

This Chapter is based on the publication *Comparison between Localized Skin-Friction Reduction and Suction on a Supercritical Airfoil* by Frede et al. and presents the methodology and results of the corresponding investigation. The study compares the active flow control techniques of wall-normal suction and streamwise travelling waves of spanwise velocity under compressible and transonic flow conditions. Particular attention is given to the physical mechanisms responsible for the improvement in aerodynamic efficiency and to the differences in the underlying control mechanisms of the two approaches. The analysis focuses on the interaction between shock-wave behavior, turbulent boundary layer development, and drag reduction in order to assess to what extent the dominant efficiency-enhancing mechanisms differ between suction and StTW control.

6.1 Methodology

6.1.1 Numerical methods

"Direct Numerical Simulations of the turbulent flow are performed with the solver FLEW, developed by Soldati et al. [70], which is based on the work of Pirozzoli [53]. FLEW is specialized for simulations of compressible flow over complex geometries, such as airfoils, and extends the Cartesian-based solver STREAmS [11] to curvilinear structured grids while preserving the high efficiency and state-of-the-art numerical schemes.

The computational domain is discretized using a structured hexahedral grid, which enables the use of standard finite-difference techniques. The compressible Navier-Stokes equations are solved with a hybrid numerical scheme proposed by Pirozzoli [52]. This approach combines central schemes, which minimize the numerical dissipation and are ideal for accurately resolving turbulent structures, with Weighted Essentially Non-Oscillatory (WENO) schemes [41], which are essential for capturing shock waves. Since central schemes can be prone to nonlinear instabilities, FLEW employs a stabilization technique based on the skew-symmetric splitting of convective derivatives [52], which preserves the global kinetic energy in the inviscid and low Mach number regime.

The spatial derivatives are first calculated in the computational space and then transformed into the physical space using metric coefficients, which are derived from the geometry of the physical mesh. The same schemes used for the convective derivatives are employed to compute the metric terms to preserve a uniform free stream [77], which is essential for complex geometries. Central differencing achieves eighth-order accuracy for both convective and viscous terms, while the WENO discretizations reach seventh-order accuracy.

FLEW is optimized for large-scale simulations on high-performance computing systems. It supports scalable parallelism via the Message Passing Interface (MPI) and is fully compatible with modern GPU-based architectures widely used in supercomputing facilities." [FSP+26]

6.1.2 Computational Setup

"The body-fixed coordinate system is defined with its origin located at the airfoil leading edge. The X-axis is aligned with the chord line and directed downstream, the Y-axis is normal to the chord and oriented upward, and the Z-axis is oriented spanwise. A second reference frame, the local surface coordinate system, is introduced for the analysis of the boundary layer characteristics. In this system, the tangential coordinate ξ lies along the local surface tangent, while the normal coordinate η corresponds to the direction of the local surface normal. The two coordinate systems are sketched in Figure 6.1a).

The present study investigates the supercritical airfoil V2C, originally designed within the European project TFAST [15]. [...] The simulations are performed at an angle of attack of $\alpha = 4°$, which corresponds to the point of the maximum lift-to-drag ratio. The chord based Reynolds number is set to $Re_\infty = U_\infty c/\nu_\infty = 3 \times 10^5$, where U_∞ is the free stream velocity, ν_∞ the kinematic viscosity, and c the chord length. The free-stream Mach number is $Ma_\infty = U_\infty/a_\infty = 0.7$, with a_∞ denoting the speed of sound at free stream conditions.

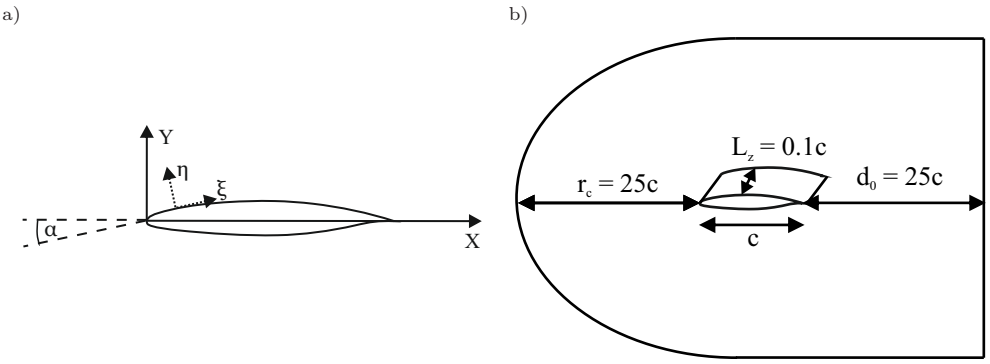


Figure 6.1: a) Sketch of the different coordinate systems used for the analysis of the simulation, and b) sketch of the mesh and the corresponding length scales.

To enforce a steady laminar-to-turbulent flow transition on both sides of the airfoil $0.1c$ downstream from the leading edge, a numerical tripping in the form of a localized small Gaussian blob of wall-normal random volume forcing is applied [68]. The tripping force is set to $150U_\infty^2/c$, ensuring the proper development of a fully turbulent boundary layer. The displacement thickness is approximated with $\delta^* = 0.001c$ at the tripping location to calculate the length scales of the tripping parameters as the spanwise wavelength $\lambda_Z = 1.7\delta$, and the spatial Gaussian attenuation of the forcing region $L_X = 4\delta$ and $L_Y = \delta$, as well as the period $T = L_X/U_\infty$.

The characteristic length c and the free-stream velocity U_∞ are used as reference scales to nondimensionalize all quantities and the governing equations. In addition to these outer scales, a viscous scaling is introduced, where the friction velocity $u_\tau = \sqrt{\tau_w/\rho}$ serves as the velocity reference and the viscous length scale ν/u_τ as the reference length. Here, τ_w, ρ, and ν denote the wall shear stress, fluid density, and kinematic viscosity, respectively. Variables normalized using viscous units based on the reference case (i.e., without active flow control) are denoted with a superscript '+', while those scaled by the friction velocity of each case carry a superscript '*'. It is important to note that the wall shear stress exhibits significant spatial variations along the surface. In this study, friction-related quantities are evaluated on the upper side at $X = 0.35$. This location is chosen because it lies sufficiently downstream for the effects of actuation to develop, yet remains far enough upstream of the shock region for the wall pressure gradient to remain approximately

constant across all cases. [10] also chose a fixed position to evaluate the friction-related quantities and showed that the choice does not impact the qualitative form of the results.

The computational mesh has a C-type topology and consists of $4096 \times 512 \times 256$ cells. In the radial direction, the domain extends up to 25 chord lengths, while the spanwise extent is $L_Z = 0.1$. The spanwise depth of the computation domain is sufficient to accommodate all relevant turbulent structures and to achieve spanwise decorrelation of the flow [59, 10]. Grid cells are uniformly spaced in the spanwise direction, while a hyperbolic tangent distribution is used in the wall-normal direction. The mesh resolution satisfies the criteria for a fully resolved DNS, with near-wall spacings of $\Delta X^+ < 10$ (streamwise), $\Delta Y^+ < 0.5$ (wall-normal), and $\Delta Z^+ < 5$ (spanwise). A schematic sketch of the computational domain is shown in Figure 6.1b).

Periodic boundary conditions are applied in the spanwise direction. At the far field, non-reflecting boundary conditions based on the characteristic wave approach [54] are used to prevent the reflection of pressure waves back toward the airfoil. In the reference case, the airfoil surface is modeled with no-slip, adiabatic wall conditions." [FSP+26]

The active boundary layer control is implemented through localized wall forcing applied on the suction side of the airfoil. Depending on the selected control mode, either the control via travelling waves or steady suction (or blowing) is imposed.

"For both control methods, a smoothing function [83] is applied over a distance of $\Delta x_{sm} = 0.05$ at the beginning and end of the control region to ensure a smooth transition between the uncontrolled and controlled flow. The smoothing function is given by

$$f_{sm}(X) = \frac{1}{2}\left[\tanh\left(\frac{X - X_b}{\Delta X_{sm}}\right) - \tanh\left(\frac{X - X_e}{\Delta X_{sm}}\right)\right]." \tag{6.1}$$

[FSP+26]
The start of the control region is denoted by X_b and the end by X_e. This avoids discontinuities in the imposed boundary layer control and improves numerical stability.

For the actuation via travelling waves, a spatially and temporally varying wall-tangential actuation is prescribed

$$u_{StTW}(X, t) = f_{sm}(X)\, A_{StTW} \sin\left(\kappa_x X - \omega t\right), \tag{6.2}$$

where A_{StTW} is the forcing amplitude, κ_x the streamwise wave number, and ω the forcing frequency.

The total energy at the wall is reconstructed from the prescribed wall temperature and the kinetic energy contribution, which is corrected by the imposed velocity

$$E_w = e(T_w) + \frac{1}{2} u_{StTW}^2, \tag{6.3}$$

where $e(T_w)$ denotes the internal energy corresponding to the wall temperature T_w.

For the control with suction, a wall-normal velocity u_{US} is prescribed and imposed in the control region

$$u_{US}(X) = f_{sm}(X) A_{US} U_\infty, \tag{6.4}$$

with the normalized suction amplitude A_{US} and the reference freestream velocity U_∞. The imposed wall- normal velocity is projected onto the Cartesian coordinate system, ensuring that the forcing remains normal to the airfoil surface on the curvilinear grid.

The wall energy is calculated from the prescribed wall temperature and the corrected kinetic energy, resulting in the same equation as above.

"Time integration is performed using a third-order Runge-Kutta scheme with a maximum Courant-Friedrichs-Lewy number of $CFL = 1$. Flow quantities are averaged in both time and spanwise direction, over a minimum interval of $\Delta T = 40$, excluding an initial transient period that is determined individually for each case. The statistical convergence of the lift and drag was assessed a posteriori using the procedure proposed by [66]. For all configurations, the uncertainty in the estimated mean lift coefficient, measured by the ratio of its standard deviation to the mean value, does not exceed 0.3%, while the corresponding uncertainty for the drag coefficient remains below 0.8%. These values are denoted by σ_L and σ_D in Table 6.2." [FSP+26]

6.1.3 RANS Analysis of the V2C airfoil

"To complete the DNS results presented in the main manuscript, additional aerodynamic characteristics of the investigated airfoil V2C are obtained from steady RANS simulations. The computations are performed using the open-source solver SU2. A fully turbulent approach is employed using the Spalart-Allmaras turbulence model without transition modeling. The freestream conditions are identical to those used in the DNS, with a Reynolds number of $Re = 3 \times 10^5$ and a Mach number of $Ma = 0.7$. Simulations are conducted for angles of attack in the range $-1° \leq \alpha \leq 4°$.

The resulting lift and drag polars are shown in Figure 6.2. The lift coefficient exhibits a linear dependence on the angle of attack over the entire range considered. No change in the lift slope is observed, which is consistent with the assumption of a fully turbulent boundary layer in all cases. The lift coefficient obtained from the RANS simulation agrees well with the DNS results. Small differences are observed in the drag coefficient. These discrepancies are attributed to the low Reynolds number, where transition effects have a large influence on the drag. Since transition is not modeled in the present RANS setup, the drag is slightly underestimated compared to the DNS results.

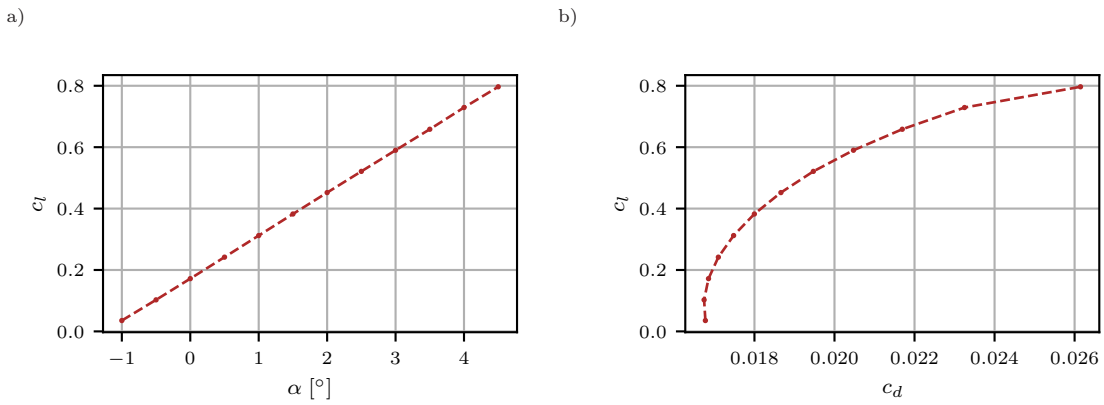


Figure 6.2: Polar plots for the V2C profile with a fully turbulent approach modeled via RANS simulations.

The surface pressure and skin-friction distributions are presented in Figure 6.3. At low angles of attack, no shock is observed. For higher angles of attack ($\alpha = 3°$ and $4°$), a shock appears on the upper surface. With increasing angle of attack, the shock strength increases, and its position shifts toward the leading edge.

The pressure distributions show a decrease in the pressure coefficient on the upper surface and an increase on the lower surface with increasing angle of attack, resulting in a larger pressure difference across the airfoil and, consequently, higher lift. The skin-friction distributions show only minor variations along most of the chord. Differences occur in the vicinity of the shock, where a local reduction in skin friction is observed. Downstream of the shock, a decrease in the friction coefficient is present for higher angles of attack." [FSP+26]

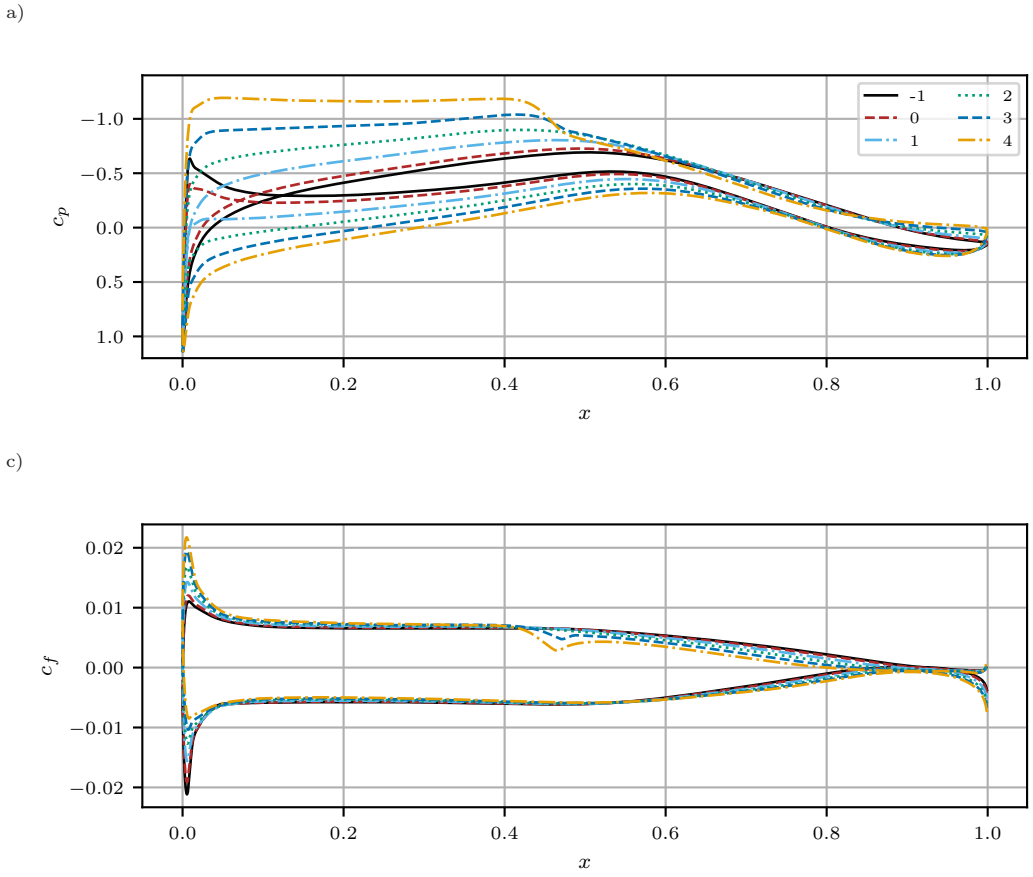


Figure 6.3: a) Pressure c_p and b) friction c_f coefficient distribution along the surface of the airfoil for RANS simulations with a fully turbulent approach.

6.1.4 Numerical Database

"The control method of StTW is defined by five parameters: the spatial wavenumber κ_x, the temporal frequency ω, the amplitude A_{StTW}, and the streamwise positions defining the start and end of the control region, X_b and X_e. In this study, the control region is fixed between $X_b = 0.2$ and $X_e = 0.78$ for both control methods [18, 59]. The upstream limit is chosen sufficiently upstream to allow the flow to transition to fully developed turbulence, while the downstream limit ensures that possible trailing edge components, such as, for example, flaps or ailerons, remain outside the control domain. The wall velocity is defined as in Equation 6.2.

[...]

Three representative StTW configurations are investigated: SW1 (streamwise wave), where the control has the shape of a steady wave; SW2, a configuration that showed a large reduction in the friction coefficient combined with a large increase in efficiency in previous studies [10]; and SW3,

a configuration with a reduced wave amplitude compared to the other ones. A baseline reference case (REF) without flow control is also computed. All simulations are conducted at an angle of attack of $\alpha = 4°$.

Table 6.1: Summary of the performed simulations with the corresponding control parameters. The travelling waves configurations are characterized by the amplitude A, and the spatial κ_x and temporal ω frequencies of the wave. The suction cases are characterized by the uniform suction velocity u_{us}.

Case ID	$\kappa_\mathbf{x}$	ω	$\mathbf{A_{StTW}}$	$\mathbf{u_{US}}$
REF	-	-	-	-
SW1	108.6	0	0.826	-
SW2	108.7	39.8	0.826	-
SW3	108.6	39.8	0.438	-
US1	-	-	-	0.00105
US2	-	-	-	0.0012

To compare the two control methods, each suction case was iteratively tuned such that its lift coefficient matched the corresponding StTW controlled case at a constant angle of attack of $\alpha = 4°$. The lift coefficient was selected as the matching parameter to test the hypothesis regarding whether the primary contributor to the improved efficiency is the reduction of the friction drag or the modification of the shock position. A RANS simulation with the open-source code SU2 (version 8.1.0) was conducted to estimate the initial suction velocity for the DNS setup. Note that the lift coefficient of the SW1 and SW3 cases is nearly identical, compare Table 6.2, thus, there is only one suction case (US1) for the comparison of these two cases. Consequently, the suction cases were adjusted to match the lift coefficients of the corresponding StTW configurations. The comparison between the control methods is therefore carried out at identical lift coefficients and angles of attack. The complete set of configurations is summarized in Table 6.1." [FSP+26]

6.2 Results

In this section of the manuscript, the effectiveness of the two investigated control methods is discussed. Therefore, the force coefficients as well as the changes in the distribution of the shear stress and pressure along the surface are shown. Further, the boundary layer properties are presented to identify the underlying mechanism of the effectiveness of the control methods.

6.2.1 Aerodynamic coefficients

The aerodynamic coefficients and their decomposition into friction and pressure contributions were introduced in Section 6.2.1. In the following, these quantities are used to evaluate and compare the aerodynamic performance of the different control strategies.

"The aerodynamic efficiency, defined as the lift-to-drag ratio $E = F_L/F_D$, characterizes the lift produced per unit drag. The position of the shock X_s is determined from the location of the maximum density gradient. To assess the effect of the control, some metrics are compared to the uncontrolled reference through the percent relative change

$$\Delta\Gamma = 100\frac{\Gamma - \Gamma_0}{\Gamma_0}, \tag{6.5}$$

where the value taken by a generic metric of interest in the controlled case is denoted by Γ, and Γ_0 is the corresponding reference value.

All parameters are averaged in both space and time, and the results are summarized in Table 6.2, where the lift c_L and drag coefficient c_D are shown with their percentage relative standard deviation σ.

For StTW, the control leads to a clear increase in the lift coefficient compared to the uncontrolled reference case for all cases. The drag coefficient increases slightly by 0.51% for the SW2 case and decreases for SW1 by 2.12%. Overall, the aerodynamic efficiency improves significantly in all cases, with gains of about 11% and a maximum of 12.76% in the SW1 case. These trends agree with the findings of [10], who also reported an overall improvement in the aerodynamic efficiency under the control of StTW.

Table 6.2: Aerodynamic coefficients for the simulated DNS cases for the reference case, as well as the cases with the control via StTW and suction. The lift c_L and drag coefficient c_D are shown with their percentage relative standard deviation σ as well as the two components of the drag ($c_{D,f}$ and $c_{D,p}$). The aerodynamic efficiency E and the position of the shock X_s are also shown. In the right part of the table, the relative change of the drag coefficient and the efficiency is shown with respect to the uncontrolled case.

Case ID	$\mathbf{c_L}$	$\sigma_\mathbf{L}$	$\mathbf{c_D}$	$\sigma_\mathbf{D}$	$\mathbf{c_{D,f}}$	$\mathbf{c_{D,p}}$	**E**	$\mathbf{X_s}$	$\mathbf{\Delta c_D}$	**ΔE**
REF	0.727	0.27	0.0259	0.46	0.0089	0.0170	28.1	0.467	-	-
SW1	0.803	0.26	0.0254	0.51	0.0074	0.0179	31.6	0.504	-2.12	12.76
SW2	0.818	0.25	0.0260	0.77	0.0078	0.0182	31.4	0.518	0.51	11.98
SW3	0.800	0.20	0.0256	0.39	0.0081	0.0175	31.2	0.506	-1.03	11.11
US1	0.808	0.10	0.0260	0.23	0.0091	0.0169	31.1	0.509	0.30	10.71
US2	0.819	0.10	0.0262	0.23	0.0092	0.0170	31.3	0.515	0.98	11.47

While the drag coefficient remains almost unchanged by the control, the share of the friction and pressure drag is modified by it. A decrease of the friction drag $c_{D,f}$ can be observed for the controlled cases via StTW, compensated by a corresponding increase in the pressure drag $c_{D,p}$. The control leads to a modified mean velocity gradient near the wall. More interestingly, the control leads to a shift of the shock toward the trailing edge, see increased X_s in Table 6.2 compared to the reference case.

The control via suction, tuned to yield the same lift coefficient as a respective StTW case, shows a surprisingly similar behavior to StTW despite the different working principle. Suction also increases the lift coefficient, while the changes in the drag coefficient are modest compared to the uncontrolled case. Overall, an increase in efficiency can be observed in the two investigated cases compared to the reference case. In contrast to the StTW, the control with suction modifies the flow differently. Suction removes low-momentum fluid from the boundary layer, which predictably increases the local wall shear stress and thus the friction drag, while at the same time, the pressure drag decreases. However, it simultaneously shifts the shock toward the trailing edge compared to the reference case. The effect of the control on the boundary layer quantities will be discussed in detail in Section 6.2.5. The lift increase and shock displacement observed under the control with suction are consistent with the mechanisms identified in the StTW cases. This further supports the hypothesis that the shift of the shock, rather than the reduction of the friction, is the key factor determining performance improvement.

Overall, the results of the averaged aerodynamic quantities indicate that the decisive factor for enhancing the aerodynamic efficiency is not the reduction of the wall-shear stress, but the ability of the control technique to alter the shock position. This hypothesis will be further discussed in the following sections.

In the following, the controlled cases are compared to the reference case as well as with each other. Therefore, the controlled cases with the same lift coefficient are grouped: (REF, SW1 and SW3, US1) and (REF, SW2, US2). Note that the lift coefficients for SW1 and SW3 are nearly identical, only one suction case for comparison is available. Since SW2 and US2 exhibit the largest efficiency gains, they are discussed in detail in the following." [FSP+26]

6.2.2 Pressure and friction coefficient distribution

"The distribution of the pressure and the friction coefficients, denoted as c_p and c_f, respectively, are shown in Figure 6.4 for the reference case (REF), the travelling waves case SW2, and the corresponding suction case US2. The coefficients are defined as follows

$$c_f(x) = \frac{\tau_w(x)}{\frac{1}{2}\rho_\infty U_\infty^2}, \tag{6.6}$$

$$c_p(x) = \frac{p_w(x) - p_\infty}{\frac{1}{2}\rho_\infty U_\infty^2}, \tag{6.7}$$

where $\tau_w(x)$ and $p_w(x)$ are the projected wall shear stress and pressure, respectively, and p_∞ is the freestream pressure.

The pressure distribution along the airfoil surface is shown in Figure 6.4a). The sudden decrease of c_p (suction peak) at the leading edge is followed by a plateau, which spans until the shock region and is characterized by a near-zero-pressure gradient for all three cases. For the controlled cases, the pressure coefficient is slightly lower in the plateau region, which is one reason for the increase in lift, which was discussed in Subsection 6.2.1. The shock region is indicated by a strong positive slope of the pressure coefficient. It can be clearly seen that the shock position for both controlled cases is shifted toward the trailing edge ($X_s = 0.515$) compared to the uncontrolled reference case ($X_s = 0.467$). The suction magnitude was tuned to match the lift coefficient of the StTW case, which not only led to the same c_L but also to the same magnitude of the shift of the shock toward the trailing edge. The shock characteristics differ slightly between the two controlled cases. The slope for the control via suction is larger and thus the shock sharper, while for the case with StTW control, the shock region spans wider. The data which are presented in the analysis are averaged results, thus also the position of the shock is also an averaged value. The shock is not fixed in space over time, but varies in a region of 1%c around the stated positions X_s above.

The friction coefficient c_f along the surface of the airfoil is shown in Figure 6.4b). For improved visualization of the distribution, the values on the lower surface are plotted with a negative sign. The transition at $X = 0.1$ is clearly visible by a peak of c_f in all configurations on both sides of the airfoil. Up until the transition, the friction coefficient is similar in all cases, the flow being laminar. In the region where the control is applied ($0.2 < x < 0.78$), the trends are different. While for the control via StTW a decrease in c_f is observed, as already expected from previous investigations, an increase in c_f can be observed for the suction case. The shock region is indicated by a drop in the friction coefficient. The decrease in the friction coefficient can already be observed upstream of the shock position. As the flow approaches the shock, it already experiences a strong adverse pressure gradient, see Figure 6.4a). This leads to a deceleration of the flow and thus a decrease in the wall shear stress as well as an increase in the boundary layer thickness (see Section 6.2.5). At the shock position, the minimum of the drop is reached. Downstream of the shock, the flow is subsonic, and the turbulence activities are enhanced due to the shock, leading to increased mixing and thus an increase in wall-shear stress. The drops of c_f in the controlled cases are placed further to the trailing edge, since the position of the shock is shifted toward the trailing edge. The shock

positions are indicated by the dashed lines (note that the shock positions of the controlled cases are at the same location and thus overlap). Throughout and immediately downstream of the shock, values of negative c_f, indicating local flow separation and reattachment, are observed for the SW2 case.

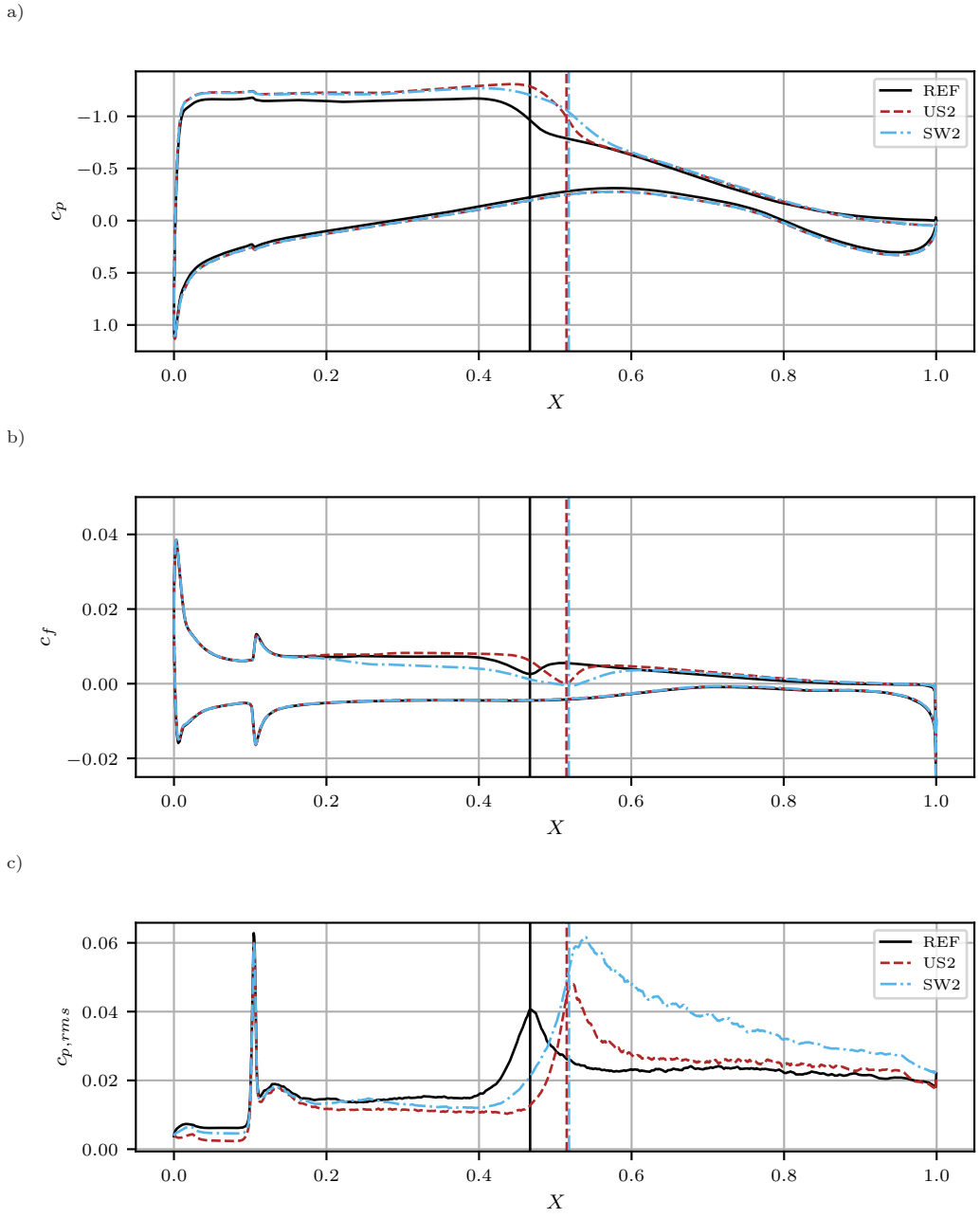


Figure 6.4: a) Pressure coefficient c_p, b) friction coefficient c_f, and c) rms of pressure coefficient $c_{p,rms}$ distribution along the surface of the airfoil. The vertical lines indicate the shock position.

Considering only the StTW results, one might infer that the nearly zero or slightly negative c_f values are the primary factor responsible for the observed drag reduction and efficiency improvement. However, in the suction-controlled cases, c_f is larger than in the reference case, becoming nearly zero but still positive only in a small region throughout the shock, suggesting the absence of mean

flow separation or recirculation bubbles. Therefore, the hypothesis that the total drag reduction and efficiency increase can only be achieved by the formation of a separation bubble characterized by low or negative c_f values is not supported. Instead, the suction cases demonstrate comparable overall drag reduction without the occurrence of a mean separation. Figure 6.4c) shows the rms values of the pressure coefficient, $c_{p,rms}$. In all configurations, two peaks can be observed. One at the position where the transition takes place, and a second one in the region of the shock. The peaks have the same order of magnitude. The peaks indicate the presence of acoustic noise and thus a change in the pressure coefficient.

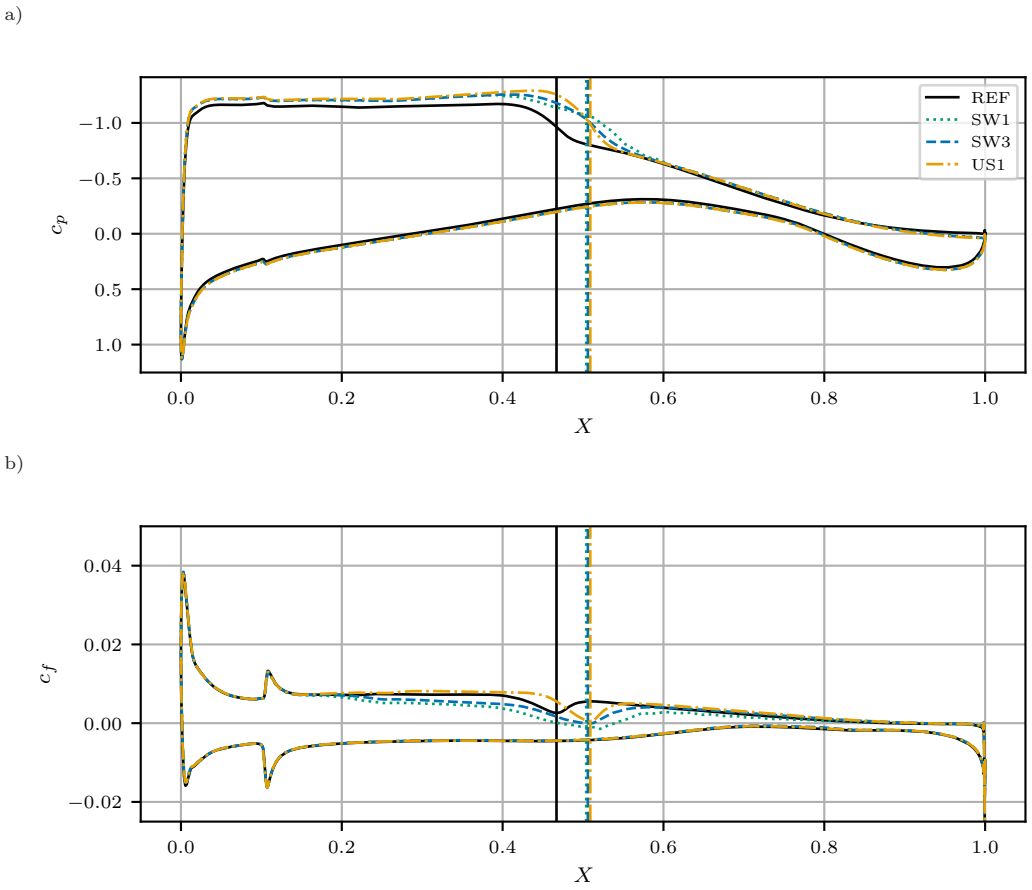


Figure 6.5: a) Pressure c_p and b) friction c_f coefficient distribution along the surface of the airfoil. The vertical lines indicate the shock position.

Figure 6.5 shows the other investigated controlled cases as well as the reference case. Overall, the results match the already observed results: the two investigated control methods lead to a shift of the shock toward the trailing edge, which is visible in the pressure as well as in the friction coefficient distribution. Furthermore, these results confirm that the shock is sharper for the suction control and wider for the control via StTW. One reason is the difference in the modifications of the boundary layer induced by the two control strategies. While uniform suction reduces both displacement and momentum thickness by a similar amount, StTW primarily reduces the momentum thickness while maintaining a comparatively larger overall boundary layer thickness. As a result, although the shock position correlates well with the reduction in momentum thickness and is therefore similar for both control methods, the thinner boundary layer in the suction case is less effective at smoothing the strong streamwise pressure gradients associated with the shock. In contrast, the thicker boundary layer in the StTW case leads to a more pronounced smearing of

these gradients, resulting in a wider shock structure. Furthermore, in the friction distribution, the separation of the flow for the control via StTW is observed, while the values for suction are close to zero but do not show a large region of negative values.

One reason for the wider shock in the StTW cases might be the presence of a separation bubble. The presence of a separation bubble makes the shock smoother by an upward shift of the shock penetration into the boundary layer. The separation probability and therefore the presence of a separation bubble are further discussed in Subsection 6.2.4. Further, in the cases of SW, less turbulence is present compared to the suction cases. In the suction case, the disturbances are pulled toward the wall and thus lead to a sharper shock.

Overall, in all investigated cases (compare Figure 6.4 and 6.5), the same trends can be observed. First, the applied control of suction and StTW shifts the shock toward the trailing edge, leading to an increase in the lift coefficient. The suction rate is tuned to achieve the same lift coefficient as the StTW case, the resulting shock position and overall aerodynamic efficiency are nearly identical. Second, this same effect on the shock position and lift coefficient occurs even though the two strategies act differently on the local friction: StTW reduces it, while suction increases it. Third, the effect on the pressure drag is opposite, StTW lead to an increase, while suction decreases the pressure drag. The observations indicate that the turbulent friction drag reduction is only indirectly responsible for the improvement in the aerodynamic efficiency. The dominant contribution instead arises from the shock displacement, which is likely linked to the thinner boundary layer produced by the applied control with respect to the reference case. This aspect will be further examined in Section 6.2.5." [FSP+26]

6.2.3 Pressure and friction drag

"This Section focuses on the distribution of the friction and pressure drag along the airfoil surface. Since the control is applied on the upper side, the effects on the pressure side are negligibly small, and the discussion of the results concentrates on the upper side.

The distribution of $c_{d,f}$ and $c_{d,p}$ for the reference case and the two controlled cases (SW2 and US2) is shown in Figures 6.6a) and b). The distribution of the friction drag on the upper side closely resembles that of the skin-friction coefficient c_f, see Figure 6.6a), as the airfoil surface is nearly flat (except near the leading edge) and therefore mostly parallel to the freestream. The difference in friction drag between the controlled and reference cases $\Delta c_{d,f}$ is shown in Figure 6.6c). Four distinct regions can be identified:

- Upstream of control ($X < 0.15$): differences between the cases are small and negligible.
- Pre-shock region ($0.15 < X < 0.4$): the two control strategies yield opposite effects. Suction increases $c_{d,f}$ compared to the reference case, while StTW reduces it.
- Shock region ($0.4 < X < 0.6$): a sharp drop in $c_{d,f}$ marks the shock. Because the shock is displaced downstream in the controlled cases, positive and negative peaks appear in $\Delta c_{d,f}$, reflecting the shifted location of the dip.
- Post-shock region ($X > 0.6$): both control methods exhibit a slight increase in $c_{d,f}$, relative to the reference. At the end of the control ($X = 0.78$), the boundary layer is thinner than in the respective reference case, thus, the friction will be locally higher than in the reference case [73].

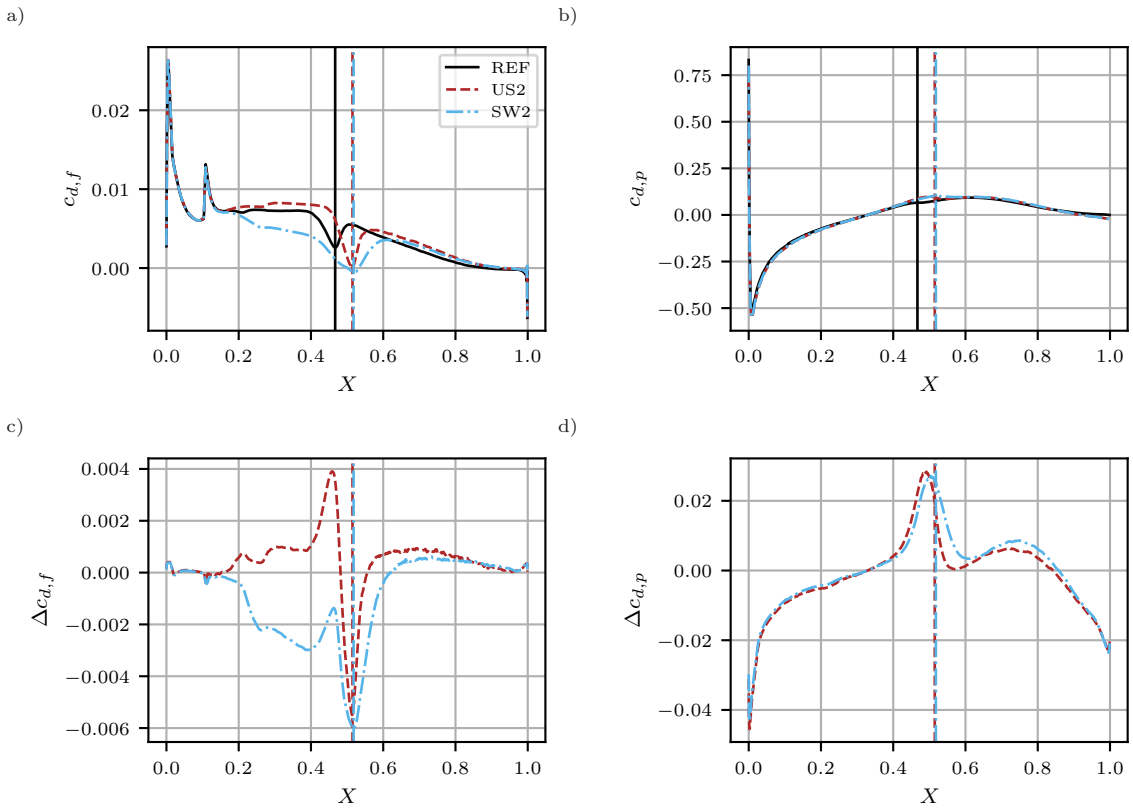


Figure 6.6: a) Friction and b) pressure drag distribution along the spanwise coordinate of the airfoil as well as the differences between the controlled cases and the reference case for the friction and pressure drag (c) and d)).

The changes in the pressure distribution $c_{d,p}$ seem small, but since its absolute magnitude is larger than that of the friction drag, even small variations significantly influence the total drag. The distribution of the pressure drag $c_{d,p}$ is shown in Figure 6.6b), which follows a similar trend across all cases: a sharp drop at the leading edge followed by a recovery, and slightly positive values over the control region. Differences emerge near the shock, as seen in Figure 6.6d), which presents the distribution of $\Delta c_{d,p}$. Both control methods increase the pressure drag in this region due to the shock being shifted downstream and intensified. The peak of $\Delta c_{d,p}$ is somewhat smaller in height but broader in width for the SW2 case than the US2 case, suggesting that the shock is slightly weaker in SW2. This observation is consistent with the slope changes discussed earlier in Subsection 6.2.2." [FSP+26]

6.2.4 Instantaneous Velocity Field

"The instantaneous velocity profiles of the tangential velocity in the very vicinity of the wall (distance from the wall $1.1 \cdot 10^{-3}c$) are shown in Figure 6.7 for the reference case (a), SW2 (b), and US2 (c).

In all three cases, the flow remains laminar up to the tripping location at $X = 0.1$. In the REF case (see Figure 6.7 a), streaks of alternating high- and low-speed fluid form as the flow transitions to turbulent flow. These streaks are convected downstream and slow down in the vicinity of the shock, where a clear velocity drop is observed. While the time- and space-averaged skin-friction coefficient c_f remains positive in this case, a few small patches of negative tangential velocity appear in the instantaneous field, indicating the presence of local and instantaneous backflow events. The

probability of a negative streamwise velocity ϕ_{nv} along X is shown in Figure 6.8. The probability for a separation in the reference case is close to zero in the region of the shock. Downstream of the shock, the streaks persist but at lower overall velocity levels compared to upstream. Near the trailing edge, a large region of negative velocity develops, indicating flow separation. This agrees with the c_f distribution, which is negative close to the trailing edge. It can also be seen in Figure 6.8, where a negative tangential velocity near the trailing edge is present at almost all time steps. The trailing edge separation is due to the geometry of the V2C airfoil, with a fairly steep slope of the upper side near the trailing edge.

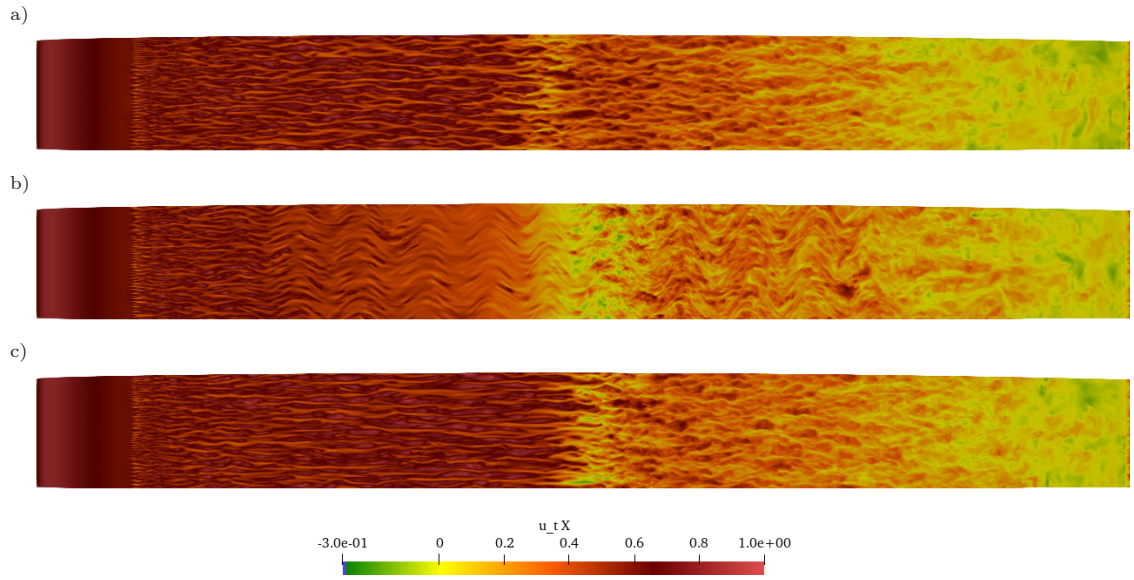


Figure 6.7: Instantaneous velocity profiles of the velocity component tangential to the wall on the upper side of the airfoil. The three cases, a) REF, b) SW2, and c) US2, are shown.

The velocity profile for the control via streamwise travelling waves is quite different. The streaks of high- and low-speed fluid, which are produced as the flow becomes turbulent after transition, can also be observed in this case. In the control region, the effect of StTW is clearly visible in the velocity field, where it induces a wave-like spanwise modulation accompanied by a weakening of the streaks. As the flow approaches the shock, the streaks slow down significantly thanks to the drag-reducing effect of the waves (orange instead of dark red streaks), and the shock itself is shifted downstream compared to the reference case. At the shock position, local regions of negative velocity indicate flow separation, consistent with the negative c_f values discussed previously. The separation probability for the travelling waves cases is between 30% for SW2 and up to 60% for SW1. However, downstream of the shock, the flow reattaches before separating again near the trailing edge, similar to the REF case.

The US2 case is similar to the REF case. The shock is shifted downstream, whereby, in this case, there is no slowing down of the flow since suction removes the low-momentum fluid. Although the averaged c_f remains positive, small regions of negative velocity are observed in the shock regions, suggesting the presence of instantaneous backflow events even in the absence of mean separation. The separation probability for the cases with suction control in the region of the shock is approximately 10%. Overall, the control delays flow separation at the trailing edge relative to the reference case. Further, a mean separation is not strictly needed for efficiency gain, as the suction cases reach similar performance without extended separation." [FSP+26]

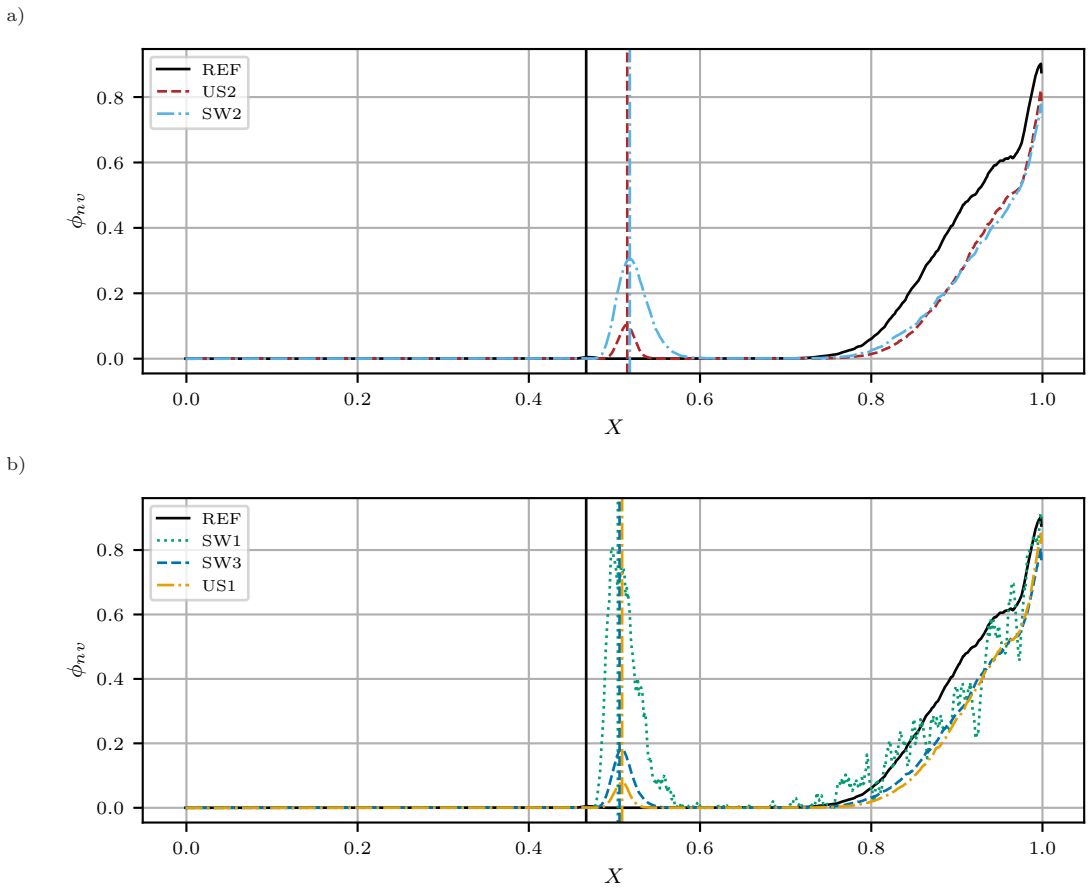


Figure 6.8: Separation probability ϕ_{nv} of the investigated control methods and the reference case. The vertical lines mark the shock positions.

6.2.5 Boundary Layer Properties

"Figure 6.9 shows the evolution of boundary layer parameters: the displacement thickness δ^*, the momentum thickness θ, and the shape factor H together with the pressure gradient $\partial c_p/\partial x$ along the surface of the airfoil. For a better interpretation of the data, the Reynolds number based on the momentum thickness Re_θ is plotted in Figure 6.9c).

The boundary layer thicknesses are computed as follows [81]

$$\delta^* = \int_0^\infty \left(1 - \frac{\bar{\rho}\tilde{u}}{\rho_e U_e}\right) d\eta, \tag{6.8}$$

$$\theta = \int_0^\infty \left(1 - \frac{\tilde{u}}{U_e}\right) \frac{\bar{\rho}\tilde{u}}{\rho_e U_e} d\eta, \tag{6.9}$$

$$H = \frac{\delta^*}{\theta}, \tag{6.10}$$

where $(\bar{})$ and $(\tilde{})$ denote the Reynolds and Favre averaged quantities, respectively. The edge of the boundary layer is defined as the location where the tangential velocity reaches 99% of the maximum value, denoted by the subscript e. It is noted that in strongly non-equilibrium flows the δ_{99} criterion may become ambiguous [30]. However, in the present configurations, the separation region is limited, and the δ_{99} criterion remains a consistent measure of the boundary layer thickness.

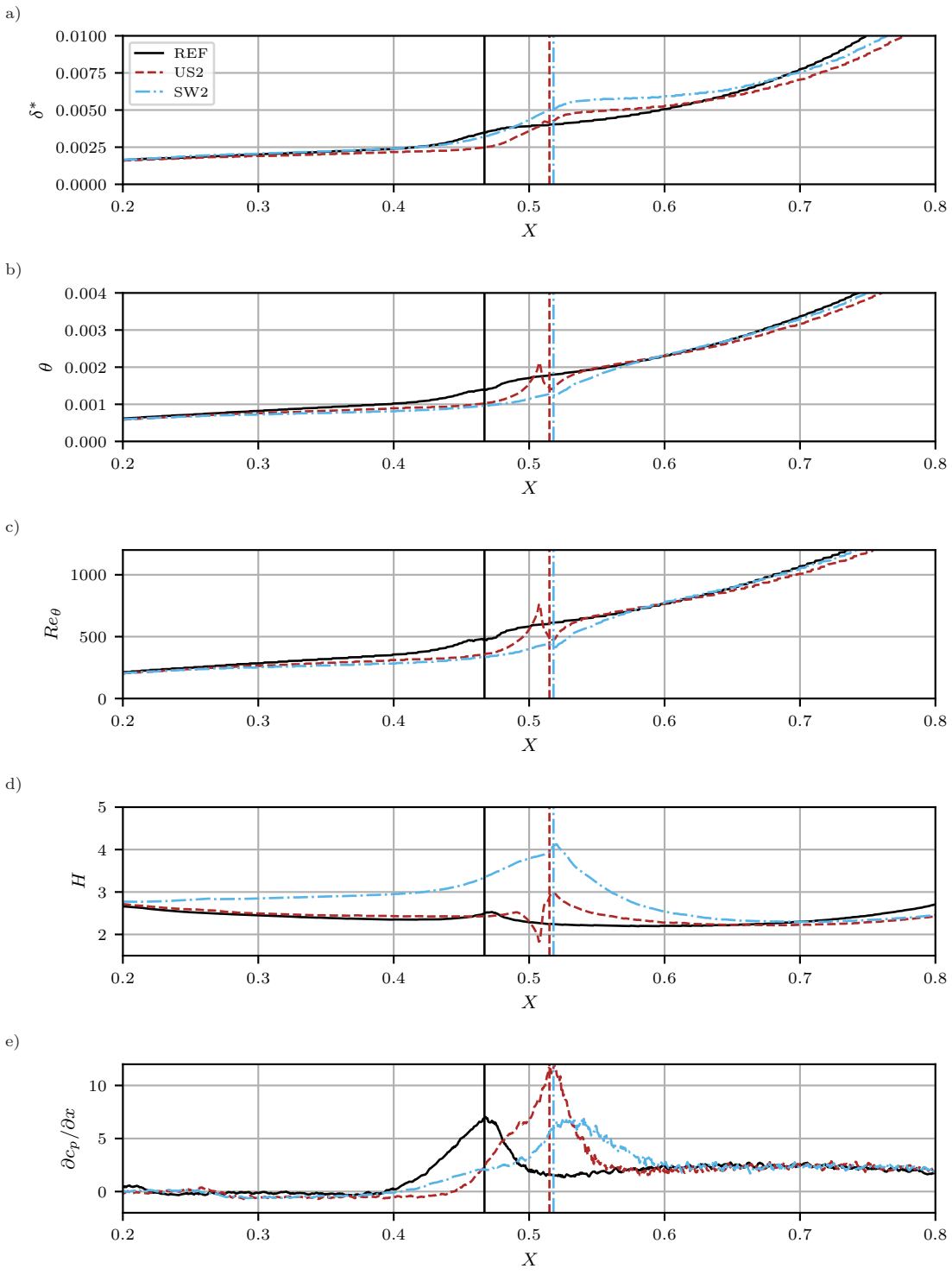


Figure 6.9: Integral Boundary layer quantities and the pressure gradient along the upper side in the region of the control for the reference case, as well as the SW2 and US2 cases.

For all three cases shown in Figure 6.9a), the displacement thickness grows gradually. Up to the shock region ($X < 0.4$), the development of the displacement thickness for the REF and the SW2 cases is nearly identical. This can also be observed for the cases SW1 and SW3 in Figure 6.10. Thus, the control of suction and StTW does not influence the development of the displacement thickness upstream of the shock. The suction-controlled cases exhibit slightly lower displacement

thickness compared to both the StTW and reference cases, which can be explained by the removal of the low-momentum fluid.

At the shock location, the external flow changes noticeably. The edge velocity U_e decreases while the pressure and temperature increase abruptly. Since the boundary layer parameters depend on these external quantities, corresponding variations in the thicknesses are observed. Within the shock region, δ^* increases for all cases, with the rise shifted downstream in the controlled configurations owing to the delayed shock position. Immediately downstream of the shock, the displacement thickness is largest for the SW2 case and smallest for the reference case. Both controlled cases show a similar post-shock trend. First, a moderate growth immediately after the shock, followed by a steeper increase toward the end of the control region. The uncontrolled case, by contrast, exhibits a gradual and continuous growth eventually surpassing the controlled configuration so that δ^* becomes largest at the end of the control region.

The airfoil curvature within the control region is limited, and the surface is relatively flat. Therefore, the reduction in the wall-shear stress observed in Figure 6.4 for the SW2 case corresponds directly to a weaker growth of the momentum thickness. This behavior is confirmed in Figure 6.9b). Both controlled cases show a similar trend. Before the shock, the momentum thickness is lower than in the uncontrolled case. For the control via suction, the momentum thickness is reduced despite higher c_f values, since suction removes low-momentum fluid near the wall, effectively thinning the boundary layer. For the travelling waves case, a smaller θ is consistent with the lower c_f values. Interestingly, the momentum thickness of the corresponding StTW and suction pairs is very similar sufficiently before the shock, even though this has not been imposed explicitly. The fact that this similarity results automatically for those cases featuring similar c_L may suggest that the control-induced modification of the momentum thickness may relate to the increase in c_L and shift of the shock. Across all configurations, the shock induces an increase in the growth rate of the momentum thickness. In the downstream part of the control region, both controlled cases feature slightly smaller momentum thicknesses than the reference case.

The shape factor H remains nearly constant in the reference case but increases significantly in the controlled cases. The increase is moderate for suction control, while the SW2 case exhibits a pronounced peak. A larger H indicates a boundary layer more prone to separation, consistent with the flow separation identified for the SW cases in the c_f distributions, the instantaneous velocity profiles, and the separation probability. The shape factor of a zero-pressure gradient flat plate is in the range of $H \approx 1.6 - 1.7$ [67] for Reynolds numbers based on the momentum thickness of $Re_\theta \approx 300$. The H factor decreases slightly with increasing Reynolds number for the simplified geometries.

For all cases, an adverse pressure gradient is present in the shock region, see Figure 6.9d), leading to flow deceleration. In the SW2 case, the adverse pressure gradient starts well before the shock, causing earlier flow deceleration. This is consistent with the instantaneous velocity profiles. The pressure gradient for the SW1 configuration (see Figure 6.10d)) shows a sinusoidal shape, reflecting the steady modulated wave of the applied control. The control via StTW accelerates and decelerates the near-wall flow at some positions along the steady wave. In the boundary layer, this results in a periodic pressure gradient. Since for the streamwise flow, it is equal in which direction the spanwise velocity is directed, the resulting wavelength of the pressure gradient is half the wavelength of the applied steady wave.

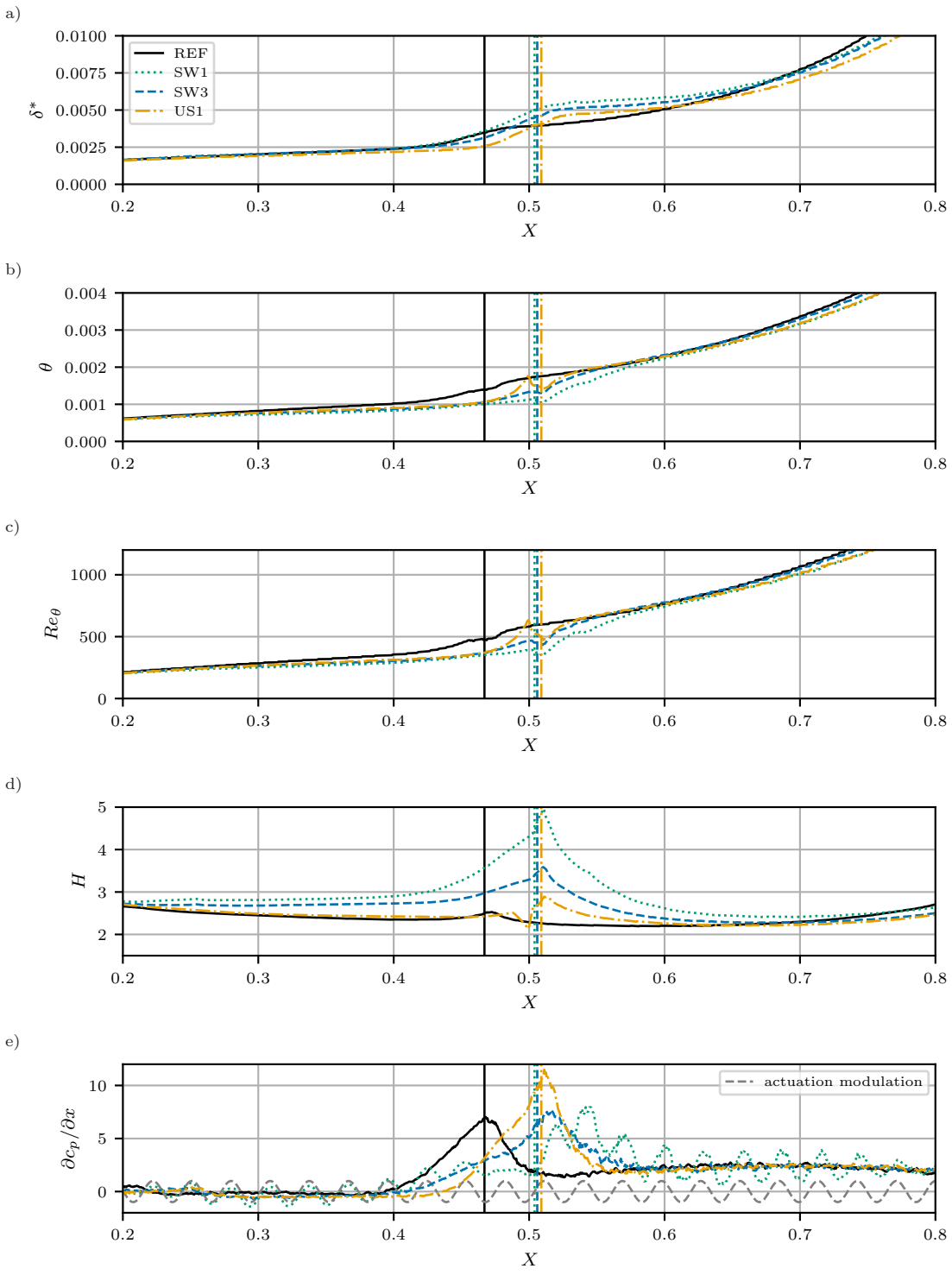


Figure 6.10: Integral Boundary layer quantities and the pressure gradient along the upper side in the region of the control for the reference case, as well as the SW1 and SW3; and US1 cases. The modulation of the wall for case SW3 is added in d), matching the modulation of the pressure gradient variation.

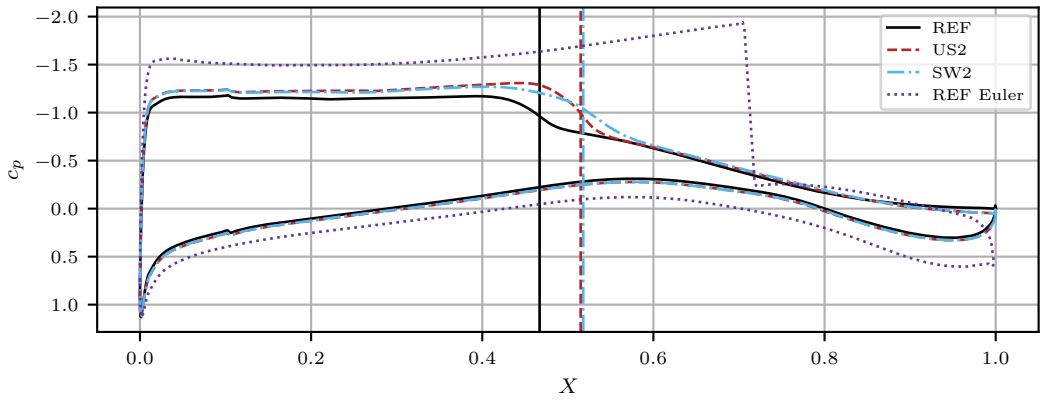


Figure 6.11: Pressure distribution of the Euler solution compared to the DNS results.

The analysis of the boundary layer parameters indicates that, upstream of the shock, the momentum thickness is reduced for both control methods. Furthermore, the momentum thickness exhibits nearly identical values for the two cases. This observation suggests that a reduced momentum thickness upstream of the shock is a contributing factor to the observed improvement in control efficiency.

The analysis of the boundary layer parameters, as well as the distributions of the aerodynamic coefficients, showed that the main contributors to the efficiency increase are the shock displacement toward the trailing edge and the reduced momentum thickness. The Euler solution, representing the inviscid limit with no boundary layer, exhibits the maximum possible shock shift downstream, illustrating the theoretical limit of the achievable control effect. Figure 6.11 compares the pressure distribution of the present DNS results and the inviscid Euler solution, computed using the open-source solver SU2. It is expected that the positive effect of the control to shift the shock downstream would reduce with increasing Reynolds number, since the boundary layer would become thinner compared to the chord, but the conditions are still far from a vanishing boundary layer thickness, and there is the possibility that these control strategies still yield positive effects at large, albeit not infinite, Reynolds numbers.

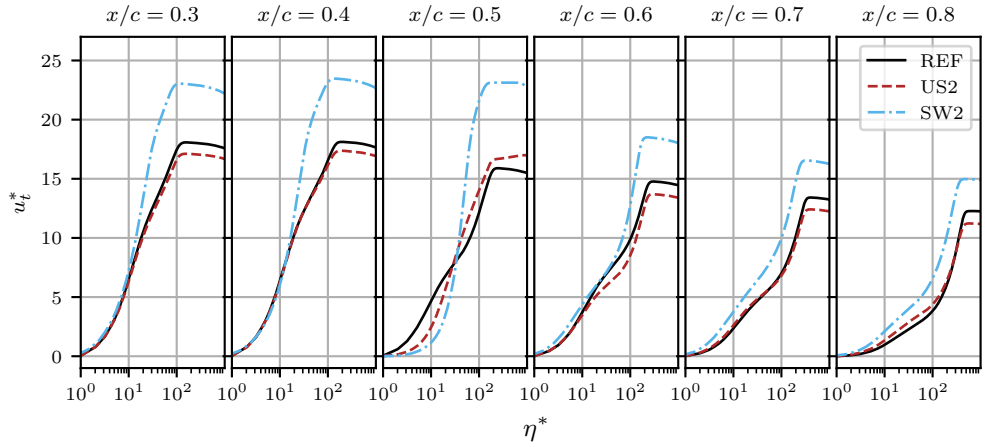


Figure 6.12: Wall-normal profiles of the mean streamwise velocity scaled in viscous units at different positions along the upper side of the airfoil. The corresponding viscous units are computed at $X = 0.35$.

Figure 6.12 presents the wall-normal profiles of the mean streamwise velocity scaled in viscous units, computed at $X = 0.35$. The first two plots ($X = 0.3$ and 0.4) illustrate the upstream region of the

shock, where the control already exhibits mild influence while the shock remains downstream. The control does not significantly affect the viscous sublayer before the shock. For StTW, the velocity profile is steeper, indicating a higher tangential velocity component. Downstream of the shock, the profiles flatten due to the flow deceleration, observed in $X = 0.5$ for the reference case and $X = 0.6$ for the controlled case." [FSP+26]

6.2.6 Reynolds stresses

"The tangential Reynolds stress, scaled in actual viscous units, at six different locations along the upper side is shown in Figure 6.13. The stress peaks shift toward higher η^* values when evaluating the tangential Reynolds stresses further downstream. The position of the peak for $X \leq 0.4$ is similar throughout all cases, with a clear reduction in the SW2 case, indicating turbulent suppression. After $X = 0.5$, the effect of the adverse pressure gradient can be observed, which moves the peak outwards. The effect of the shock is more visible in the controlled cases, where higher amplitudes in the $\overline{u'v'}^*$ peaks and a larger shift can be observed. The controlled case SW2 displays the highest peak, this could be due to the presence of the separation bubble, whose shear layers can additionally trigger turbulence." [FSP+26]

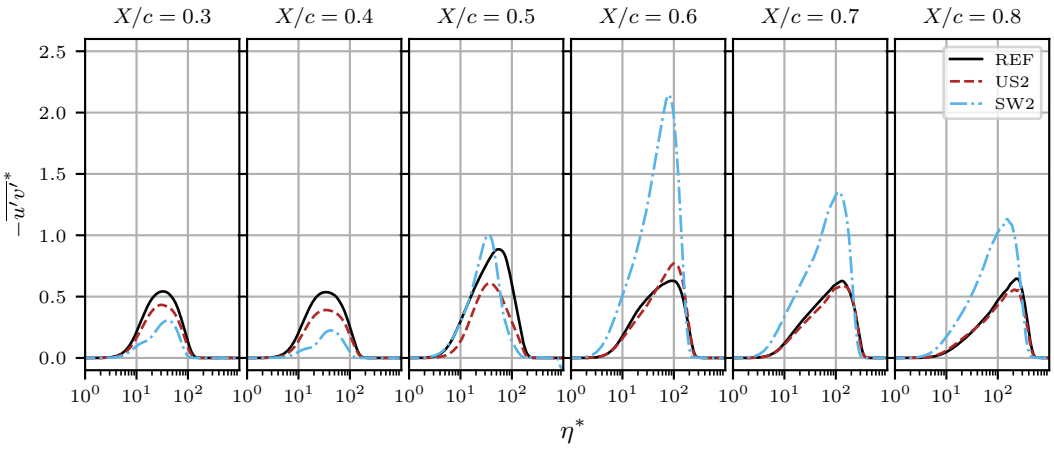


Figure 6.13: Tangential turbulent stress scaled in viscous units at different positions along the upper side of the airfoil. The corresponding viscous units are computed at $X = 0.35$.

6.3 Power Consumption

"Active flow control methods require energy to operate. Quantifying the amount of energy employed for operation is essential to assessing the viability of the control. Although both control strategies investigated in the present work, StTW and US, influence the near-wall flow characteristics, they do so through fundamentally different physical processes, which is also reflected in the corresponding power requirements. The following subsections summarize the idealized formulations used to quantify the energy input associated with each actuation type." [FSP+26]

6.3.1 Power estimation for StTW

"In a mechanical implementation of StTW, an actuator performs work against the viscous stresses generated by the imposed spanwise wall motion. The power required by the control would be dominated by the mechanical inertia of the actuating system, as has been the case for most laboratory implementations so far [6, 24]. Since the estimation of power consumption strongly depends on the details of the implementation, it is common practice to assume an ideal (lossless and massless) device, so the power is transmitted to the fluid without mechanical losses. The power consumption can thus be derived from the compressible energy equation as the work performed by the spanwise wall shear per unit time:

$$P_{StTW} = \int_{A_{wall}} w_\xi \, \mu \left. \frac{\partial w}{\partial \eta} \right|_\xi \, \mathrm{d}A, \tag{6.11}$$

where w_ξ is the spanwise wall velocity and the area A_{wall}, which corresponds to the surface area where the control is applied.

6.3.2 Power estimation for US

The power required for suction is governed primarily by the work needed to draw the fluid from the boundary layer and compress it to discharge conditions. To derive the expression, the flow is treated as an ideal gas undergoing isentropic compression within an idealized pump. Under these assumptions, viscous stresses may be neglected. Using the compressible energy equation and assuming that the mass flow rate through the control area and the mass flow rate at outflow conditions are equal

$$\dot{m}_{us} = \rho_{us} \, u_{us} \, l_{us} = \rho_{out} \, u_{out} \, l_{out} = \dot{m}_{out} = \dot{m}, \tag{6.12}$$

where the subscript *us* denotes the values at the wall across the boundary layer control region and *out* the discharge conditions. The ideal power required for suction becomes

$$P_{pump} = \int_{A_{wall}} \left\{ \dot{m} \, R_{id} \, T_{us} \, \frac{\gamma}{\gamma - 1} \left[\left(\frac{p_{out}}{p_{us}} \right)^{\frac{\gamma-1}{\gamma}} - 1 \right] + \frac{1}{2} \, \dot{m} u_{us}^2 \left[\left(\frac{u_{out}}{u_{us}} \right)^2 - 1 \right] \right\} \, \mathrm{d}A, \tag{6.13}$$

where T is the temperature, R the ideal gas constant and γ the ratio of specific heats. For this formulation, the pressure environment in which the pump operates needs to be considered. The extracted fluid is collected in a supply chamber at the pressure level $p_{chamber}$. To ensure continuous inflow through the suction area, the pressure in the chamber must be lower than the minimum pressure along the suction surface

$$p_{chamber} = min(p_{us}) - \Delta p, \tag{6.14}$$

where Δp accounts for the flow resistance through the porous skin and the ducts.

The fluid is expelled as a jet, assuming to recover the same total pressure as the free stream and exits with a velocity of U_∞. The associated thrust generated by the jet is

$$P_{thrust} = \dot{m} \, u_{out}. \tag{6.15}$$

Subtracting this contribution from the ideal pump power yields the net power input required for the suction-based control

$$P_{us} = P_{pump} - P_{thrust}. \tag{6.16}$$

" [FSP+26]

6.3.3 Net Power Consumption

"A direct comparison of the power requirements associated with spanwise travelling waves and wall-normal suction is not straightforward, as the underlying formulations rely on different physical assumptions and levels of idealization. For the StTW case, the power estimate reflects an ideal actuator that transfers energy without losses and performs work only against the viscous stresses generated by the imposed wall motion. This represents a highly optimistic scenario.

In contrast, the suction power model incorporates a more realistic representation of the pumping process. The fluid extracted from the boundary layer is assumed to enter a supply chamber maintained at a constant pressure level. This assumption inherently reflects non-ideal operating conditions, particularly in configurations where the surface pressure exhibits substantial spatial variations, as in transonic flow where a shock is present. In such scenarios, the pump must overcome large pressure differences, potentially increasing the power demand. However, for the present comparison, the pump efficiency is set to $\eta_p = 1$, and the additional pressure drop accounting for losses due to the porous surface and the ducts is neglected ($\Delta p = 0$). These assumptions yield the most optimistic estimate permitted by the suction power formulation and ensure a more equitable comparison with the idealized StTW power evaluation.

The calculated control power is shown in Table 6.3. Although the absolute values depend on the specific assumptions underlying the power calculation, the results indicate that both control strategies require power inputs of the same order of magnitude. Nevertheless, the power associated with case US2 is approximately half that of case SW2, even though the estimate for StTW is based on more idealized assumptions.

It should be noted that these power estimates are optimistic and are intended primarily for a qualitative comparison rather than a definitive assessment of energetic efficiency. No systematic optimization of the control parameters has been performed. In the travelling wave cases, a considerable portion of the input power is irreversibly dissipated in the near-wall region, and only a small fraction of the work directly contributes to modifying the shear stress. Additionally, the relatively large amplitudes used in the travelling wave case ($A_{TW2} = 0.826$ and $A_{TW3} = 0.438$) imply rapid wall motion, which further increases the energetic costs. In contrast, the suction-based control operates on comparatively small extraction velocities ($u_{us} \approx 0.001$), resulting in a lower power consumption.

Table 6.3: Calculation of the power consumption for the two control strategies.

Case ID	$\mathbf{P_{StTW}} \cdot 10^3$	$\mathbf{P_{pump}} \cdot 10^3$	$\mathbf{P_{thrust}} \cdot 10^3$	$\mathbf{P_{us}} \cdot 10^3$
SW1	1.498	-	-	-
SW2	1.939	-	-	-
SW3	0.539	-	-	-
US1	-	1.734	0.973	0.761
US2	-	1.989	1.105	0.885

Overall, both control strategies achieve comparable improvements in aerodynamic efficiency and promote a downstream displacement of the shock. However, the power consumption associated with suction remains substantially lower than that of the spanwise travelling waves, even under the non-ideal assumptions." [FSP+26]

6.4 Concluding Discussions

The discussed study investigated the aerodynamic performance and flow physics of the transonic airfoil V2C with the two active flow control methods of streamwise travelling waves and wall-normal homogeneous suction, based on direct numerical simulations. Both methods were found to improve the overall aerodynamic efficiency compared to the uncontrolled baseline, despite fundamentally different mechanisms.

While the lift coefficient increased in all controlled cases, the changes in total drag were relatively small. A detailed decomposition revealed opposite trends in the individual drag contributions: StTW primarily reduces skin-friction drag but slightly increases pressure drag, whereas suction produced the inverse behavior. Nevertheless, both strategies resulted in comparable overall efficiency improvements, indicating that the redistribution of the drag components is less relevant than the global flow response.

A key outcome of the study is the consistent downstream shift of the shock for both control strategies. This shock displacement correlates strongly with the increase in lift and aerodynamic efficiency and appears to be the dominant mechanism behind the performance gain. Suction cases adjusted to achieve lift coefficients comparable to the StTW cases exhibited similar shock positions and efficiency improvements. The results therefore suggest that the main driver of the aerodynamic benefit is not the direct reduction of wall-shear stress, but rather the modification of the shock-boundary-layer interaction.

Both control strategies achieve this effect through a reduction in momentum thickness upstream of the shock, albeit via different physical mechanisms. StTW weakens the near-wall turbulence and reduces skin friction, while suction directly removes low-momentum fluid from the boundary layer. Cases with similar lift coefficients and shock positions consistently exhibited comparable momentum thickness levels. This indicates that momentum thickness is a key parameter linking the applied control to the resulting aerodynamic performance.

The comparison to the inviscid solutions shows that further shock displacement is theoretically possible, but also highlights that the boundary layer thickness remains significant even at higher Reynolds numbers. Consequently, while the observed trends are expected to persist qualitatively, the magnitude of the efficiency gains is likely to decrease under more realistic flight conditions.

From an energetic perspective, both control strategies operate within the same order of magnitude, although StTW require roughly twice the power of suction under the present assumptions. Despite these differences, both methods achieve similar aerodynamic benefits, suggesting that the efficiency gain is primarily governed by the flow physics rather than the energetic efficiency of the actuation itself.

Overall, both control methods improve aerodynamic performance by acting on the upstream boundary layer and shifting the shock downstream. However, the study is limited by the relatively low Reynolds number, which likely amplifies the observed effects. Future work should therefore focus on higher Reynolds numbers and systematic optimization of the control parameters, potentially

in combination with geometric design changes, to assess the practical relevance of the observed mechanism under more realistic conditions.

7 Final Concluding Discussion

The objective of this thesis was to investigate how active flow control can improve aerodynamic efficiency in compressible and transonic flows. Particular emphasis was placed on understanding the interaction between boundary layer manipulations, shock-wave behavior, and the resulting balance between friction and pressure drag. Two research questions were formulated. The first addressed the performance of wall-normal homogeneous blowing and suction under compressible and transonic conditions. It further investigated the influence of shock boundary layer interactions on the aerodynamic efficiency. The second focused on identifying the dominant physical mechanism responsible for the aerodynamic benefits of the active flow control methods of wall-normal suction and streamwise travelling waves of spanwise velocity and on determining how these mechanisms differ between the two approaches.

The results presented in Chapters 5 and 6 demonstrate that active flow control can improve aerodynamic efficiency in transonic airfoil flows. The observed improvements are primarily associated with modifications of the boundary layer and the shock characteristics rather than with changes in local-skin friction drag. The control methods alter the boundary layer in the vicinity of the shock, which affects the shock position, the pressure distribution, and the aerodynamic force balance. Consequently, the success of a control strategy in transonic flows depends primarily on its influence on the shock boundary layer interaction rather than on its direct effect on wall-shear stress.

The first research question examined the performance of wall-normal blowing and suction under compressible and transonic conditions and the extent to which shock boundary layer interactions influence the aerodynamic efficiency. The results of the parametric study show that the aerodynamic impact of wall-normal mass flow control depends strongly on the flow regime, the control configuration, and the control magnitude.

In the compressible subsonic regime, only a limited number of configurations produced an increase in aerodynamic efficiency. Positive effects were observed mainly for suction at high lift coefficients and low control magnitudes. These findings are consistent with previous studies [5, 18] and highlight that aerodynamic efficiency can be improved even when the control method does not reduce local wall-shear stress.

In the transonic regime, the behavior changes fundamentally due to the presence of a shock wave. Under these conditions, wall-normal mass flow control affects not only the local wall shear stress and boundary layer thickness but also the position of the shock and the pressure distribution over the airfoil. Among the investigated configurations, suction applied on the suction side proved to be the most promising approach. Suction caused a downstream displacement of the shock toward the trailing edge and increased the lift coefficient. For low control magnitudes, this was accompanied by a reduction in inclusive drag, resulting in an increase in aerodynamic efficiency even when the energetic cost of the actuation was taken into account using conservative assumptions.

In contrast, none of the investigated blowing configurations produced a net increase in aerodynamic efficiency once the inclusive drag was considered. Although blowing reduced local skin friction drag, this benefit was offset by unfavorable changes in pressure drag. An important finding of the present

study was that local friction drag reduction alone is not a sufficient indicator of aerodynamic improvement in transonic airfoil flows. When a shock wave is present, pressure effects become equally important as skin-friction effects and can even dominate the overall aerodynamic response.

The results further show that the effect of suction depends sensitively on the control magnitude. Stronger suction reduces the boundary layer thickness more effectively and shifts the shock further downstream. At the same time, however, it increases friction drag due to steeper velocity gradients at the wall and may also strengthen the shock, leading to increased pressure drag. Consequently, only low-magnitude suction produced a net aerodynamic benefit. This indicates the existence of an optimal control range in which the drag reduction achieved through the shock displacement is greater than the associated drag penalties.

The investigation of different control locations showed that, within the considered parameter space, the overall control configuration and the total mass flow involved in the actuation are more influential than the precise positioning of a shorter control region relative to the shock. Larger control regions generally produced stronger aerodynamic effects because they involved greater momentum extraction or injection. Nevertheless, this observation should not be generalized beyond the investigated configuration, as different geometries or non-uniform control distributions may exhibit a stronger sensitivity to control placement.

The first research question can therefore be answered by stating that wall-normal blowing and suction can significantly influence aerodynamic performance in compressible and transonic flows, but their effectiveness is governed primarily by their impact on the shock boundary layer interaction. In the investigated parameter range, only suction on the suction side produced a positive aerodynamic effect, and this occurred mainly at low control magnitudes under transonic conditions. The underlying mechanism is the modification of the boundary layer that leads to a downstream displacement of the shock and a corresponding improvement in the lift-to-drag ratio.

The second research question addressed the dominant physical mechanism responsible for the aerodynamic benefits of wall-normal suction and streamwise travelling waves of spanwise velocity and examined the extent to which these mechanisms differ between the two approaches.

The comparative study showed that, despite acting through fundamentally different local mechanisms, both control strategies produce remarkably similar global aerodynamic effects. In both cases, the lift coefficient increased, the shock moved downstream, and the aerodynamic efficiency improved relative to the uncontrolled reference case.

A decomposition of the drag contributions showed that the two methods affect local drag components in opposite ways. Streamwise travelling waves reduced friction drag while slightly increasing pressure drag, whereas suction increased friction drag while reducing pressure drag. Despite these contrasting effects, both methods produced comparable gains in aerodynamic efficiency. This demonstrates that reducing skin friction alone cannot explain the observed aerodynamic improvement. If friction reduction were the dominant mechanism, suction would not have yielded such favorable results.

The detailed boundary layer analysis provides a clear explanation for this observation. Both control methods reduce the momentum thickness upstream of the shock, although they achieve this through different physical processes. Travelling waves modify near-wall turbulence and alter boundary layer development through drag reduction mechanisms, while suction directly removes low-momentum fluid from the boundary layer. Despite these differences, both approaches generate a similar boundary layer state in the region relevant to the shock boundary layer interaction.

The most informative cases are those with similar lift coefficients and shock positions. These cases also show similar momentum-thickness distributions upstream of the shock despite being controlled by different methods. This strongly suggests that momentum thickness is the key parameter linking local boundary layer modifications to the global aerodynamic response. These results therefore indicate that the dominant mechanism responsible for improved aerodynamic efficiency is the reduction of momentum thickness upstream of the shock, which promotes a downstream displacement of the shock and thereby modifies the balance between lift and drag in a favorable manner.

The results further indicate that the aerodynamic benefits associated with shock displacement are limited and should not be assumed to increase linearly with the downstream shock movement. Excessive downstream movement of the shock may increase shock strength, promote local separation, and increase pressure drag, thereby reducing or even reversing the aerodynamic gain. Evidence of such behavior was observed in both studies. Higher suction magnitudes led to increasing drag despite further shock displacement, while the travelling wave cases exhibited indications of separations and reattachment downstream of the shock. These findings suggest that an optimal shock position exists and that successful control requires balancing shock displacement, shock strength, drag, and lift rather than maximizing shock displacement alone.

The second research question can therefore be answered by stating that the dominant physical mechanism responsible for the aerodynamic benefits of wall-normal suction and streamwise travelling waves is the control-induced reduction of momentum thickness upstream of the shock. This boundary layer modification causes a downstream displacement of the shock and thereby improves the aerodynamic force balance. The difference between the two methods lies primarily in the local mechanism by which this boundary layer state is achieved. While travelling waves act through turbulence modification and drag-reducing processes, suction acts through direct removal of low-momentum fluid. Nevertheless, both approaches influence the same key parameter governing the shock boundary layer interaction and therefore produce similar global aerodynamic benefits.

Taken together, the results of both studies allow a broader conclusion regarding active flow control in transonic airfoil flows. The effectiveness of a control strategy cannot be evaluated alone based on local quantities such as skin friction drag. In transonic conditions, the pressure field and shock position are strongly coupled to boundary layer development. As a consequence, a control method may successfully reduce friction drag without yielding a net aerodynamic benefit if the associated pressure drag is too large. The assessment of active flow control in transonic flows, therefore, requires a global perspective in which friction drag, lift, and actuation power are considered simultaneously.

This conclusion is particularly relevant for drag reduction concepts originally developed in canonical incompressible turbulent flows. While skin friction reduction is naturally the primary objective in suction flows, the present results demonstrate that the aerodynamic benefit of these strategies cannot be transferred directly to realistic transonic configurations. The presence of a shock introduces an additional and often dominant mechanism that fundamentally alters the relationship between local flow modifications and global aerodynamic performance. Consequently, active flow control concepts for transonic aircraft applications should be evaluated primarily according to their ability to manipulate the shock boundary layer interaction in a favorable and energetically efficient manner.

The findings of this thesis must nevertheless be interpreted in light of the limitations of the performed investigations. The first study employed RANS simulations with fixed transition to enable a broad exploration of the parameter space. While suitable for identifying trends and sensitivities, this approach cannot resolve all details of the turbulent flow field. The second study relied on

direct numerical simulations and therefore provided substantially greater physical insight, but was restricted to relatively low Reynolds numbers. Under such conditions, the boundary layer is thicker relative to the chord length than under realistic flight conditions. As a result, the influence of active flow control on momentum thickness and shock position is expected to be more pronounced than at higher Reynolds numbers. The aerodynamic improvements observed in the present work, therefore, likely represent an upper bound, while the achievable benefits under realistic cruise conditions may be smaller.

A further limitation concerns the estimation of actuation power. Simplified and partly idealized assumptions were adopted in both studies to enable transparent and consistent comparison between control strategies. Practical implementations would inevitably involve additional losses and integration constraints. Consequently, the energetic feasibility of the investigated control concepts cannot yet be assessed conclusively. Furthermore, the present work considered only two-dimensional airfoil flows. Important effects associated with real aircraft configurations, including induced drag, wing sweep, and three-dimensional flow structures, were outside the scope of the investigation and may significantly influence the achievable performance gains.

Despite these limitations, the present thesis establishes a clear physical framework for future investigations. A key next step is the systematic optimization of control parameters under conditions representative of realistic cruise operations. For wall-normal suction, this includes optimization of control magnitude, control region extent, and placement relative to the operating point. For streamwise travelling waves, wavelength, frequency, amplitude, and phase speed require further investigation with particular emphasis on energetic benefit. Extensions to higher Reynolds numbers and more realistic aerodynamic configurations are also necessary to determine whether the identified mechanisms remain dominant under practical operating conditions. Another promising direction is the combined optimization of airfoil geometry and active flow control, since the effectiveness of the control appears closely linked to the baseline shock position and pressure distribution. In addition, combinations with laminar flow control concepts may offer further benefits for suction-based approaches.

In conclusion, this thesis has demonstrated that active flow control can improve aerodynamic efficiency in compressible and transonic airfoil flows, but that these improvements are primarily linked to modifications of the shock boundary layer interaction rather than to direct reductions in wall-shear stress. Wall-normal blowing was found to reduce friction drag locally but did not improve aerodynamic efficiency within the investigated parameter range. Wall-normal suction, in contrast, produced beneficial effects for low control magnitudes in selected transonic cases by shifting the shock downstream and increasing lift. The comparison with streamwise travelling waves further revealed that control methods with fundamentally different local effects can generate aerodynamic benefits. The common mechanism underlying these improvements is the reduction of momentum thickness upstream of the shock and the resulting modification of the shock boundary layer interaction.

The two research questions formulated at the beginning of the thesis can therefore be answered consistently. First, the effectiveness of wall-normal blowing and suction is strongly governed by their influence on the shock boundary layer interaction, with suction proving beneficial only within a limited range of transonic operating conditions. Second, the dominant mechanism responsible for improved aerodynamic efficiency for both suction and travelling waves is the reduction of momentum thickness upstream of the shock and the resulting downstream displacement of the shock, while the differences between the approaches lie in the local processes used to achieve this boundary layer state. By identifying this common physical mechanism, the present thesis contributes to a deeper understanding of active flow control in the transonic regime and guides

the development of future flow control concepts aimed at improving the aerodynamic efficiency of transport aircraft.

8 References

Bibliography

[1] A Clean Planet for all - A European strategic long-term vision for a prosperous, modern, competitive and climate neutral economy. Technical report, European Commission, Brussels, 2018.

[2] Communication form the commission to the European Parliament, the European Council, the Council, the European Economic and Social Commitee and the Committee of the Regions - The European Green Deal. Technical Report 15051/19, Council of the European Union, 2019.

[3] A. Abbas, G. Bugeda, E. Ferrer, S. Fu, J. Periaux, J. Pons-Prats, E. Valero, and Y. Zheng. Drag reduction via turbulent boundary layer flow control. *Science China Technological Sciences*, 60(9):1281–1290, Sept. 2017. ISSN 1674-7321, 1869-1900. DOI 10.1007/s11431-016-9013-6.

[4] J. D. Anderson. *Modern compressible flow: with historical perspective*. McGraw-Hill series in aeronautical and aerospace engineering. McGraw-Hill, Boston, Mass., 3. ed., internat. ed edition, 2003. ISBN 978-0-07-242443-0 978-0-07-124136-6 978-0-07-112161-3.

[5] M. Atzori, R. Vinuesa, G. Fahland, A. Stroh, D. Gatti, B. Frohnapfel, and P. Schlatter. Aerodynamic Effects of Uniform Blowing and Suction on a NACA4412 Airfoil. *Flow, Turbulence and Combustion*, 105(3):735–759, Sept. 2020. ISSN 1386-6184, 1573-1987. DOI 10.1007/s10494-020-00135-z.

[6] F. Auteri, A. Baron, M. Belan, G. Campanardi, and M. Quadrio. Experimental assessment of drag reduction by traveling waves in a turbulent pipe flow. *Physics of Fluids*, 22(11), Nov. 2010. ISSN 1070-6631, 1089-7666. DOI 10.1063/1.3491203.

[7] J. Banchetti, P. Luchini, and M. Quadrio. Turbulent drag reduction over curved walls. *Journal of Fluid Mechanics*, 896:A10, Aug. 2020. ISSN 0022-1120, 1469-7645. DOI 10.1017/jfm.2020.338.

[8] D. W. Bechert, M. Bruse, W. Hage, J. G. T. Van Der Hoeven, and G. Hoppe. Experiments on drag-reducing surfaces and their optimization with an adjustable geometry. *Journal of Fluid Mechanics*, 338:59–87, May 1997. ISSN 0022-1120, 1469-7645. DOI 10.1017/S0022112096004673.

[9] N. Beck, T. Landa, A. Seitz, L. Boermans, Y. Liu, and R. Radespiel. Drag Reduction by Laminar Flow Control. *Energies*, 11(1):252, Jan. 2018. ISSN 1996-1073. DOI 10.3390/en11010252.

[10] N. Berizzi, D. Gatti, G. Soldati, S. Pirozzoli, and M. Quadrio. Aerodynamic performance of a transonic airfoil with spanwise forcing. *Journal of Fluid Mechanics*, 1010:A18, May 2025. ISSN 0022-1120, 1469-7645. DOI 10.1017/jfm.2025.332.

[11] M. Bernardini, D. Modesti, F. Salvadore, and S. Pirozzoli. STREAmS: A high-fidelity accelerated solver for direct numerical simulation of compressible turbulent flows. *Computer Physics Communications*, 263:107906, June 2021. ISSN 0010-4655. DOI 10.1016/j.cpc.2021.107906.

[12] J. Bird, M. Santer, and J. F. Morrison. Experimental Control of Turbulent Boundary Layers with In-plane Travelling Waves. *Flow, Turbulence and Combustion*, 100(4):1015–1035, June 2018. ISSN 1386-6184, 1573-1987. DOI 10.1007/s10494-018-9926-2.

[13] T. Black, A. Sarnecki, and W. Mair. The turbulent boundary layer with suction or injection. *Aeronautical Research Council Reports & Memoranda*, (20), 1958.

[14] P. H. Cook, M. A. McDonald, and M. P. Firmin. Aerofoil RAE2822 - pressure distributuions, boundary layer and wake measurements. *AGARD Report AR*, (138), 1979.

[15] P. Doerffer, P. Flaszynski, J.-P. Dussauge, H. Babinsky, P. Grothe, A. Petersen, and F. Billard, editors. *Transition Location Effect on Shock Wave Boundary Layer Interaction: Experimental and Numerical Findings from the TFAST Project*, volume 144 of *Notes on Numerical Fluid Mechanics and Multidisciplinary Design*. Springer International Publishing, Cham, 2021. ISBN 978-3-030-47460-7 978-3-030-47461-4. DOI 10.1007/978-3-030-47461-4.

[16] T. D. Economon, F. Palacios, S. R. Copeland, T. W. Lukaczyk, and J. J. Alonso. SU2: An Open-Source Suite for Multiphysics Simulation and Design. *AIAA Journal*, 54(3):828–846, Mar. 2016. ISSN 0001-1452, 1533-385X. DOI 10.2514/1.J053813.

[17] K. Eto, Y. Kondo, K. Fukagata, and N. Tokugawa. Assessment of Friction Drag Reduction on a Clark-Y Airfoil by Uniform Blowing. *AIAA Journal*, 57(7):2774–2782, July 2019. ISSN 0001-1452, 1533-385X. DOI 10.2514/1.J057998.

[18] G. Fahland, A. Stroh, B. Frohnapfel, M. Atzori, R. Vinuesa, P. Schlatter, and D. Gatti. Investigation of Blowing and Suction for Turbulent Flow Control on Airfoils. *AIAA Journal*, 59(11):4422–4436, Nov. 2021. ISSN 0001-1452, 1533-385X. DOI 10.2514/1.J060211.

[19] J. H. Ferziger and M. Perić. *Computational methods for fluid dynamics*. Springer-Verlag, Berlin [i pozostałe], third, rev. edition edition, 2002. ISBN 978-3-540-42074-3. OCLC: 1042943810.

[20] J. H. Ferziger, M. Perić, and R. L. Street. *Numerische Strömungsmechanik*. Springer Berlin Heidelberg, Berlin, Heidelberg, 2., aktual. aufl. 2020 edition, 2020. ISBN 978-3-662-46544-8. DOI 10.1007/978-3-662-46544-8.

[21] M. Gad-el Hak. *Flow Control: Passive, Active, and Reactive Flow Management*. Cambridge University Press, 1 edition, Aug. 2000. ISBN 978-0-521-77006-4 978-0-521-03671-9 978-0-511-52953-5. DOI 10.1017/CBO9780511529535.

[22] F. Gattere, M. Zanolini, D. Gatti, M. Bernardini, and M. Quadrio. Turbulent drag reduction with streamwise-travelling waves in the compressible regime. *Journal of Fluid Mechanics*, 987: A30, May 2024. ISSN 0022-1120, 1469-7645. DOI 10.1017/jfm.2024.408.

[23] D. Gatti and M. Quadrio. Reynolds-number dependence of turbulent skin-friction drag reduction induced by spanwise forcing. *Journal of Fluid Mechanics*, 802:553–582, Sept. 2016. ISSN 0022-1120, 1469-7645. DOI 10.1017/jfm.2016.485.

[24] D. Gatti, A. Güttler, B. Frohnapfel, and C. Tropea. Experimental assessment of spanwise-oscillating dielectric electroactive surfaces for turbulent drag reduction in an air channel flow. *Experiments in Fluids*, 56(5):110, May 2015. ISSN 0723-4864, 1432-1114. DOI 10.1007/s00348-015-1983-x.

[25] K. Gersten and J. Wiedemann. *Widerstandsverminderung umströmter Körper durch kombiniertes Ausblasen und Absaugen an der Wand.* VS Verlag für Sozialwissenschaften, Wiesbaden, 1982. ISBN 978-3-531-03103-3 978-3-322-87701-7. DOI 10.1007/978-3-322-87701-7.

[26] GitHub. GPy, 2012. URL https://github.com/SheffieldML/GPy.

[27] GitHub. GPyOpt, 2016. URL https://github.com/SheffieldML/GPyOpt.

[28] B. Graver, K. Zhang, and D. Rutherford. Emissions from commercial aviation, 2018. 2019.

[29] N. Gregory. Research on suction surfaces for laminar flow. In *Boundary Layer and Flow Control*, pages 924–960. Elsevier, 1961. ISBN 978-1-4832-1323-1. DOI 10.1016/B978-1-4832-1323-1.50012-9.

[30] K. P. Griffin, L. Fu, and P. Moin. General method for determining the boundary layer thickness in nonequilibrium flows. *Physical Review Fluids*, 6(2):024608, Feb. 2021. ISSN 2469-990X. DOI 10.1103/PhysRevFluids.6.024608.

[31] H. Herwig. *Strömungsmechanik: Einführung in die Physik von technischen Strömungen.* SpringerLink Bücher. Vieweg+Teubner, Wiesbaden, 2008. ISBN 978-3-8348-0334-4 978-3-8348-9497-7. DOI 10.1007/978-3-8348-9497-7.

[32] L. Huang, P. G. Huang, R. P. LeBeau, and T. Hauser. Numerical Study of Blowing and Suction Control Mechanism on NACA0012 Airfoil. *Journal of Aircraft*, 41(5):1005–1013, Sept. 2004. ISSN 0021-8669, 1533-3868. DOI 10.2514/1.2255.

[33] D. Hwang. Review of research into the concept of the microblowing technique for turbulent skin friction reduction. *Progress in Aerospace Sciences*, 40(8):559–575, Nov. 2004. ISSN 03760421. DOI 10.1016/j.paerosci.2005.01.002.

[34] W. J. Jung, N. Mangiavacchi, and R. Akhavan. Suppression of turbulence in wall-bounded flows by high-frequency spanwise oscillations. *Physics of Fluids A: Fluid Dynamics*, 4(8): 1605–1607, Aug. 1992. ISSN 0899-8213. DOI 10.1063/1.858381.

[35] Y. Kametani and K. Fukagata. Direct numerical simulation of spatially developing turbulent boundary layers with uniform blowing or suction. *Journal of Fluid Mechanics*, 681:154–172, Aug. 2011. ISSN 0022-1120, 1469-7645. DOI 10.1017/jfm.2011.219.

[36] Y. Kametani, K. Fukagata, R. Örlü, and P. Schlatter. Effect of uniform blowing/suction in a turbulent boundary layer at moderate Reynolds number. *International Journal of Heat and Fluid Flow*, 55:132–142, Oct. 2015. ISSN 0142727X. DOI 10.1016/j.ijheatfluidflow.2015.05.019.

[37] M. Klöwer, M. R. Allen, D. S. Lee, S. R. Proud, L. Gallagher, and A. Skowron. Quantifying aviation's contribution to global warming. *Environmental Research Letters*, 16(10):104027, Oct. 2021. ISSN 1748-9326. DOI 10.1088/1748-9326/ac286e.

[38] M. W. Knoop, F. H. Hartog, F. F. J. Schrijer, O. W. G. Van Campenhout, M. Van Nesselrooij, and B. W. Van Oudheusden. Experimental assessment of square-wave spatial spanwise forcing of a turbulent boundary layer. *Experiments in Fluids*, 65(5):65, May 2024. ISSN 0723-4864, 1432-1114. DOI 10.1007/s00348-024-03799-9.

[39] V. Kornilov. Current state and prospects of researches on the control of turbulent boundary layer by air blowing. *Progress in Aerospace Sciences*, 76:1–23, July 2015. ISSN 03760421. DOI 10.1016/j.paerosci.2015.05.001.

[40] V. I. Kornilov and A. V. Boiko. Efficiency of Air Microblowing Through Microperforated Wall for Flat Plate Drag Reduction. *AIAA Journal*, 50(3):724–732, Mar. 2012. ISSN 0001-1452, 1533-385X. DOI 10.2514/1.J051426.

[41] X.-D. Liu, S. Osher, and T. Chan. Weighted Essentially Non-oscillatory Schemes. *Journal of Computational Physics*, 115(1):200–212, Nov. 1994. ISSN 00219991. DOI 10.1006/jcph.1994.1187.

[42] I. Marusic, D. Chandran, A. Rouhi, M. K. Fu, D. Wine, B. Holloway, D. Chung, and A. J. Smits. An energy-efficient pathway to turbulent drag reduction. *Nature Communications*, 12 (1), Oct. 2021. ISSN 2041-1723. DOI 10.1038/s41467-021-26128-8.

[43] B. Mele, R. Tognaccini, and P. Catalano. Performance Assessment of a Transonic Wing–Body Configuration with Riblets Installed. *Journal of Aircraft*, 53(1):129–140, Jan. 2016. ISSN 0021-8669, 1533-3868. DOI 10.2514/1.C033220.

[44] F. Menter. Zonal Two Equation k-w Turbulence Models For Aerodynamic Flows. In *23rd Fluid Dynamics, Plasmadynamics, and Lasers Conference*, Orlando,FL,U.S.A., July 1993. American Institute of Aeronautics and Astronautics. DOI 10.2514/6.1993-2906.

[45] H. S. Mickley, R. C. Ross, A. L. Squyers, and W. E. Stewart. Heat, Mass, and Momentum Transfer for Flow over a Flat Plate with Blowing or Suction. (3208):1–25, 1954.

[46] Y. Morita, S. Rezaeiravesh, N. Tabatabaei, R. Vinuesa, K. Fukagata, and P. Schlatter. Applying Bayesian optimization with Gaussian process regression to computational fluid dynamics problems. *Journal of Computational Physics*, 449:110788, Jan. 2022. ISSN 00219991. DOI 10.1016/j.jcp.2021.110788.

[47] M. Ohashi, Y. Morita, S. Hirokawa, K. Fukagata, and N. Tokugawa. Parametric study toward optimization of blowing and suction locations for improving lift-to-drag ratio on a Clark-Y airfoil. *Journal of Fluid Science and Technology*, 15(2):JFST0008–JFST0008, 2020. ISSN 1880-5558. DOI 10.1299/jfst.2020jfst0008.

[48] J. Park and H. Choi. Effects of uniform blowing or suction from a spanwise slot on a turbulent boundary layer flow. *Physics of Fluids*, 11(10):3095–3105, Oct. 1999. ISSN 1070-6631, 1089-7666. DOI 10.1063/1.870167.

[49] S. V. Patankar. *Numerical heat transfer and fluid flow.* Series in computational methods in mechanics and thermal sciences. McGraw-Hill [u.a.], New York, NY Hamburg, 1980. ISBN 978-0-07-048740-6.

[50] U. Piomelli, P. Moin, and J. Ferziger. Large eddy simulation of the flow in a transpired channel. *Journal of Thermophysics and Heat Transfer*, 5(1):124–128, Jan. 1991. ISSN 0887-8722, 1533-6808. DOI 10.2514/3.238.

[51] S. Pirozzoli. Generalized conservative approximations of split convective derivative operators. *Journal of Computational Physics*, 229(19):7180–7190, Sept. 2010. ISSN 0021-9991. DOI 10.1016/j.jcp.2010.06.006.

[52] S. Pirozzoli. Numerical Methods for High-Speed Flows. *Annual Review of Fluid Mechanics*, 43(1):163–194, Jan. 2011. ISSN 0066-4189, 1545-4479. DOI 10.1146/annurev-fluid-122109-160718.

[53] S. Pirozzoli. Stabilized non-dissipative approximations of Euler equations in generalized curvilinear coordinates. *Journal of Computational Physics*, 230(8):2997–3014, Apr. 2011. ISSN 0021-9991. DOI 10.1016/j.jcp.2011.01.001.

[54] T. Poinsot and S. Lelef. Boundary conditions for direct simulations of compressible viscous flows. *Journal of Computational Physics*, 101(1):104–129, July 1992. ISSN 00219991. DOI 10.1016/0021-9991(92)90046-2.

[55] L. Prandtl and A. Betz, editors. *Ergebnisse der Aerodynamischen Versuchsanstalt zu Göttingen - IV. Lieferung*, volume 7 of *Göttinger Klassiker der Strömungmechanik*. Göttingen University Press, Göttingen, 1932.

[56] D. Prosser. Construct2D. URL https://sourceforge.net/projects/construct2d/.

[57] M. Quadrio and P. Ricco. Critical assessment of turbulent drag reduction through spanwise wall oscillations. *Journal of Fluid Mechanics*, 521:251–271, Dec. 2004. ISSN 0022-1120, 1469-7645. DOI 10.1017/S0022112004001855.

[58] M. Quadrio, P. Ricco, and C. Viotti. Streamwise-travelling waves of spanwise wall velocity for turbulent drag reduction. *Journal of Fluid Mechanics*, 627:161–178, May 2009. ISSN 0022-1120, 1469-7645. DOI 10.1017/S0022112009006077.

[59] M. Quadrio, A. Chiarini, J. Banchetti, D. Gatti, A. Memmolo, and S. Pirozzoli. Drag reduction on a transonic airfoil. *Journal of Fluid Mechanics*, 942:R2, July 2022. ISSN 0022-1120, 1469-7645. DOI 10.1017/jfm.2022.369.

[60] C. E. Rasmussen and C. K. I. Williams. *Gaussian processes for machine learning*. Adaptive computation and machine learning. MIT Press, Cambridge, Mass., 3. print edition, 2008. ISBN 978-0-262-18253-9.

[61] O. Reynolds. On the dynamical theory of incompressible viscous fluids and the determination of the criterion. *Philosophical Transactions of the Royal Society of London. (A.)*, (186):123–164, 1895. ISSN 0264-3820, 2053-9231. DOI 10.1098/rsta.1895.0004.

[62] S. Rezaeiravesh, T. Mukha, and P. Schlatter. Efficient prediction of turbulent flow quantities using a Bayesian hierarchical multifidelity model. *Journal of Fluid Mechanics*, 964:A13, June 2023. ISSN 0022-1120, 1469-7645. DOI 10.1017/jfm.2023.327.

[63] P. Ricco, M. Skote, and M. A. Leschziner. A review of turbulent skin-friction drag reduction by near-wall transverse forcing. *Progress in Aerospace Sciences*, 123:100713, May 2021. ISSN 03760421. DOI 10.1016/j.paerosci.2021.100713.

[64] P. Roe. Approximate Riemann solvers, parameter vectors, and difference schemes. *Journal of Computational Physics*, 43(2):357–372, Oct. 1981. ISSN 00219991. DOI 10.1016/0021-9991(81)90128-5.

[65] C.-C. Rossow, K. Wolf, and P. Horst, editors. *Handbuch der Luftfahrzeugtechnik: mit 34 Tabellen*. Hanser, München, 2014. ISBN 978-3-446-42341-1.

[66] S. Russo and P. Luchini. A fast algorithm for the estimation of statistical error in DNS (or experimental) time averages. *Journal of Computational Physics*, 347:328–340, Oct. 2017. ISSN 00219991. DOI 10.1016/j.jcp.2017.07.005.

[67] P. Schlatter and R. Örlü. Assessment of direct numerical simulation data of turbulent boundary layers. *Journal of Fluid Mechanics*, 659:116–126, Sept. 2010. ISSN 0022-1120, 1469-7645. DOI 10.1017/S0022112010003113.

[68] P. Schlatter and R. Örlü. Turbulent boundary layers at moderate Reynolds numbers: inflow length and tripping effects. *Journal of Fluid Mechanics*, 710:5–34, Nov. 2012. ISSN 0022-1120, 1469-7645. DOI 10.1017/jfm.2012.324.

[69] H. Schlichting and K. Gersten. *Grenzschicht-Theorie*. Springer, Berlin ; New York, 9., völlig neubearbeitete und erw. aufl edition, 1997. ISBN 978-3-540-55744-9.

[70] G. Soldati, A. Ceci, and S. Pirozzoli. FLEW: A DNS Solver for Compressible Flows in Generalized Curvilinear Coordinates. *Aerotecnica Missili & Spazio*, 103(4):413–425, Dec. 2024. ISSN 0365-7442, 2524-6968. DOI 10.1007/s42496-024-00199-4.

[71] P. R. Spalart and J. D. McLean. Drag reduction: enticing turbulence, and then an industry. *Philosophical Transactions of the Royal Society A: Mathematical, Physical and Engineering Sciences*, 369(1940):1556–1569, Apr. 2011. ISSN 1364-503X, 1471-2962. DOI 10.1098/rsta.2010.0369.

[72] J. H. Spurk and N. Aksel. *Strömungslehre: Einführung in die Theorie der Strömungen*. Springer-Lehrbuch. Springer Berlin Heidelberg, Berlin, Heidelberg, 7. aufl. 2007 edition, 2007. ISBN 978-3-540-38439-7 978-3-540-38441-0. DOI 10.1007/978-3-540-38441-0.

[73] A. Stroh, Y. Hasegawa, P. Schlatter, and B. Frohnapfel. Global effect of local skin friction drag reduction in spatially developing turbulent boundary layer. *Journal of Fluid Mechanics*, 805:303–321, Oct. 2016. ISSN 0022-1120, 1469-7645. DOI 10.1017/jfm.2016.545.

[74] Y. Sumitani and N. Kasagi. Direct numerical simulation of turbulent transport with uniform wall injection and suction. *AIAA Journal*, 33(7):1220–1228, July 1995. ISSN 0001-1452, 1533-385X. DOI 10.2514/3.12363.

[75] W. Sutherland. The viscosity of gases and molecular force. *The London, Edinburgh, and Dublin Philosophical Magazine and Journal of Science*, 36(223):507–531, 1893. ISSN 1941-5982, 1941-5990. DOI 10.1080/14786449308620508.

[76] J. Szodruch. Viscous drag reduction on transport aircraft. In *29th Aerospace Sciences Meeting*, Reno,NV,U.S.A., Jan. 1991. American Institute of Aeronautics and Astronautics. DOI 10.2514/6.1991-685.

[77] M. R. Visbal and D. V. Gaitonde. On the Use of Higher-Order Finite-Difference Schemes on Curvilinear and Deforming Meshes. *Journal of Computational Physics*, 181(1):155–185, Sept. 2002. ISSN 0021-9991. DOI 10.1006/jcph.2002.7117.

[78] M. J. Walsh. Riblets for aircraft skin-friction reduction. *Langley Symposium on Aerodynamics*, (1), 1986.

[79] M. J. Walsh, W. L. Sellers, and C. B. McGinley. Riblet drag at flight conditions. *Journal of Aircraft*, 26(6):570–575, June 1989. ISSN 0021-8669, 1533-3868. DOI 10.2514/3.45804.

[80] D. C. Wilcox. *Turbulence Modeling for CFD*. DCW Industries, 1994.

[81] D. Xu, P. Ricco, and L. Duan. Decomposition of the skin-friction coefficient of compressible boundary layers. *Physics of Fluids*, 35(3):035107, Mar. 2023. ISSN 1070-6631, 1089-7666. DOI 10.1063/5.0142129.

[82] J. Yao and F. Hussain. Supersonic turbulent boundary layer drag control using spanwise wall oscillation. *Journal of Fluid Mechanics*, 880:388–429, Dec. 2019. ISSN 0022-1120, 1469-7645. DOI 10.1017/jfm.2019.727.

[83] I. Yudhistira and M. Skote. Direct numerical simulation of a turbulent boundary layer over an oscillating wall. *Journal of Turbulence*, 12:N9, Jan. 2011. ISSN 1468-5248. DOI 10.1080/14685248.2010.538397.

List of Conference Contributions

[MFR+23] Fermin Mallor, Annika Frede, Saleh Rezaeiravesh, Davide Gatti, and Philipp Schlatter. Bayesian optimisation of blowing and suction for drag reduction of a transonic airfoil. 2023.

List of Journal Publications

[FAF+23] Georg Fahland, Marco Atzori, Annika Frede, Alexander Stroh, Bettina Frohnapfel, and Davide Gatti. Drag Assessment for Boundary Layer Control Schemes with Mass Injection. *Flow, Turbulence and Combustion*, 113(1):119–138, 2023. doi:10.1007/s10494-023-00462-x.

[FG25] A. Frede and D. Gatti. Investigation of blowing and suction for turbulent flow control on a transonic airfoil. *International Journal of Heat and Fluid Flow*, 113:109769, June 2025. doi:10.1016/j.ijheatfluidflow.2025.109769.

[FSP+26] Annika Frede, Giulio Soldati, Sergio Pirozzoli, Niccolò Berizzi, Maurizio Quadrio, and Davide Gatti. Comparison between Localized Skin-Friction Reduction and Suction on a Supercritical Airfoil. *Flow, Turbulence and Combustion*, 116(4):50, May 2026. doi:10.1007/s10494-026-00748-w.

Acronyms and symbols

Acronyms

AoA	angle of attack
BLC	boundary layer control
DNS	direct numerical simulations
ISTM	Institute of Fluid Mechanics at KIT
KIT	Karlsruhe Institute of Technology (KIT)
LES	large eddy simulations
PS	airfoil pressure side (lower side)
RANS	Reynolds-averaged Navier-Stokes
REF	reference case
SS	airfoil suction side (upper side)
StTW	Streamwise traveling waves
SW	streamwise waves
TBL	turbulent boundary layer
TKE	turbulent kinetic energy
US	uniform suction
ZPG	zero pressure gradient

Latin letter - Upper case

A	surface
A_K	wetted surface
A_{StTW}	amplitude of StTW control
A_{US}	suction amplitude
A_{wall}	area of the wall
C	Sutherland constant
E	efficiency
E_{BLC}	total energy of boundary layer control

E_{tot}	total energy
E_w	total energy at the wall
$\vec{F}$	force
F_{body}	body force
F_D	drag force
F_L	lift force
F_S	side force
$F_{surface}$	surface force
$\vec{F}_{tot}$	total aerodynamic force
H	shape factor
$L_{\{X,Y\}}$	Gaussian attenuation
L_Z	spanwise extent of the airfoil
Ma	Mach number
Ma_∞	freestream Mach number
P_{pump}	ideal power for suction
P_{StTW}	power for StTW actuation
P_{thrust}	thrust power
P_{us}	net power input
$\dot{Q}$	net heat flux
R	response of Bayesian optimization
$\mathcal{R}$	Riemann invariant
R_{id}	ideal gas constant
Re	Reynolds number
Re_∞	freestream Reynolds number
Re_θ	Reynolds number based on momentum thickness
T	temperature
$\mathbf{T}$	shear stress tensor
T_0	reference temperature
T_∞	freestream temperature
T_b	blowing air temperature
T_s	suction air temperature
T_{us}	temperature of suction fluid
T_w	wall temperature

U_∞	freestream velocity
U_e	velocity at boundary layer edge
V	volume
W	work
X_b	start of the control region
X_e	end of the control region
X, Y, Z	normalized wall coordinate system

Latin letter - Lower case

$\vec{a}$	speed of sound
a_∞	freestream speed of sound
a_{BLC}	boundary speed of sound
c	chord length
c_{BLC}	boundary layer control penalty
c_D	drag coefficient
$c_{D,b}$	body drag coefficient
$c_{D,f}$	friction drag
$c_{D,inc}$	inclusive drag coefficient
$c_{D,p}$	pressure drag
$c_{D,tot}$	total drag coefficient
$c_{D,w}$	wake drag coefficient
c_f	friction coefficient
c_L	lift coefficient
c_p	pressure coefficient
c_p^*	sonic pressure coefficient
$c_{p,chamber}$	pressure coefficient of the chamber
$c_{p,control}$	pressure coefficient in the control regime
$c_{p,rms}$	rms of pressure coefficient
c_{pump}	pump coefficient
c_{sh}	specific heat constant
$c_{turbine}$	turbine coefficient
d_o	outlet distance in meshes
e	internal energy

$\hat{e}_x$	unit vector in streamwise direction
f_{sm}	smoothing function
$\vec{g}$	gravity
h_t	total enthalpy
$\vec{I}$	momentum
i, j	indices
$\vec{k}$	body force per unit mass
l	characteristic length
l_{BLC}	streamwise extent of blowing and suction boundary layer control
l_{out}	length of outflow
l_s	airfoil span
l_{us}	length of uniform suction control
m	mass
$\dot{m}_\infty$	freestream mass flow per unit area
$\dot{m}$	mass flux
$\dot{m}_{BLC}$	boundary layer control mass flux
$\dot{m}_{out}$	mass flux of outflow conditions
$\dot{m}_{us}$	mass flux of uniform suction
$\hat{n}$	unit normal vector
p	pressure
p_∞	freestream pressure
p_b	blowing pressure
$p_{chamber}$	pressure of the supply chamber
p_{out}	pressure at outflow conditions
p_s	suction pressure
p_{us}	pressure of uniform suction fluid
p_w	projected pressure
$\vec{q}$	heat flux
q_∞	freestream dynamic pressure
r_c	radius of far-field boundary in meshes
s	sampling coordinate
t	time
$\vec{t}$	stress

$\hat{t}$	tangential unit vector
u **and** $\vec{u}$	velocity
u_{BLC}	velocity of blowing and suction boundary layer control
$u_{\delta_{99}}$	velocity equal to $0.99U_e$
u_{out}	velocity of outflow
u_{StTW}	wall-tangential actuation of streamwise travelling waves
u_t	wall normal velocity
u_τ	friction velocity
u_{US}	wall-normal uniform suction velocity
w_w	wall velocity of traveling waves
w_ξ	spanwise wall velocity
x_s	shock position
x_{sm}	smoothing distance
x, y, z	wall coordinate system

Greek letters - Upper case

Γ	generic metric
Φ	extensive property

Greek letters - Lower case

α	angle of attack
γ	ratio of specific heats
δ_{99}	geometric boundary layer thickness
δ^*	displacement thickness
η, ξ	airfoil coordinate system
η_p	pump efficiency
η_t	turbine efficiency
θ	momentum thickness
κ_x	spatial frequency
λ_z	spanwise wavelength
μ	dynamic viscosity
μ_0	dynamic viscosity at reference temperature T_0
μ_∞	freestream viscosity

ν_∞	freestream kinematic viscosity
ν_τ	viscosity based on friction velocity
ν_w	kinematic viscosity at the wall
ξ	hyper-parameter
ρ	density
ρ_∞	freestream density
ρ_{BLC}	density of blowing and suction control fluid
ρ_e	density at boundary layer edge
ρ_{int}	density of nearest interior cell
ρ_{out}	density at outflow conditions
ρ_{us}	density of uniform suction fluid
ρ_w	density at the wall
σ_D	drag coefficient uncertainty
σ_L	lift coefficient uncertainty
τ_w	wall shear stress
ϕ	intensive property
ϕ_{nv}	probability of negative velocity
ω	temporal frequency

Mathematical operators

$\partial\,(...)$	partial derivative
d(...)	ordinary derivative
D(...)	material derivative
Δ	difference
∇	Laplace operator
$\mathbf{a}$	vector/tensor (bold print)
$\mathbf{T}$	transposed
$\lvert\vec{(...)}\rvert$	Euclidean norm
$\overline{(...)}$	temporal average
$\tilde{(...)}$	Favre average
$(...)'$	instantaneous difference form the mean quantity
$(...)^+$	the quantity is expressed in inner scaling based on the reference case of the turbulent boundary layer

$(...)^*$	the quantity is expressed in inner scaling based on the same case of the turbulent boundary layer

List of Figures

2.1 Sketch of the blowing and suction control mechanism on the upper side of an airfoil. . 6
2.2 Sketch of streamwise travelling waves of spanwise velocity on the upper side of an airfoil. 8

3.1 Sketch of a normalized mean velocity profile of a turbulent boundary layer. 19

4.1 Control Volume (CV) for the airfoil momentum budget in which **n** is the normal vector pointing out of the CV ([FAF$^+$23]). 27

5.1 Sketch of the computational C-mesh. 34
5.2 Sketch of a pressure distribution to determine the different pressure levels for the supply chambers for the pump or turbine. 37
5.3 Sketch of the control areas and different control configurations. 38
5.4 Sketch of the different control positions with respect to the shock position. 38
5.5 Distribution of the pressure and friction coefficient for a RANS and a DNS simulation at a Reynolds number of $Re = 3 \times 10^5$. 40
5.6 Pressure distribution of the RANS simulation and the experimental data of Cook et al. [14] at a Reynolds number of $Re = 6.5 \times 10^6$. 40
5.7 Polar plot and pressure and friction coefficient distribution for the three control configurations and the uncontrolled reference case for $\dot{m}_{BLC} = 0.1\%\dot{m}_\infty$ and $\alpha = 2.31°$ for the surface distribution plots, and $Ma = 0.6$ and 0.725 for the left and right columns, respectively. 42
5.8 Polar plot and pressure and friction coefficient distribution for different control magnitudes and the uncontrolled reference case. The applied control is suction on the suction side at Mach numbers of $Ma = 0.65$ and 0.725 for the left and right columns, respectively. The surface plots are shown for an angle of attack of $\alpha = 2.31°$. 44
5.9 Polar plot and pressure and friction coefficient distribution for different control magnitudes and the uncontrolled reference case. The applied control is blowing on the pressure side at Mach numbers of $Ma = 0.65$ and 0.725 for the left and right columns, respectively. The surface plots are shown for an angle of attack of $\alpha = 2.31°$. 46
5.10 Snapshot of the streamlines for (a) the uncontrolled case and (b) the controlled case with blowing on the pressure side for $Ma = 0.65$, $\alpha = 2.31°$ and $\dot{m}_{BLC} = 1.2\%\dot{m}_\infty$. 47
5.11 Drag distribution for different Mach numbers for suction on the suction side with a control magnitude of $m_{BLC} = 0.2\%\dot{m}_\infty$ and an angle of attack of $\alpha = 2.31°$. 48
5.12 Drag distribution for different Mach numbers for blowing on the pressure side with a control magnitude of $m_{BLC} = 0.2\%\dot{m}_\infty$ and an angle of attack of $\alpha = 2.31°$. 48
5.13 Polar plot and pressure and friction coefficient distribution for different control positions and the uncontrolled reference case. The applied control is blowing on the suction side and suction on the suction side for the left and right columns, respectively, with a control magnitude of $m_{BLC} = 0.1\%\dot{m}_\infty$. The surface plots are shown for an angle of attack of $\alpha = 2.31°$. 50
5.14 Variation of the Reynolds number for one single configuration at a Mach number of $Ma = 0.725$ and a constant lift coefficient of $c_l = 0.695$. 50
5.15 Efficiency increase for suction on the suction side at three different Mach numbers of $Ma = 0.65$ as a representation of the subsonic case and $Ma = 0.71$ and 0.725 as representations for the transonic cases without the power consumption. 52

5.16 Efficiency increase for suction on the suction side at three different Mach numbers of $Ma = 0.65$ as a representation of the subsonic case and $Ma = 0.71$ and 0.725 as representations for the transonic cases with the power consumption. 53
5.17 Pressure and friction coefficient of the most promising configuration for $Ma = 0.725$, $m_{BLC} = 0.1\%\dot{m}_\infty$ and $\alpha = 3°$ or 3.567° for the controlled (suction on the suction side) and uncontrolled case, respectively. 53
5.18 Distribution of the local Mach number around the airfoil for the reference simulation without active control. 57
5.19 Evolution of the response (as a relative percentage change versus the baseline case) with the number of iterations (left) and cumulative best response found (right). . . . 57
5.20 Best control strategy found after the optimization process for the case in which the drag is minimized (top left), and for the cases in which the cost of the control actuation is taken into account in the objective function (top right and bottom left represent the cases with η equal to 1 and 0.8, respectively). 58
5.21 Pressure c_p (left) and skin-friction c_f coefficient (right) obtained after the optimization process. The baseline case is represented with a black, dashed line, and the best control strategy with a solid line. The color coding refers to the three considered optimization cases as reported in the legend. 58

6.1 a) Sketch of the different coordinate systems used for the analysis of the simulation, and b) sketch of the mesh and the corresponding length scales. 62
6.2 Polar plots for the V2C profile with a fully turbulent approach modeled via RANS simulations. 64
6.3 a) Pressure c_p and b) friction c_f coefficient distribution along the surface of the airfoil for RANS simulations with a fully turbulent approach. 65
6.4 a) Pressure coefficient c_p, b) friction coefficient c_f, and c) rms of pressure coefficient $c_{p,rms}$ distribution along the surface of the airfoil. The vertical lines indicate the shock position. 69
6.5 a) Pressure c_p and b) friction c_f coefficient distribution along the surface of the airfoil. The vertical lines indicate the shock position. 70
6.6 a) Friction and b) pressure drag distribution along the spanwise coordinate of the airfoil as well as the differences between the controlled cases and the reference case for the friction and pressure drag (c) and d)). 72
6.7 Instantaneous velocity profiles of the velocity component tangential to the wall on the upper side of the airfoil. The three cases, a) REF, b) SW2, and c) US2, are shown. 73
6.8 Separation probability ϕ_{nv} of the investigated control methods and the reference case. The vertical lines mark the shock positions. 74
6.9 Integral Boundary layer quantities and the pressure gradient along the upper side in the region of the control for the reference case, as well as the SW2 and US2 cases. . 75
6.10 Integral Boundary layer quantities and the pressure gradient along the upper side in the region of the control for the reference case, as well as the SW1 and SW3; and US1 cases. The modulation of the wall for case SW3 is added in d), matching the modulation of the pressure gradient variation. 77
6.11 Pressure distribution of the Euler solution compared to the DNS results. 78
6.12 Wall-normal profiles of the mean streamwise velocity scaled in viscous units at different positions along the upper side of the airfoil. The corresponding viscous units are computed at $X = 0.35$. 78
6.13 Tangential turbulent stress scaled in viscous units at different positions along the upper side of the airfoil. The corresponding viscous units are computed at $X = 0.35$. . 79

List of Tables

5.1 Aerodynamic coefficients for the conducted validation simulation for the RANS and DNS results for a Reynolds number of $Re = 3 \times 10^5$. 40
5.2 Example cases of suction on the suction side, which promise an increase in efficiency. The uncontrolled cases are rerun at the same lift coefficient as the controlled cases for a better comparison. 51
5.3 Calculation of the power consumption and thrust generation to get a better estimation of the real drag savings for three example Mach numbers. The uncontrolled cases are shown in Table 5.2. 54
5.4 Aerodynamic properties and power consumption of the optimal control strategies. . . 57

6.1 Summary of the performed simulations with the corresponding control parameters. The travelling waves configurations are characterized by the amplitude A, and the spatial κ_x and temporal ω frequencies of the wave. The suction cases are characterized by the uniform suction velocity u_{us}. 66
6.2 Aerodynamic coefficients for the simulated DNS cases for the reference case, as well as the cases with the control via StTW and suction. The lift c_L and drag coefficient c_D are shown with their percentage relative standard deviation σ as well as the two components of the drag ($c_{D,f}$ and $c_{D,p}$). The aerodynamic efficiency E and the position of the shock X_s are also shown. In the right part of the table, the relative change of the drag coefficient and the efficiency is shown with respect to the uncontrolled case. 67
6.3 Calculation of the power consumption for the two control strategies. 81